Non-Tidal Atmosphere and Ocean Background Modelling for Satellite Gravimetry: Development of AOD1B RL07

Dissertation

zur Erlangung des Doktorgrades
der Naturwissenschaften
vorgelegt von

Linus Shihora

am Fachbereich Geowissenschaften der Freien Universität Berlin,
angefertigt am Deutschen GeoForschungsZentrum GFZ, Potsdam.

Berlin, 2023

Erstgutachter:	Prof. Dr. Maik Thomas
Zweitgutachter:	Prof. Dr. Frank Flechtner

Datum der Einreichung:	05.10.2023
Datum der Disputation:	20.06.2024

Abstract

The satellite gravimetry missions GRACE and its successor GRACE-FO measure large-scale mass redistributions in the Earth system, including changes in terrestrial water storage, ice shelves, the oceans and atmosphere as well as the solid Earth. As the measurements are typically accumulated over one month before the computation of a gravity solution, high-frequency mass variations need to be accounted for using a-priori background models. The Atmosphere and Ocean Dealiasing Level 1B (AOD1B) data product routinely provides the necessary simulated non-tidal mass variations in the atmosphere and oceans.

While progress towards better background models has been made over the past years, residual errors in the simulated atmospheric and oceanic mass variations are still among the largest limiting factors to the overall GRACE accuracy. As a result, further improvements of these data-products are directly linked to improvements in the final gravity solutions and thus subsequent geophysical analyses.

This thesis summarizes the most recent improvements to the AOD1B product, including an updated ocean model configuration considering the effects of self-attraction and loading, an updated atmospheric component as well as an improved post-processing and tidal analysis. All of these changes are shown to result in a better representation of the simulated mass variations and are thus combined into a new release RL07 of AOD1B.

Additionally, the new release is examined in terms of its stability and consistency over long and short time-scales. Spurious trends, low-frequency signals or bias jumps in the background model data can, if unaccounted for, introduce biases into the global gravity solutions which are prone to be interpreted erroneously in subsequent geophysical analyses. Consequently, the analysis focusses on signals that might be induced into the final gravity field solutions such as trends but also possible discontinuities caused by changes is the employed atmospheric datasets. It is shown that AOD1B RL07 is free from such artefacts and can thus safely be used as a background model in satellite gravimetry.

Finally, an analysis of the residual errors in AOD1B RL07 is presented. The estimation is based on ensemble statistics derived from different atmospheric reanalyses. For the oceans, the impact of both the forced and intrinsic variability is investigated through differences in simulation experiments. The atmospheric and oceanic information is then combined to produce a new time-series of true errors, called AOe07, which is applicable in combination with AOD1B RL07 and can be used both as stochastic information in the gravity field retrieval process, as well as in simulation studies in preparation for future satellite gravimetry missions.

Kurzfassung

Die Satellitenmission GRACE und ihre Nachfolgemission GRACE-FO messen großskalige Umverteilungen der Massen im Erdsystem. Diese beinhalten unteranderem Veränderungen in terrestrischen Wasserspeichern, Schelfeis, den Ozeanen und der Atmosphäre sowie der festen Erde. Da die Satellitendaten vor der Berechnung einer Schwerefeldlösung typischerweise über einen Monat akkumuliert werden, müssen hochfrequente Massenvariationen durch a-priori Hintergrundmodelle berücksichtigt werden. Das Atmosphere and Ocean Dealiasing Level 1B (AOD1B) Datenprodukt stellt eben diese gezeitenunabhängigen Massenvariationen in der Atmosphäre und den Ozeanen routiniert zur Verfügung.
Obwohl die Hintergrundmodelle der Sattellitengravimetrie über die Jahre hinweg regelmäßig verbessert wurden, sind Fehler in den Modellen immernoch eine der größten Limitierungen für GRACE und GRACE-FO. Im Gegenzug haben Verbesserungen in den Modellen einen direkten positiven Einfluss auch die Genauigkeit der Schwerefeldlösungen und damit auch indirekt auf die darauf basierenden geophysikalischen Anwendungen.
In dieser Arbeit wird die Weiterentwicklung von AOD1B hin zu einem neuen Release AOD1B RL07 zusammengefasst. Der Fokus liegt dabei auf einer aktualisierten Konfiguration des Ozeanmodells, inklusive der Berücksichtigung der Effekte der Selbstanziehung und Auflast der Wassersäule, einem Update der atmosphärischen Komponente und einer verbesserten Datenprozessierung mit verbesserter Behandlung atmosphärischer Gezeiten. Es wird gezeigt, dass diese Veränderungen zu einer besseren Darstellung der atmosphärischen und ozeanischen Massenveränderungen führen und somit zu einer verringerung der GRACE Unsicherheiten beitragen können.
Zusätzlich wird der neue Datensatz auf seine Stabilität und Konsistenz auf sowohl langen als auch kurzen Zeitskalen hin untersucht. Fälschliche Trends oder Diskontinuitäten in den Hintergrundmodellen können bei der Prozessierung der Satellitendaten in die Schwerefeldlösung gebracht werden und anschließend in geophysikalischen Anwendungen zu Fehlinterpretationen führen. Es wird ein Fokus auf bekannte Übergänge in den atmosphärischen Daten von AOD1B sowie lineare Trends gelegt, und gezeigt, dass AOD1B keine entsprechenden problematischen Artefakte aufweist und daher für die Anwendung

in der Satellitengravimetrie geeignet ist.
Abschließend werden die residuellen Unsicherheiten des neuen Datensatzes abgeschätzt. Die Analyse basiert dabei auf der statistischen Auswertung verschiedener atmosphärischer Reanalysen und ozeanischer Ensemble-Simulationen, wobei sowohl die atmosphärisch induzierte Variabilität, als auch die intrinsische Variabilität berücksichtigt werden. Die Ergebnisse beider Komponenten werden anschließend kombiniert, um eine neue Zeitreihe echter Fehler, AOe07 genannt, zur Verfügung zu stellen. Diese ist dabei auf AOD1B RL07 abgestimmt und kann daher sowohl als stochastische Information in der Berechnung der Schwerefeldlösungen verwendet, als auch in Simulationsstudien für zukünftige Schwerefeldmissionen genutzt werden.

Contents

1

Introduction

According to F. R. Helmert, the classical definition of geodesy is given as ’the science of the measurement and mapping of the earth’s surface, its orientation in space, and its external gravity field’ (Torge and Müller, 2012) and the interest in the shape of the Earth can be traced as far back as antiquity (Russo and Levy, 2003). Today, however, the term has typically a more extended meaning as it also includes in particular temporal variations in the Earth’s gravity field. One of the greatest advances in geodesy came with the launch of the first satellites in 1957 (Sputnik) which subsequently allowed measurements of the Earths gravity field with an accuracy greater than ever before (Flechtner et al., 2021). During the following years, several low degree harmonic coefficients of the gravity field were determined from their induced perturbations on the satellites’ orbits. With the launch of dedicated SLR satellite missions, starting with the Starlette satellite in 1975 and followed by the LAGEOS satellites, all of which are still in orbit, more accurate modelling and monitoring, including temporal changes, was possible (Yoder et al., 1983; Flechtner et al., 2021). Eventually, however, the accuracy of the observations and the impact of non-gravitational influences on the satellites limited the scientific results. As a consequence, active satellite missions utilising inter-satellite ranging or gradiometry were developed and led to the launch of the Gravity Recovery and Climate Experiment (GRACE) in 2002 (Tapley et al., 2004). Due to the large success of the mission, a successor mission called GRACE Follow On (GRACE-FO) was launched in 2018 (Landerer et al., 2020) and further new missions are already under development.

To this day, GRACE and GRACE-FO have provided high-resolution global measurements of temporal anomalies in the gravity field for over two decades, exceeding over 200 unique monthly gravity solutions (Dahle et al., 2019a). Due to the length of the time-series, combined with GRACEs inherent ability to monitor depth-integrated mass changes, the results have been invaluable in the assessment of changes in the Earth system undergoing rapid climate change. Most prominently, these include studies of ice-mass loss in both Antarctica (Velicogna et al., 2014, 2020) and Greenland (Velicogna and Wahr, 2005; Sasgen et al., 2020), changes in glacier mass (Arendt et al., 2013) as well as changes in terrestrial water storage (Rodell et al., 2018; Boergens et al., 2020). Combining GRACE data with other measurements such as altimetry or in-situ data has also allowed for analyses of sea-level change (Hamlington et al., 2020; Dobslaw et al., 2020), especially entangling contributions from steric and barystatic sea-level change (Gregory et al., 2019; Volkov et al., 2017). GRACE and GRACE-FO have enabled studying ocean dynamics on a large scale in regions where in-situ measurements are particularly sparse such as the Southern Ocean (Bergmann and Dobslaw, 2012) and attempts have been made towards the monitoring of changes in the Atlantic Overturning Circulation through bottom pressure variations (Landerer et al., 2015). In general, GRACE and GRACE-FO measurements have contributed greatly to measurements of large-scale changes in the Earth system and to our understanding of climate change (Tapley et al., 2019).

Over the past years, a lot of progress has been made towards increasing the quality and reliability of the measurements from satellite gravimetry. This includes improvements in the instrumentation of the GRACE-FO satellites such as an additional laser-ranging instrument, which offers a significantly improved signal-to-noise ratio. Additionally, GRACE-FO features a third star camera head for more robust attitude determination, as well as evolved microwave ranging instruments, GPS receivers and accelerometers. Despite all these improvements, however, several challenges which affect the gravity field solution quality remain. Principally among these are noise levels induced by accelerometer data (Behzadpour et al., 2021) as well as high-frequency mass variations, both tidal (Sulzbach et al., 2021) and non-tidal (Dobslaw et al., 2017), which are not resolvable by the monthly gravity solutions but instead increase the noise of the solutions. Based on a simulation study, Flechtner et al. (2016) determined the largest contributions to the overall error in GRACE to come from these three influences. While progress has been made in all of these aspects since that study, the fact that the error is dominated by the accelerometer noise and high-frequency mass-variations remains. Any reduction in these induced errors will therefore greatly contribute to the quality of the GRACE measurements and their applications.

Using assessments of the background-model accuracy allows a further mitigation of noise due to imperfect background models through stochastic modelling (Kvas and Mayer-Gürr, 2019; Abrykosov et al., 2021) where satellite measurements are weighted based on the associated background model uncertainty. While these approaches do improve the gravity field solutions, they rely on accurate and up-to-date assessments of the background model capabilities.

Especially now that plans for future satellite gravimetry missions are developing (Cesare et al., 2016; Haagmans et al., 2020) and mission funding is approved, efforts towards reducing noise levels and improving background models are as valuable as they ever were. Future gravity missions based on low-low inter-satellite ranging measurements will, even if consisting of multiple satellite pairs (Bender and Nerem, 2008; Massotti et al., 2021), require background models that accurately represent the high-frequency mass variations (Haagmans and Tsaoussi, 2020). Together with possible improvements in the quality of the ranging data and improved sensor performance, improvements in background models will not only have a significant impact on the final data quality but be imperative in order to make full use of the increased performance of future double-pair constellations.

To that end, this work presents the recent efforts towards the development, production and assessment of a new release of the Atmosphere and Ocean De-Aliasing Level-1B product, AOD1B RL07. The aim of this work is to develop a new background model that provides a more accurate representation of the high-frequency non-tidal mass variations in the Earths atmosphere and oceans compared to its predecessors and thus improves the quality of the GRACE and GRACE-FO gravity solutions. Additionally, it needs to be ensured that the data product is stable and consistent over both long and short timescales and residual errors in the background models need to be assessed, which allow for a reduction of residual aliasing artefacts through stochastic modelling and aid in the performance assessment of future gravity missions.

Structure of this thesis

This thesis is structured around four first-author publications by L. Shihora that outline the development, production and assessment of AOD1B RL07.
Sect. 2 consists of an introduction to the relevant topics covered in this thesis. This includes an overview of the GRACE and GRACE-FO satellite missions, the problems arising from temporal aliasing and an introduction to the Atmosphere and Ocean De-Aliasing Level-1B data product in general. Section 3 is based on the publication

Shihora, L., Sulzbach, R., Dobslaw, H. and Thomas, M. (2022): Self-attraction and loading feedback on ocean dynamics in both shallow water equations and primitive equations. Ocean Modelling, 169, 101914, 10.1016/j.ocemod.2021.101914

and describes the implementation of a frequently omitted feedback of mass redistribution on ocean dynamics into both a barotropic tidal model as well as the general circulation MPIOM which is also the basis for the oceanic component of AOD1B.

Section 4 describes the development of the new release of AOD1B (RL07) as well as tests and comparisons of the new dataset to the previous release RL06 using both GRACE K-band ranging and laser-ranging interferometer data as well as altimetry measurements. The section is based on the publication

Shihora, L., Balidakis, K., Dill, R., Dahle, C., Ghobadi-Far, K., Bonin, J. and Dobslaw, H. (2022): Non-Tidal Background Modelling for Satellite Gravimetry Based on Operational ECWMF and ERA5 Reanalysis Data: AOD1B RL07. Journal of Geophysical Research: Solid Earth, 127, 8, 10.1029/2022JB024360. This article is licensed under a Creative Commons Attribution 4.0 license

but also includes information from a co-authored publication

Ghobadi-Far, K., Han, S.-C., McCullough, C. M., Wiese, D. N., Ray, R. D., Sauber, J., **Shihora, L.**, and Dobslaw, H. (2022): Along-Orbit Analysis of GRACE Follow-On Inter-Satellite Laser Ranging Measurements for Sub-Monthly Surface Mass Variations. Journal of Geophysical Research: Solid Earth, 127, 2, 10.1029/2021JB022983

which features an additional regional comparison of the new AOD1B data to the previous release. The section includes also a discussion based on the co-authored publication

Balidakis, K., Sulzbach, R., **Shihora, L.**, Dahle, C., Dill, R., and Dobslaw, H. (2022): Atmospheric contributions to global ocean tides for satellite gravimetry. Journal of Advances in Modelling Earth Systems, 14, 11, 10.1029/2022MS003193

on the representation and estimation of atmospherically induced tidal signals that are present in the oceanic simulations, but were intentionally removed from the coefficients to make AOD1B a non-tidal product.

The following Section 5 then focusses on the stability of the newly released AOD1B data over both long and short time-scales and highlights its importance in satellite gravimetry applications. It is based on a third first authored publication

Shihora, L., Balidakis, K., Dill, R. and Dobslaw, H. (2023): Assessing the long-term stability of AOD1B atmosphere-ocean non-tidal background modelling for climate applications of satellite gravity data. Geophysical Journal International, Volume 234, Issue 2, August 2023, Pages 1063–1072, 10.1093/gji/ggad119. This article has been accepted for publication in Journal of Geophysical Research ©: 2023 Linus Shihora. Published by Oxford University Press on behalf of the Royal Astronomical Society. All rights reserved.

The last major section (Sect. 6) describes an updated estimation of the residual uncertainties as they are expected to be present in the new AOD1B RL07 as well as the computation of a new variance-covariance matrix to be used in simulation studies in the context of future satellite gravimetry missions. It is based on the corresponding preprint that was submitted to the Journal of Geodesy:

Shihora, L., Liu, Z., Balidakis, K., Wilms, J., Dahle, C., Flechtner, F., Dill, R., Dobslaw, H. (2023): Accounting for Residual Errors in Atmosphere-Ocean Background Models Applied in Satellite Gravimetry. Submitted to Journal of Geodesy. Reproduced with permission from Springer Nature.

While the text is based on the pre-print version, the final published paper can be found under 10.1007/s00190-024-01832-7.

Note, that the introductions and conclusions of all first-author publications are slightly adapted to better fit the overall structure of the thesis. The main parts, especially the results and overall conclusions, remain unchanged with respect to the original publication.

The thesis concludes in Section 7 with a summary of the overall results, their impact on satellite gravimetry and an outlook to further improvements in de-aliasing and future gravity missions.

2

Background

With AOD1Bs primary application being the processing of satelltite gravimetry data, this section starts with a reasonably brief description of the GRACE and GRACE-FO satellite missions. This includes an overview of the measurement principle, data processing chain and associated challenges. The next part of this section is dedicated to the difficulties arising from temporal aliasing, which have a major impact on the GRACE data and its processing. This then leads to the introduction of AOD1B and its application in satellite gravimetry. We introduce the components of AOD1B, some general technical details regarding its production and application, and the details of the previous version AOD1B RL06 which forms the starting point of the development for RL07.

2.1 Satellite gravimetry and GRACE

The Gravity Recovery and Climate Experiment (GRACE) was a satellite mission launched in March 2002 to actively monitor Earths time-variable gravity field using inter-satellite ranging measurements (Tapley et al., 2004). The primary mission lifetime was 5 years, operations have continued, however, until October 2017. A follow-up mission called GRACE Follow-On (GRACE-FO) (Landerer et al., 2020) was subsequently launched in May 2018 with the intent of continuing the monitoring of the changes in Earths gravity. Both satellite missions consist of two satellites orbiting the Earth in a low Earth orbit (LEO) of initially ∼500 km and a near-polar inclination of 89.5° with a distance of about 200 km between the spacecrafts. They are equipped with Global Positioning System (GPS) recievers for the tracking of each satellite with respect to the GPS constellation, star cameras which provide attitude information and accelerometers (GRACE-ACCs) in the satellites center of mass to measure non-conservative forces acting on the satellites. The primary measurement instrument, however, is a K-band ranging (KBR) instrument that provides continuous ranging measurements between the two satellites. In addition, the GRACE-FO satellites are equipped with a laser-ranging interferometer (LRI), offering a much higher signal to noise ratio compared to the KBR data.

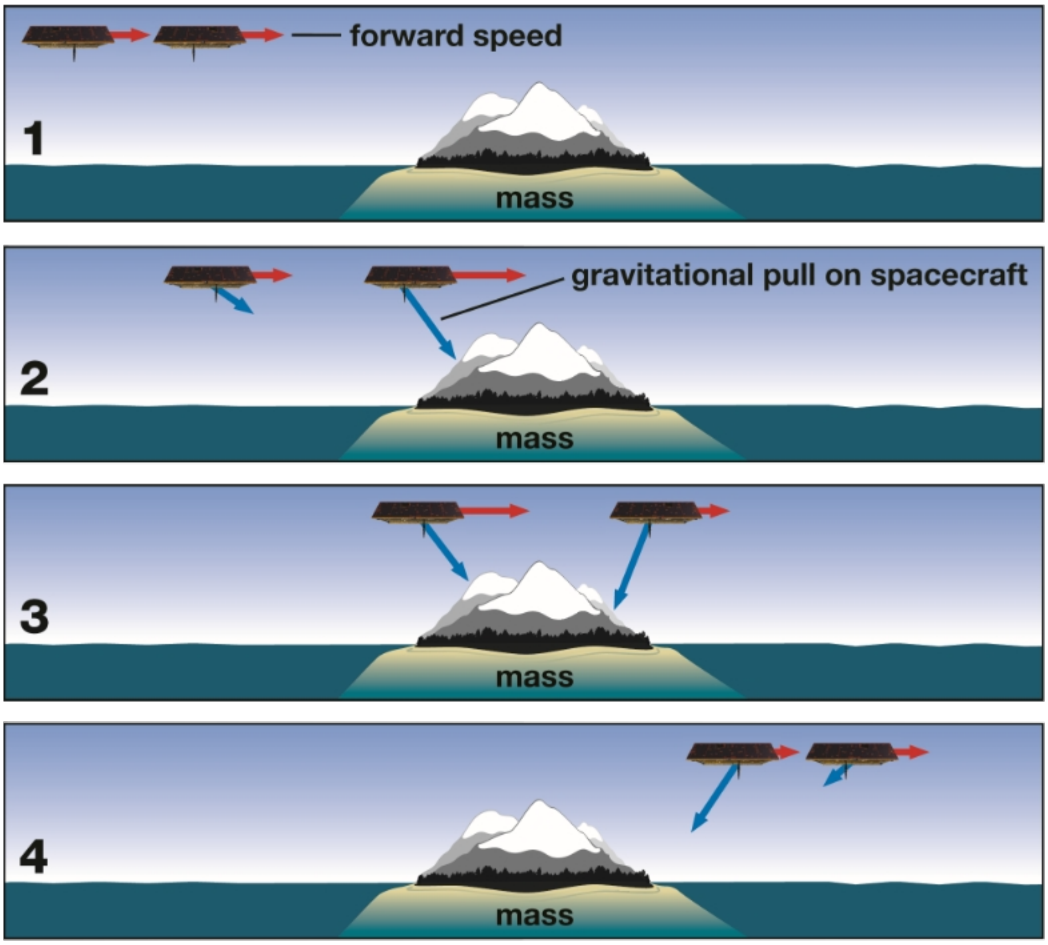

Figure 2.1: Illustration of the measurement principle of GRACE and GRACE-FO. Gravity anomalies along the track of the satellites affect the leading satellite first resulting in a measurable increase in the inter-satellite distance. As the trailing satellite catches up, the distance is reduced again. Measurements of the inter-satellite distance are thus sensitive to mass anomalies within and around the Earth. Image taken from https://gracefo.jpl.nasa.gov/resources/50/how-grace-fo-measures-gravity/.

The measurement principle of GRACE and GRACE-FO relies on the connection between changes in the Earths gravity field along the satellites path and the thus induced changes in the inter-satellite distance (Fig. 2.1). As the leading satellite travels over a (positive) gravity anomaly, it is pulled forward and the inter-satellite distance increases. Subsequently, as the second satellite travels over the anomaly, the satellite distance decreases again. Using the KBR and LRI instruments, these distance changes are measured with an accuracy of O(10μm) (Thomas, 1999). By combining the ranging data with the GRACE-ACC measurements, the gravity induced impact on the satellites can be separated from the non-gravitational forces such as drag from the residual atmosphere. In combination with the positioning data from GPS, star camera data and sufficient measurement time, a global map of the gravitational anomalies can be computed.

The satellite measurements are made publicly available to the scientific community to facilitate their use in a wide variety of geophysical applications as outlined in Sect. 1. Several stages, or levels, of data processing are made available as coordinated by the GRACE Science Data System (SDS). First, the raw satellite data is downloaded via GFZ's communication station in Ny-Ålesund and labelled as Level-0. Conversion to physical units and application of calibrations then yields Level-1a data which is further transformed to the correct reference frame, filtered and subsampled to produce Level-1b data (Wu et al., 2004). At this stage they are publicly available from the Jet Propulsion Laboratory (JPL) as well as the GeoForschungsZentrum (GFZ). Further processing is done by the official GRACE processing centres (Dahle et al., 2019a; Wiese et al., 2018; Save et al., 2016) as well as other institutions (e.g. Kvas et al. (2019)) with the aim to calculate Level-2 global gravity field solutions.

To derive a final map of the temporal anomalies in the gravity field, however, the satellite measurements need to be accumulated. The degree to which the global gravity field can be resolved heavily depends on the spatial coverage of the measurements on the Earth. Using GRACE data accumulated over one day, as an example, limits the maximum degree in terms of spherical harmonics to about 15 (Weigelt et al., 2013). As a consequence, the GRACE measurements are accumulated typically for 30 days to achieve a high spatial coverage before the computation of the final monthly gravity solution. As an alternative, daily gravity field solutions up to degree and order (d/o) 40 are available which rely on a combination of GRACE measurements and prior stochastic information in a Kalman smoother framework and thus require additional background information (Kvas et al., 2019; Mayer-Gürr et al., 2018).

2.2 Temporal aliasing

One of the major challenges in the computation of monthly GRACE gravity field solutions is known as temporal aliasing. Temporal aliasing in principle refers to the inability to correctly capture a high frequency signal if the sampling frequency is too small. More specifically, a harmonic signal with a frequency ω or period T can not be resolved with a sampling coarser than $\Delta t_{\mathrm{max}} = T/2$. The minimally required sampling frequency, i.e. half the signal frequency, is called the Nyquist frequency.
A simplified one-dimensional example of this phenomenon is given in Fig. 2.2. The subfigures show a single sine wave sampled using a decreasing sampling frequency. The original signal is resolvable until the sampling frequency matches half the original frequency, which is shown in the lower left panel. For a coarser sampling, the signal is not recoverable.

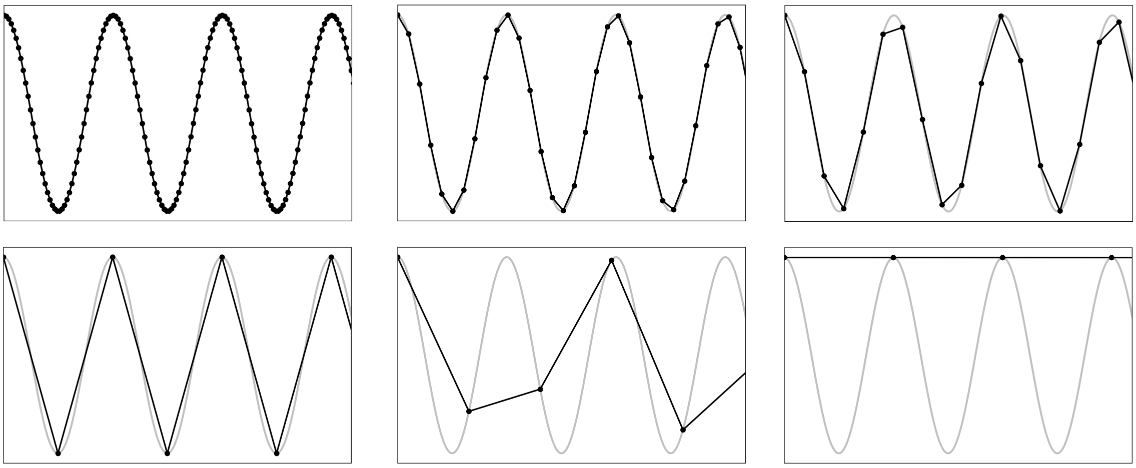

Figure 2.2: Illustration of the problem of temporal aliasing in one dimension. A pure sine wave (grey line) is sampled (black dots) with an increasing sampling distance. The signal can be recovered from the samples only up to the so called Nyquist frequency shown in the lower left. If the sampling frequency is smaller, the original signal can not be recovered and temporal aliasing arises. Adapted from Cushman-Roisin and Beckers (2011).

This is, of course, neither limited to single harmonic functions nor to one dimensional cases. For a more complex frequency spectrum, all frequencies above the Nyquist frequency will not be resolved and instead contribute to noise.

In the context of satellite gravimetry, GRACE measurements need to be accumulated for typically one month before the computation of the gravity field in order to achieve a high enough spatial sampling. Consequently, mass variations with frequencies below twice the GRACE accumulation period will not be recoverable in the gravity solution. This can be illustrated by a thought-experiment using GRACE ground track data. In Fig.

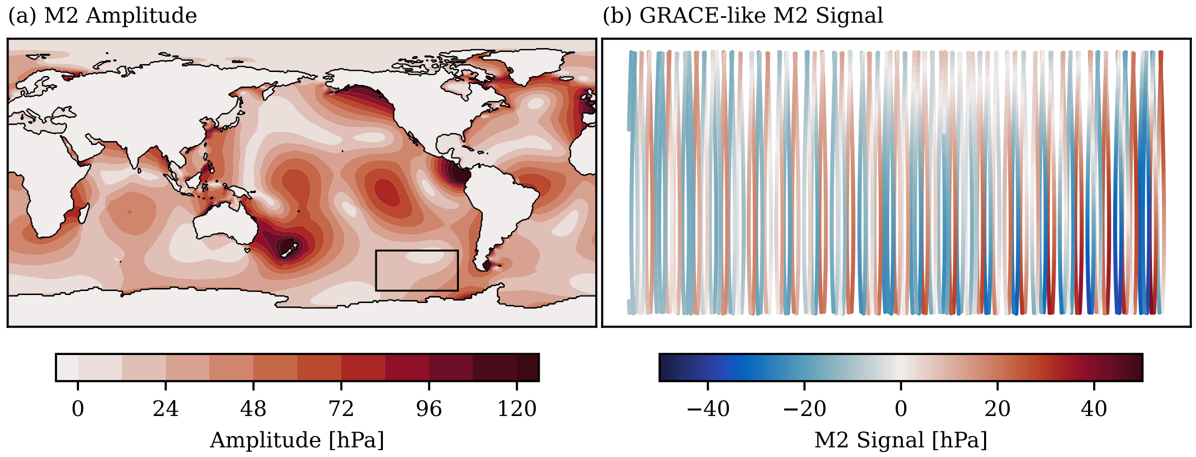

Figure 2.4: Impact of the M_2 tidal mass variations on the GRACE data as produced by a simplified simulation experiment. The amplitude of a simulated M_2 tidal time-series is shown in (a). The tidal amplitude is filtered using a 500km Gaussian filter and combined with GRACE-FO ground track data for Jan. 2019 to simulate what the satellites would record based on the tidal mass variations. GRACE-FO ground tracks coloured with the "seen" tidal signal are shown in (b) for the Bellingshausen Basin.

circulation model (OGCM) either globally or specifically for the Bellingshausen Basin. In subfigure (c) we again show the signal the GRACE-FO satellites would see based on the ground track pattern for January 2019 due to the non-tidal mass anomalies in the ocean. Also in this case, the original high-frequency mass variations are not recoverable. While these simulated examples simplify the real GRACE observation geometry, the need to account for the impact of temporal aliasing is clear. Especially considering that the signals to be recovered by GRACE measurements are of similar or even smaller magnitude that the high frequency variations in some cases.

To mitigate these effects of temporal aliasing, which are in reality a combination of signals from different sources, background models are typically applied in the GRACE processing. These background models offer a-priori information on the tidal and non-tidal variations and the simulated mass variations are subtracted in the gravity field estimation process during the computation of Level-2 solutions. As a result, the quality and accuracy of these background models has a direct impact on the amount of noise and the quality of the final monthly gravity solutions.

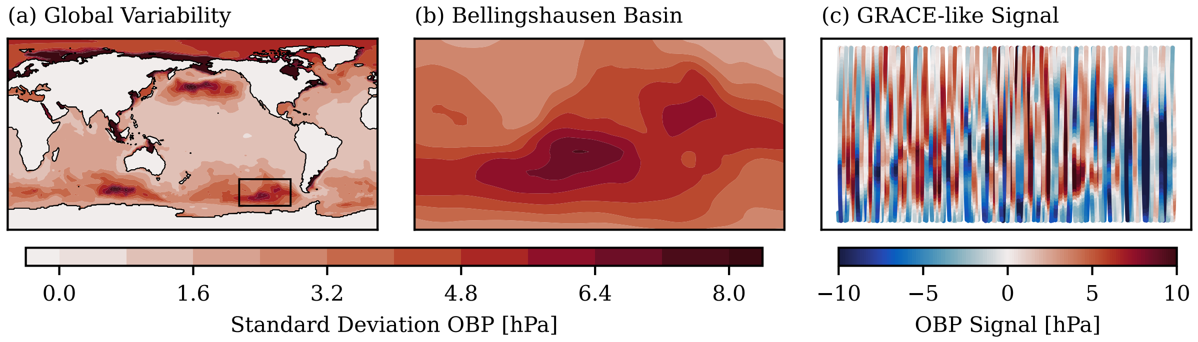

Figure 2.5: Impact of the non-tidal OBP mass variations on the GRACE data as produced by a simplified simulation experiment. The amplitude of a simulated OBP time-series is shown in (a) globally and in (b) for the Bellingshausen Basin. The signal is filtered using a 500km Gaussian filter and combined with GRACE-FO ground track data for Jan. 2019 to simulate what the satellites would record based on the non-tidal mass variations. GRACE-FO ground tracks coloured with the “seen” OBP signal are shown in (c) for the Bellingshausen Basin.

2.3 The Atmosphere and Ocean De-Aliasing Level 1B product

Various different processes contribute to the non-tidal high-frequency mass variations in the Earths atmosphere and oceans. In the atmosphere, changes in surface pressure (SP) on the order of O(10 hPa) are induced by advected weather systems and can have horizontal dimensions of several 100 km. Additionally, strong precipitation associated with advection and convection can temporarily increase the amount of water stored on the continents or fed into the oceans. In the oceans, mass variations at high frequencies are largely due to surface winds leading to a redistribution of water masses. These wind-driven barotropic changes are particularly pronounced in higher latitudes. Especially in the Southern Ocean, OBP variations can reach several 10 hPa in resonant basins (Fukumori et al., 1998). Differences in atmospheric surface pressure over the oceans can also drive relevant mass variations. For slowly varying pressure changes, on the order of several days, the ocean surface can be expected to compensate the atmospheric pressure anomalies which is also known as the inverted barometer effect (Gregory et al., 2019). However, at higher frequencies, i.e. daily or sub-daily, surface pressure anomalies induce lateral pressure gradients and thus changes in ocean dynamics and consequently ocean mass distribution.

All of these processes are prone to be the cause of temporal aliasing in monthly gravity solutions of satellite gravimetry, if unaccounted for. Thus, the Atmosphere and Ocean De-Aliasing Level-1B (AOD1B) data product offers the appropriate a-priori information on these mass variations and is one of the background models that is routinely applied in the Level-1b to Level-2 processing of satellite gravimetry (Dahle et al., 2019b).

There is in addition, a second application of AOD1B in the context of GRACE and GRACE-FO data processing. Other satellite observation systems, such as satellite altimetry, are primarily sensitive to surface properties of the Earth. In contrast, due to the unique measurement principle, GRACE data is sensitive to vertically integrated mass anomalies. This is an invaluable feature for applications where measurements independent of surface exposure are required such as in the analysis of terrestrial water storage (TWS) changes or ice mass loss. But it poses the additional problem of signal separation. In order to separate mass anomalies in the atmosphere and mass anomalies at or under the Earths surface, prior information is required which is also provided by AOD1B (Dobslaw et al., 2016a).

The information on the mass variations described by AOD1B comes from three major contributions. The first component are anomalies in atmospheric surface pressure. To that end, AOD1B utilises atmospheric reanalysis data from the European Centre for Medium-Range Weather Forecasts (ECMWF). This means that a single atmospheric model configurations is used over a long time-period and observational data is assimilated into the model to arrive at a representation of the state of the atmosphere that is as accurate as possible. It offers the additional benefit of a homogeneous spatial and temporal resolution as well as a consistency of the data for the entire length of the reanalysis due to the use of a single model configuration. In addition to reanalysis data, AOD1B also relies on operational ECMWF analysis data for the most recent years and for the operational production of AOD1B. The operational estimates are available with a low latency and thus allow for timely routine, i.e. daily, production of AOD1B. Additionally, frequent updates to the model and data assimilation scheme increase the quality regularly. Using atmospheric reanalysis data for a majority of the ADO1B product and then switching to the operational weather prediction model for the latest years thus offers the benefit of both products, provided that the transition between the two is performed with care and the consistency is carefully monitored through time, especially at epochs where changes to the operational model are performed.

As a second contribution, AOD1B considers the vertical structure of the atmosphere, i.e. anomalies in the density of the upper atmosphere. While these contributions are small compared to the impact of considering only the surface pressure anomalies, they are still relevant given the measurement precision of satellite gravimetry measurements (Swenson and Wahr, 2002) from GRACE and GRACE-FO.

The third contribution to AOD1B comes from the oceanic mass variations. These are based on unconstrained, transient simulations with a global OGCM forced with either the atmospheric reanalysis or operational analysis data. This includes forcing through surface wind stresses, wind speed, surface pressure, temperature and dew point temperature, cloud cover, solar radiation and precipitation. Global OBP fields are then stored from the simulation and used in the subsequent processing of AOD1B as they combine all contributions to the mass variations along the vertical line which incudes changes in the sea surface height but also changes in the density of the water column.

Technically, AOD1B is provided as sets of fully normalized Stokes coefficients (Heiskanen and Moritz, 1967) up to d/o 180 with a temporal resolution of three hours. This is a higher spatial resolution than the final monthly GRACE gravity field solutions, which are often produced as Stokes coefficients up to d/o 96 (Dahle et al., 2019b), but allows for future improvements in spatial resolution, especially considering future double-pair gravity missions. The first set of Stokes coefficients, called ATM, combine the contributions of atmospheric surface pressure and density anomalies of the upper atmosphere over the continents, as well as the static contribution to surface pressure to the OBP over the oceans. As a second set, the OCN coefficients contain the dynamic contribution to OBP over the oceans. The combination of ATM and OCN, labelled GLO coefficients, provide the full high frequency variations over the continents and ocean and are routinely applied as background model data in satellite gravimetry. Finally, the OBA coefficients, which are useful for oceanographic applications, provide the dynamic ocean bottom pressure data together with the static contribution from the atmosphere over the oceans but disregard the effects of upper air density anomalies. The separation of the mass anomalies into these different sets of coefficients allows not only the application in the de-aliasing of satellite gravimetry data but also allows users of the final GRACE solutions to re-add individual high-frequency contributions from the atmosphere or oceans which were subtracted in the calculation of the monthly gravity solutions. This then allows the use of GRACE data in applications that study e.g. oceanic or atmospheric mass variations (Dobslaw et al., 2016a).

Prior to the work presented in this thesis, AOD1B was in its sixth release (RL06) (Dobslaw et al., 2017). As mentioned in the previous section, Flechtner et al. (2016) showed deficiencies in the background modelling to be one of the largest contributors to the overall error in GRACE. While this study was based on AOD1B RL05 and while RL06 improved the representation of mass variations, residual deficiencies in AOD1B remain. This is especially the case for the oceanic component of AOD1B (Bonin and Save, 2020; Schindelegger et al., 2021) as it is not constrained by observations which is in contrast to the atmospheric ECMWF reanalysis data. As such, while improvements in the representation of atmospheric mass anomalies certainly have a positive impact on the de-aliasing, improvements in the oceanic component of AOD1B offer the opportunity for the largest improvement to the overall quality of a new release of AOD1B and as a consequence also to the final monthly gravity field solutions from satellite gravimetry.

3

Self-attraction and loading feedback on ocean dynamics in both shallow-water equations and primitive equations

The Earth is not a rigid body but is deforming in response to both internal and external forces on various time-scales. Deformations are accompanied with a redistribution of masses within the solid Earth that modify the Earth's external gravity field. Water mass distributions that deviate from the geoid cause a redistribution of mass within the solid earth, accompanied by a horizontal movement of water masses due to changes in the Earth's gravity field. Together with the self-gravitation of water masses, these effects are commonly referred to as the self-attraction and loading (SAL) feedback to ocean dynamics.

SAL was first identified to be important for the evolution of sea-level over the last glacial cycle (Farrell, 1972). Accumulation of ice on the continents reduced the amount of water in the oceans and led to a global mean sea-level more than 100 m lower than present-day. Local relative sea-level as measured with respect to the (deforming) solid Earth, however, was found to deviate from the global mean, and can be only explained by solving the so-called sea-level equation (Farrell and Clark, 1976). More recently, continental surface mass estimates as obtained with GRACE (Tapley et al., 2004) and GRACE-FO (Landerer et al., 2020) monitor the spatially variable barystatic sea-level with monthly temporal sampling (Tamisiea et al., 2010). In all those applications, it is implicitly – and appropriately – assumed that the ocean mass distribution adapts quasi-instantaneously to the changes in the gravity field.

For mass distributions at diurnal time-scales, however, this assumption is not valid. Global ocean tides have been known for a long time already to be affected by SAL due to the delayed response to the rapidly varying forcing (Henderschott, 1972; Farell, 1973). Whereas many simplifications have been tested in the past for the proper inclusion of SAL effects into global numerical models (e.g., Accad and Pekeris (1978)), it is now widely accepted that the full effect of SAL from solving the global convolution integral is required to meet the accuracy requirements of present-day satellite missions (Ray, 1998). While the influence on the high-frequency non-tidal dynamics is also undisputed (Stepanov and Hughes, 2004), it has received far less attention. Previous studies (Vinogradova et al., 2010; Riva et al., 2010) have focussed on longer time-scales, whereas the impact on the high-frequency ocean dynamics, which is especially relevant for satellite gravimetry (Schindelegger et al., 2021), will be the focus of this section.

Here, we will briefly highlight the theory for calculating the SAL potential (Sect. 3.1). Next, we describe the numerical implementation of the SAL feedback into a global ocean tide model based on the shallow-water equations (Sect. 3.2), as well as into the OGCM to be used for AOD1B RL07 based on the primitive equations (Sect. 3.3) where we also discuss the influence of including surface pressure anomalies over land in the SAL contribution, as well as the influence of the mean OBP field. Results are presented for both simulations of ocean tidal dynamics as well as for the non-tidal ocean circulation. The section closes with a summary and a discussion of the relevance of SAL feedbacks for satellite applications (Sect. 3.4).

For completeness, we note that Gregory et al. (2019) recently suggested to summarize the feedback of self-attraction and loading on ocean dynamics under the more generic name "gravity, rotation, and deformation (GRD)". We note that rotational feedbacks are not considered in this study, and are certainly also not relevant for inclusion into numerical ocean models due to the rather slow variations in both the position of the pole and the rotational rate of the Earth. In order to avoid confusion by introducing a name that prominently includes rotation which is never considered in this thesis, the term SAL is used in the following.

3.1 On self-attraction and loading

We start with the theoretical formulation for SAL which forms the basis of the implementations into both ocean models. The formulation is based on deriving an additional potential term which describes the additional gravitational potential due to an anomalous water mass on a spherical shell as well as the effect of the elastic deformation of the solid earth. After Kuhlmann et al. (2011) the gravitational potential at a point $\boldsymbol{p}$ induced by a point mass m at a point $\boldsymbol{q}$ is given by:

$$V(\boldsymbol{p}) = G\frac{m}{\overline{\boldsymbol{pq}}}. \tag{3.1}$$

Here G represents the gravitational constant and $\overline{\boldsymbol{pq}}$ the distance between the two points. The total potential at point $\boldsymbol{p}$ due to the entire ocean mass distribution is then given by the integral over the ocean domain. Considering the relative difference between the ocean depth and the Earth radius R we make the approximation that the mass of the ocean is distributed on an infinitely thin shell and thus given by the surface mass density σ.

$$V(\boldsymbol{p}) = G\iint_S \frac{\sigma(\boldsymbol{q})}{\overline{\boldsymbol{pq}}}\mathrm{d}S \tag{3.2}$$

After Abramowitz and Stegun (1972) the distance $\overline{\boldsymbol{pq}}$ can be expressed by the Earth's radius R and the solid angle Ω between the two points:

$$\overline{\boldsymbol{pq}} = 2R\sin\left(\frac{\Omega}{2}\right) 9R\sqrt{2-2\cos\Omega}. \tag{3.3}$$

The above relation can now be rewritten yielding the generating function for a series of Legendre Polynomials

$$\frac{R}{\overline{\boldsymbol{pq}}} = \frac{1}{\sqrt{2-2\cos\Omega}} = \sum_n^\infty P_n(\cos\Omega) \tag{3.4}$$

and inserted into Eq. 3.2 this gives:

$$V(\boldsymbol{p}) = \frac{G}{R}\sum_n^\infty \iint_S \sigma(\boldsymbol{q})P_n(\cos\Omega)\mathrm{d}S. \tag{3.5}$$

The surface mass density σ can be decomposed into spherical harmonics (Wahr et al., 1998) giving

$$\sigma_n(\lambda,\phi) = \frac{2n+1}{4\pi R^2}\iint_S \sigma(\lambda',\phi')P_n(\cos\Omega)\mathrm{d}S. \tag{3.6}$$

Inserting this into the equation for the potential (Eq. 3.5) results in:

$$V(\boldsymbol{p}) = \frac{3g}{\rho_e}\sum_{n=0}^\infty \frac{\sigma_n(\lambda,\phi)}{2n+1}, \tag{3.7}$$

with $G = \frac{gM_e}{R^2}$ and the Earth's density $\rho_e = \frac{3M_e}{4\pi R^3}$. Finally, we note that the surface mass density in spherical harmonics can be expressed by ocean bottom pressure anomalies

$p'_{B,n} = \sigma_n g$, yielding:

$$V(\boldsymbol{p}) = \frac{3}{\rho_e} \sum_{n=0}^{\infty} \frac{p'_{B,n}}{2n+1}. \tag{3.8}$$

This description thus relies on the decomposition of OBP anomalies into spherical harmonics $p'_{B,nm}$. The pressure values over the continents can either be set to zero or, as in the case for non-tidal simulations, also include atmospheric surface pressure anomalies (Sect. 3.3.2). The inclusion of the elastic deformation of the sea floor as well as the subsequent change in the gravitational potential of the Earth are described by the Love numbers h'_n, k'_n (Munk and MacDonald, 1960) for which we use data given by Wang et al. (2012) based on the PREM model of the solid Earth. The final SAL potential including all three effects is then given by (Kuhlmann et al., 2011):

$$V(\boldsymbol{p}) = \sum_{n=0,|m|<n}^{\infty} (1 + k'_n - h'_n)\ \alpha'_n\ p'_{B,nm}(\boldsymbol{p}) \quad , \quad \alpha'_n = \frac{3}{\rho_e(2n+1)}. \tag{3.9}$$

As the full implementation of SAL requires significant computational overhead due to the decomposition into spherical harmonics in each time-step, different approximations have been suggested in the past. Most notably, Accad and Pekeris (1978) proposed neglecting the degree dependence in Eq. 3.9 and using only a single term of the series. This implies the assumption that the SAL effects are dominated by a specific spatial scale. The spherical harmonic expansion of the $p'_{B,n}$ field is then superfluous and Eq. 3.9 simplifies to

$$V(\boldsymbol{p}) = \beta\ \alpha_0\ p'_B. \tag{3.10}$$

The approximation is called β-approximation and is also implemented and tested in the following.

3.2 Barotropic tidal modelling

The barotropic ocean tide model TiME (**Ti**dal **M**odel forced by **E**phemerides) used in this study was initially developed in Hamburg, Germany (Zahel, 1977, 1978). Since then, TiME has been constantly developed (Seiler, 1991; Thomas and Sündermann, 1999; Weis et al., 2008) and was upgraded most recently by adding dissipation mechanisms, refining numerical grids and updating the bathymetric map (Sulzbach et al., 2021). In the following we give a short introduction to the theory of tides and the employed validation metrics and introduce the model specifications. Finally, we present simulation results with respect to the influence of SAL for a selection of partial tides and show that while the importance of considering the full SAL-forcing is smaller for long-period tides, it cannot be neglected to achieve high accuracy results.

3.2.1 Tidal excitation and validation metrics

Astronomical tides are excited by the periodically varying gravitational attraction of celestial bodies, primarily the Sun and Moon. The resulting lunisolar tide-raising potential $V_{tid}(t, \phi, \lambda)$, that is also influenced by the solid Earth response to tidal forces (body tides) (Henderschott, 1972) can be decomposed in time into a set of so-called partial tide potentials $V_i(t, \phi, \lambda)$, that oscillate at discrete frequencies ω_i and exhibit spatial patterns, that follow the real-valued spherical harmonics Y_{nm} as given by Hartmann and Wenzel (1994, 1995). The individual partial tide frequencies hereby relate to characteristics of the dynamics of celestial bodies and can be described in terms of the 6-digit Doodson-numbers (Doodson, 1921).

The time-dependent, horizontal gradients of V_i induce harmonic, barotropic forces that excite ocean tide dynamics oscillating at the given frequency. The obtained partial tide response patterns hereby depend on the respective tidal frequency ω_i, the degree n and order m of the respective exciting spherical harmonic potential and, less strongly, on the excitation amplitude V_i^0. To validate the numerical results obtained with a tidal model we will focus on the induced oscillations of the free ocean surface

$$\zeta^i(t, \phi, \lambda) = \zeta_{cos}^{\omega_i} \cos \omega_i t + \zeta_{sin}^{\omega_i} \sin \omega_i t + (\text{nonlin.}) \quad , \tag{3.11}$$

that contain minor constant and higher frequency components as the result of weakly non-linear processes, that are ignored in the following. Thus, a partial tide can be entirely specified by the complex elevation-function $\zeta^i = \zeta_{cos}^{\omega_i} + i\zeta_{sin}^{\omega_i}$. Tidal elevations simulated in this study will be compared to the data-constrained tidal model FES14 ((Lyard et al., 2006), updated) by evaluating the respective mean deviation in terms of the root-mean square averaged over one tidal period

$$\text{RMS}(\zeta_1^i, \zeta_2^i) = \sqrt{\frac{1}{2}|\zeta_1^i(\mathbf{x}) - \zeta_2^i(\mathbf{x})|^2} \ . \tag{3.12}$$

This value can further be averaged over a defined oceanic domain D_o by evaluating

$$\overline{\text{RMS}}_{\zeta_1^i, \zeta_2^i} = \sqrt{A_o^{-1} \sum_{j,k \in D_o} A_{jk} \left(RMS_{\zeta_1^i, \zeta_2^i}^{jk} \right)^2} \ , \tag{3.13}$$

where A_{jk} are surface elements, that add up to the surface of the considered domain $A_o = \sum_{j,k \in D_o} A_{jk}$.

We distinguish between deep/shallow (limit: $H = 1000$m) and polar/non-polar (limit:

Table 3.1: $\overline{RMS}$ (cm) between TiME and FES14 averaged over certain oceanic domains and for an open ocean tide gauge (tg) data set: d = deep, sh=shallow, p=polar and np=non-polar relate to oceanic domains, as defined in Sect. 3.2.1. Additionally, Doodson coefficients, degree and order (d/o) (n,m) of exciting spherical harmonic function and excitation frequencies ω for the respective tides are shown.

Domain	151 tg	(d,np)	(sh,np)	(d,p)	(sh,p)	global
$\boldsymbol{M_2}$ (255.555), $\omega = 28.98410$ °/h, (n,m) = (2,2)						
$d/o = 1024$	4.83	3.39	17.97	3.40	11.88	6.48
$\beta = 0.1$	6.69	5.41	27.26	6.47	19.09	10.02
$\beta = 0.$	27.02	22.90	42.90	19.42	29.38	25.33
$\boldsymbol{K_1}$ (165.555), $\omega = 15.04107$ °/h , (n,m) = (2,1)						
$d/o = 1024$	1.32	0.90	5.74	1.81	4.20	2.03
$\beta = 0.07$	2.71	2.02	6.76	3.16	4.75	2.89
$\beta = 0.1$	1.91	1.28	7.84	2.47	5.00	2.75
$\beta = 0.13$	2.42	1.65	10.16	2.56	5.73	3.50
$\beta = 0.$	5.72	4.31	9.03	6.11	6.94	5.04
$\boldsymbol{M_f}$ (075.555), $\omega = 1.09803$ °/h , (n,m) = (2,0)						
$d/o = 1024$	/	0.06	0.34	0.17	0.23	0.12
$\beta = 0.1$	/	0.13	0.36	0.29	0.65	0.20
$\beta = 0.$	/	0.20	0.93	0.56	1.86	0.24

$|\phi| = 66°$) areas to build four distinct oceanic domains. This choice allows to focus on areas that can be optimally captured by altimetry-constrained models (non-polar ocean), or purely-hydrodynamic models (deep ocean). Further we compare the results to the "ground-truth" of tide-gauge stations (tg) by averaging over a set of $N_{tg} = 151$ stations compiled by Ray (2013), where we evaluate Eq. 3.13 by averaging the RMS obtained at the individual gauges ($A_{jk} = A_n = 1$; $A_0 = N_{tg}$). The derived metrics can be used to quantify the model performance. We will predominantly relate to the here-defined deep, non-polar metric that comprises over 80% of the ocean surface.

3.2.2 Shallow-water equations

Tidal dynamics are calculated by integrating the non-linear, shallow-water equations (e.g. (Pekeris, 1974; Schwiderski, 1980))

$$\partial_t \mathbf{v} + \mathbf{f} \times \mathbf{v} + (\mathbf{v} \cdot \nabla)\, \mathbf{v} = -g \boldsymbol{\nabla} \zeta + \boldsymbol{\nabla} \left(V_i + V \right) - \mathbb{D}\ , \tag{3.14}$$

$$\partial_t \zeta = -\boldsymbol{\nabla} \left(\left(H + \zeta \right) \, \mathbf{v} \right) \tag{3.15}$$

employing a temporal finite-difference scheme (Backhaus, 1985) spanned on a global ϕ/λ-grid at $\frac{1}{12}^\circ$-resolution. The barotropic ocean state is described by $\boldsymbol{\zeta}^i = (\mathbf{v}^i, \zeta^i)$, where ζ^i is the free surface elevation and $\mathbf{v}^i$ is the barotropic flow velocity. Additional parameters are the Coriolis vector $\mathbf{f} = 2\Omega\sin(\phi)$, the bathymetric function $H(\lambda, \phi)$ and the mean surface gravity $g = 9.80665\frac{m}{s^2}$. The tidal excitation in the here employed "partial tide mode" is induced by astronomical forces proportional to $\boldsymbol{\nabla} V_i$ as well as by SAL-Forcing $\boldsymbol{\nabla} V$. The full SAL-effect is included by decomposing the surface mass density into spherical harmonics up to a certain maximum degree and order l_{max} and evaluating Eq. (3.9). The in terms of spherical harmonic functions computed SAL potential is then subsequently transformed back into the spatial domain before application in the model. The computational burden is thus shifted to transforming information between spectral and spatial domain. Since this is efficiently handled by the SHTns-package (Schaeffer, 2013), the computation time increases only moderately by $\sim 15\%$ for each time-step. Alternatively it is possible to employ the β-parametrization discussed above.

TiME possesses three dissipation mechanisms summarized by

$$\mathbb{D} = \frac{r}{H}\,|\mathbf{v}|\mathbf{v} - A_h \hat{\boldsymbol{R}}'\mathbf{v} + \frac{\kappa}{H}\mathbb{C}\mathbf{v}\ . \tag{3.16}$$

This includes the quadratic bottom friction term with friction coefficient $r = 0.003$, linear wavedrag-dissipation introduced by the Nycander-tensor $\mathbb{C}$ (Nycander, 2005) and a tuning coefficient κ as well as a linearly parametrized horizontal eddy-viscosity-scheme proportional to coefficient A_h, where $\hat{\boldsymbol{R}}'$ is a partial differential operator acting on $\mathbf{v}$ that is defined in Sulzbach et al. (2021). While sea-ice is not considered in the model, we note that cavities under the Antarctic ice shelf are included in the spatial domain of the simulations.

3.2.3 Simulation results

We employ model settings, that were found to result in very accurate results for multiple partial tides ($A_h = 2 \cdot 10^4 \frac{m^2}{s}$, $\kappa = 1.25$, rtopo2-bathymetry, arg/chi-grid) (Sulzbach et al., 2021). Several experiments are performed individually for three different partial tides from the semi-diurnal (M_2), diurnal (K_1) and long-period tidal band (M_f). The K_1- and M_2 experiments are initialized for 30 days, when tidal elevations have equilibrated well below a precision of 1 mm (compare e.g. Schindelegger et al. (2018)). As in this situation the sea surface dynamics can be precisely described by Eq. 3.11, only the last simulated period is used to extract the respective partial tide, the first overtide and a residual, constant component as a consequence of tidal rectification. The M_f-run is spun up for 2 complete periods, where the constituents were derived by the following third period.

The time-step is set to $\frac{1}{240}(M_2)$, $\frac{1}{480}(K_1)$, $\frac{1}{6720}(M_f)$ of the respective tidal period, yielding numerical values of close to 180 seconds in each case.
A first simulation includes the full SAL-effect by evaluating Equation (3.9) up to $d/o = 1024$, which is a sufficient degree to resolve the SAL-effect to a sub-mm level in the open ocean (Schindelegger et al., 2018). Additional experiments employ the β-parametrization at various values β, where $\beta = 0$ corresponds to entirely ignoring dynamical feedback by SAL.

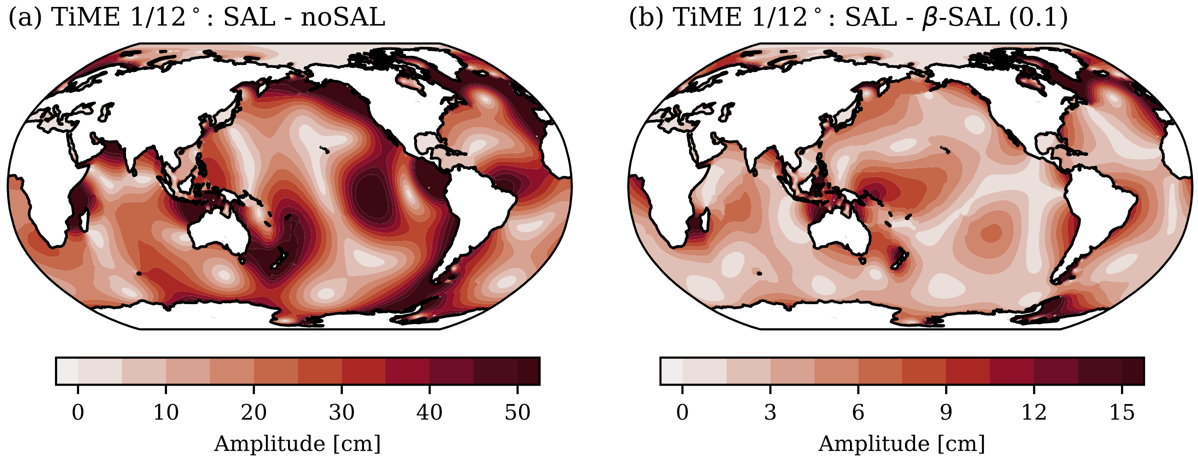

Figure 3.1: Amplitudes of the complex differences for the M_2 constituent between SAL and noSAL (a) as well as SAL and $\beta = 0.1$-parametrization (b) model runs for TiME at $\frac{1}{12}^{\circ}$-resolution.

Table 3.1 summarizes the validation results for several domains for the three experiments and Fig. 3.1 shows deviations in between individual solutions for M_2.

M_2-tide

Considering the full SAL-effect for the main lunar M_2-tide leads to a non-polar open ocean RMS of 3.39 cm (Sulzbach et al., 2021). The consideration of the $\beta = 0.1$-parametrization leads to a strong increase of this value (+60%) and a complete neglection is even more fatal to accuracy (+576%). RMS-values for shallow and/or polar regions show similar tendencies, but the accuracy drop in shallow water areas is smaller due to TiME's generally worse performance in shelf seas.

K_1-tide

Repeating the same experimental setup leads to an increase in RMS of (42/379)% when setting $\beta = (0.1/0)$. Further experiments were conducted for $\beta = (0.07/0.13)$ yielding worsened open ocean RMS values in comparison to $\beta = 0.1$. While this proves the default setting $\beta = 0.1$ as robust concerning open ocean dynamics of diurnal tides, the shallow non-polar RMS increase was lowest when setting $\beta = 0.07$ (18%), while $\beta = 0.13$ (77%) even worsened the results compared to neglecting the effect completely (+57%, values for non-polar areas). This can be explained by considering the typical scales of oscillation systems in shelf areas in comparison to the open ocean: since this scale is much smaller, tidal loads on contra-phasic points influence each other by partially annihilating the effect of the load. This results in locally diminished values of the β-parametrization.

M_f-tide

Having a half-monthly period, the M_f-oscillation system is less dynamic and much closer to an equilibrium tide description. Nevertheless, the non-polar open ocean RMS increases by (117/233)%, when parametrizing SAL as $\beta = (0.1/0)$. This increase is similar for global ocean dynamics, but much more moderate than the impact obtained for semi-diurnal and diurnal tides.

The results indicate that a full representation of the SAL-effect is necessary to obtain the highest accuracy results for all considered tidal species that exhibit periods in the range from 12 h to 14 d. Hereby the impact decreased for lower oscillation frequencies. This points to the decreasing dynamic feedback of SAL back into tidal dynamics that ultimately leads to consideration of the self-consistent equilibrium tide, where dynamic feedback is fully suppressed. Further, the larger scales of the amphidromic systems for K_1 and M_f that by far extend the near-field effects of loading Greens function improve the accuracy of the β-approximation in the open ocean.

3.3 Primitive equations

The dynamic feedback of SAL has been introduced also into the Max-Planck-Institute for Meteorology Ocean Model (MPIOM) (Jungclaus et al., 2013), which is a direct descendant of the Hamburg Ocean Primitive Equation Model (HOPE) (Drijfhout et al., 1996; Wolff et al., 1997). MPIOM is a free surface general circulation model that solves the primitive equations under the hydrostatic and Boussinesq approximations (Marsland et al., 2003). The model is discretised horizontally on an Arakawa-C grid and vertically on a z-grid. The atmospheric forcing includes wind stress, heat- and freshwater fluxes, and optionally also atmospheric surface pressure. Lunisolar gravitational tidal forcing (Thomas et al., 2001) can be additionally employed. The ocean model includes both a dedicated sea-ice model (Marsland et al., 2003) as well as cavities underneath the Antarctic shelf-ice. MPIOM has been used for AOD1B RL06 (Dobslaw et al., 2017) and is set to be used for

RL07 as well, which will be the subject of later chapters of this thesis.

The full implementation of SAL according to Eq. 3.9 is kept as close as possible to the implementation in TiME. At every time-step ocean bottom pressure anomalies (OBA) are calculated with respect to a pre-computed mean OBP field. The OBA field is then remapped from MPIOMs internal tri-polar grid to a 720x360 Gaussian grid in preparation for the transformation to spherical harmonics (SHs). For the SH transformation we utilise, as in TiME, the SHTns library by Schaeffer (2013) and expand to d/o 179. The calculation of the SAL potential follows Eq. 3.9 before the back-transformations into the spatial domain and to the internal MPIOM grid are performed. The gradient of the thus obtained additional potential is then applied in parallel, although independently, to MPIOMs tidal potential. For the implementation of the scalar approximation the above described process is simplified significantly. Instead of the spatial and spectral transformations the OBA field is used to compute the approximated potential according to Eq. 3.10 with a scalar factor of $\beta = 0.1$.

For this study, we utilise MPIOMs medium-resolution TP10L40 configuration which uses a 1.0° tri-polar grid horizontally with 40 vertical layers. The model time-step is set to 20 minutes. The ocean model is spun-up for 1000 years from 3D temperature and salinity climatologies (Levitus et al., 2005) with cyclic atmospheric forcing with daily sampling (Röske, 2005). Note that this spin-up is later extended to 2000 years in the production of AOD1B in order to further diminish the artificial model drifts. Following the spin-up, transient simulations are performed with hourly atmospheric forcing based on the ECMWF ERA5 re-analysis (Hersbach et al., 2020) including atmospheric pressure forcing. Hourly snapshot OBP fields are generated as output regularly. All experiments discussed below are two years long, whereas only the last year will be analysed in the following.

3.3.1 Experiments with tidal forcing

MPIOM provides the option to simulate lunisolar gravitational tides for the benefit of studying non-linear interactions among the general circulation and tidal dynamics (Thomas et al., 2001). We use an experiment with MPIOM under both atmospheric and gravitational forcing, but isolate the signature of the M_2 by means of least-squares adjustment from the hourly sampled OBP fields. For simplicity, simulated sea surface height variations from TiME are converted to OBA.

We here compare three model runs using either the full SAL implementation according to Eq. 3.9, the scalar approximation according to Eq. 3.10 or no SAL potential. Fig. 3.2 shows the amplitudes of the complex differences for the M_2 constituent between the

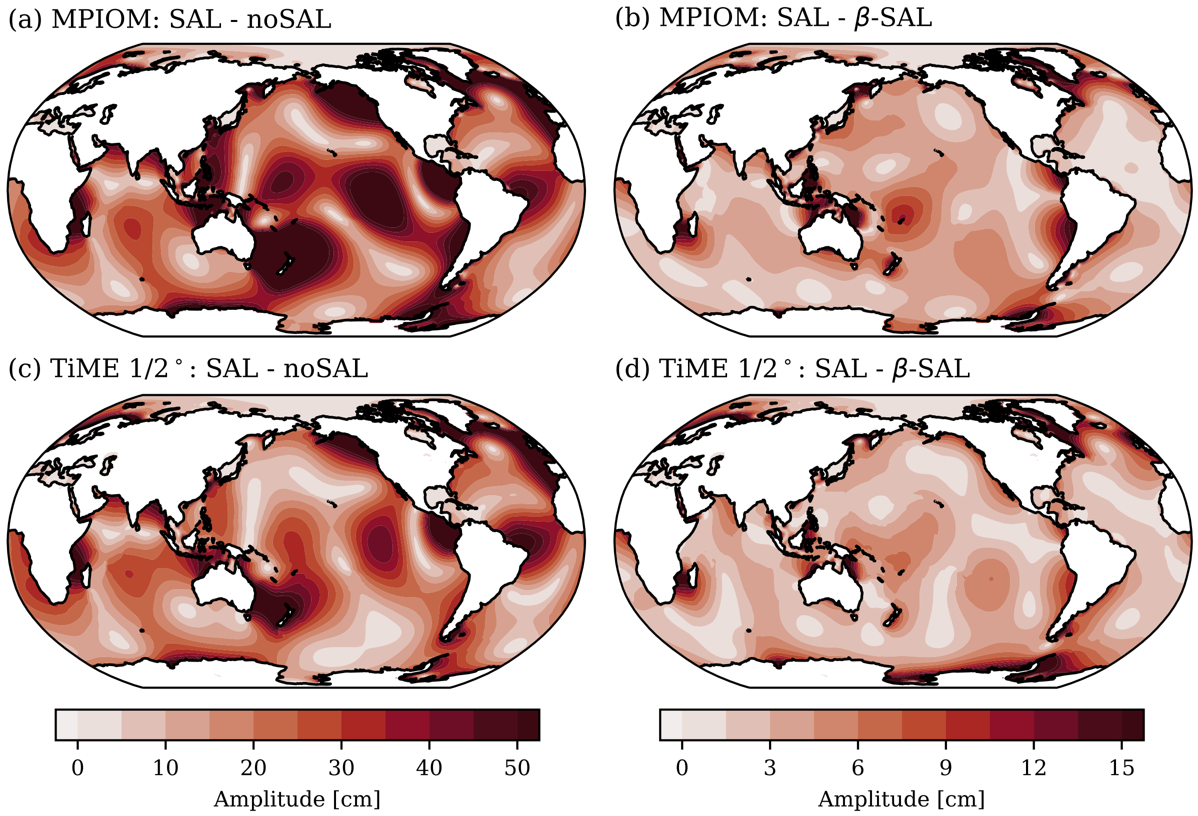

Figure 3.2: Amplitudes of the complex differences for the M_2 constituent between SAL and noSAL (left) as well as SAL and β-SAL (right) model runs for MPIOM (top) and TiME (bottom).

fullSAL and noSAL simulations (left) and between the fullSAL and β-SAL simulations (right) performed with MPIOM (top - a & b) and TiME (bottom - c & d) at a resolution of $\frac{1}{2}^{\circ}$.

For both MPIOM and TiME, the fullSAL implementation produces complex differences of more than 50 hPa in regions with a large M_2 amplitude. However, while the results are qualitatively in good agreement, the SAL influence in MPIOM is in these areas about 30% larger, which might be related to the rather long time-step in MPIOM that is not well suited to represent rapid semi-diurnal fluctuations.

Comparing the influence of the scalar approximation to the full SAL implementation (Fig. 3.2 b and d) shows that both MPIOM and TiME produce a difference in amplitude of up to 15 hPa. The largest differences are here confined to coastal areas such as the Coral and Celebes Sea, the Sea of Okhotsk and the south-eastern Pacific Ocean. In the open ocean the difference in complex amplitude between the two model runs reaches about 5 hPa. As the choice of β in the scalar approximation signifies a predominance of a specific spatial scale, a larger difference in coastal areas is to be expected. According to Ray (1998) and Stepanov and Hughes (2004), $\beta = 0.1$, while being the best choice for a constant factor,

Table 3.2: $\overline{RMS}$ (cm) between MPIOM and FES14 averaged over certain oceanic domains and for an open ocean tide gauge (tg) data set: d = deep, sh=shallow and np=non-polar relate to oceanic domains, as defined in Sect. 3.2.1.

Domain	151 tg	(d,np)	(sh,np)	global
no SAL	25.87	23.35	38.60	24.64
full SAL	10.88	10.52	35.90	14.66

represents the influence of SAL in shallower regions only poorly.

Similar to the validation performed for the results obtained with TiME, we here also validate the results for several domains for the M_2 results obtained from MPIOM in Tab. 3.2.

The results are computed analogously to the results from TiME. For MPIOM, considering the full SAL-effect for the main lunar M_2 tide leads to a reduction of the non-polar open ocean RMS from 25.87 to 10.88 cm, which represents a reduction of about 58%. For the shallow water areas the reduction in RMS is reduced in a similar way to the results from TiME, which is also connected to the generally worse performance in shelf areas. We note, however, that the results obtained here are meant to demonstrate the implementation of SAL in MPIOM and are not to be compared to the results from TiME in terms of absolute values. Naturally, MPIOM is not able to compete with TiME when it comes to the simulation of tides, which is of course also reflected in the RMS values. Instead, emphasis should be placed on the improvement obtained from the SAL feedback within each model, which suggests that similar improvements should also be visible in MPIOM for non-tidal dynamics.

3.3.2 Impact of SAL on non-tidal dynamics

We also perform experiments with MPIOM to investigate the effects of SAL on the circulation. We will focus on OBP first, since this is the quantity most directly affected by SAL and of importance for satellite gravimetry through AOD1B. The experiments differ in the treatment of SAL and include either the full SAL potential as given by Eq. 3.9 (here labelled SAL-OBP) where the values over the continents are set to zero, the full SAL potential including contributions from surface pressure anomalies over land (SAL-SPOBP), the simplified SAL potential as given by the scalar approximation of Eq. 3.10 (β-OBP) with $\beta = 0.1$ or no SAL contribution whatsoever (noSAL). Please note that gravitational tides are not simulated in those experiments and that the ocean response to atmospheric tides (Dobslaw and Thomas, 2005) has been removed from the time-series of each experiment empirically.

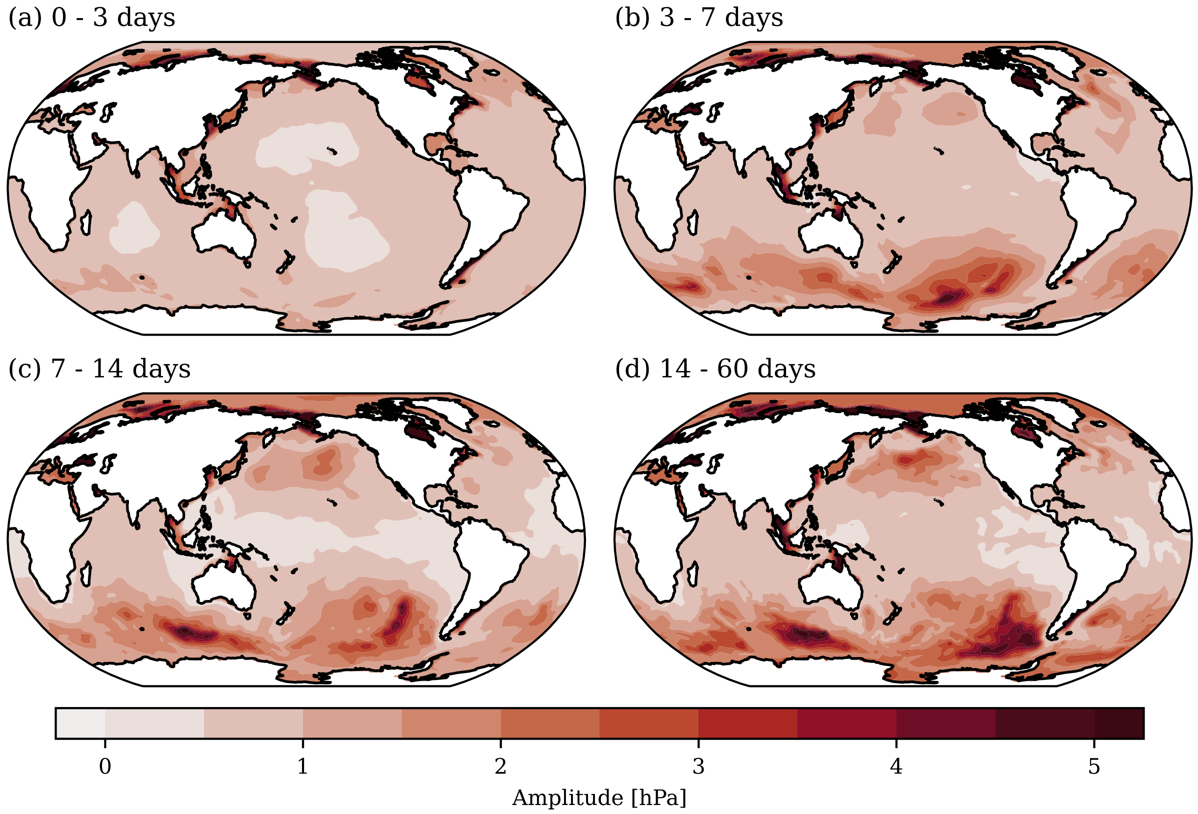

Figure 3.3: Standard deviation of OBA for the SAL-SPOBP model run. The results are separated into four frequency bands using a series of Butterworth filters: 0 - 3 days (a), 3 - 7 days (b), 7 - 14 days (c), 14 - 60 days (d).

The results are analysed by separating the OBA time-series into four frequency bands of 0 - 3 days, 3 - 7 days, 7 - 14 days and 14 - 60 days using 4th order Butterworth filters. Longer frequencies will not contribute to potential aliasing effects for monthly gravity solutions in satellite gravimetry. In Fig. 3.3 we show the variability of OBP, split into the aforementioned frequency bands, for the SAL-SPOBP model run as a reference. At the highest frequencies (0 - 3 days), the variability predominantly consists of basin modes that are locally enhanced in various semi-enclosed coastal regions. Spatial scales gradually reduce with longer periods and signals become more spatially variable. Signals in OBP at the longest periods considered here are particularly pronounced in various resonant regions in the Southern Ocean (e.g., Indoaustralian Basin, Bellingshausen Basin), where barotropic ocean dynamics are excited by the strong and rapidly varying westerly surface winds.

To isolate the effect of different SAL aspects on OBP variability, we calculate standard deviation differences between model runs for each frequency band. Fig. 3.4 shows the standard deviation differences of the SAL-SPOBP and noSAL model runs. For the high

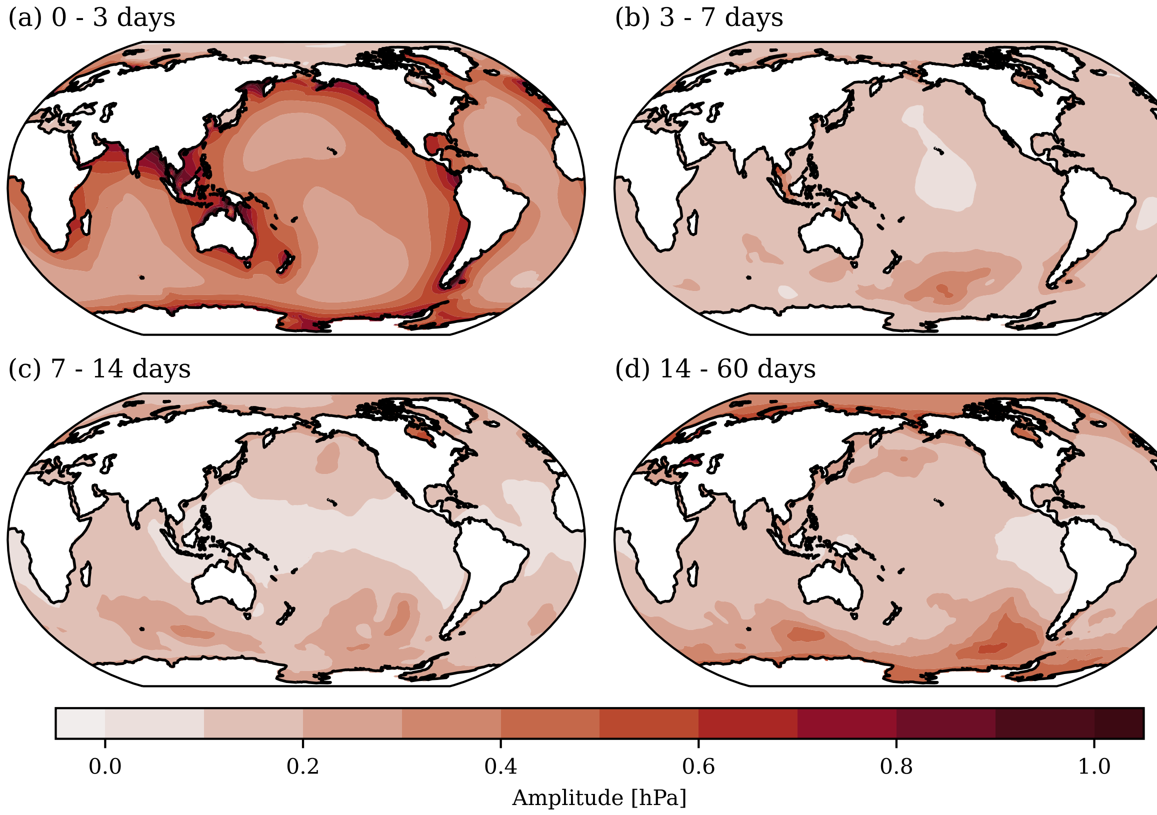

Figure 3.4: Standard deviation of differences in OBA for SAL-SPOBP and noSAL model runs. The results are separated into four frequency bands using a series of Butterworth filters: 0 - 3 days (a), 3 - 7 days (b), 7 - 14 days (c), 14 - 60 days (d).

frequency band (Fig. 3.4 a) signals of up to 1 hPa are observed which is the strongest relative impact of SAL for all frequency bands considered when compared to the background variability depicted in fig. 3.3. These signals are mainly located in shelf / coastal regions and coincide with regions of large OBP variability. For the intermediate frequency bands of 3 - 7 days and 7 - 14 days (Fig. 3.4 b & c), the observed signals are reduced substantially and are well below 0.5 hPa. A somewhat stronger SAL influence is again observed for longer frequencies (Fig. 3.4 d) even though the background variability is stronger here as well. While significant signals of up to 1 hPa are observed in certain shelf areas such as the Gulf of Thailand, signals of up to, and locally even exceeding, 1 hPa are now found in large areas of the Southern Ocean. Mainly, the Kerguelen Plateau and the Bellingshausen Sea as well as east of the Drake Passage. These regions, again, correspond to areas in the region of the Antarctic Circumpolar Current (ACC) that are typically associated with large OBP variability.

We also study the influence of the inclusion of surface pressure anomalies in the SAL potential by comparing the results from the SAL-SPOBP and SAL-OBP model runs in

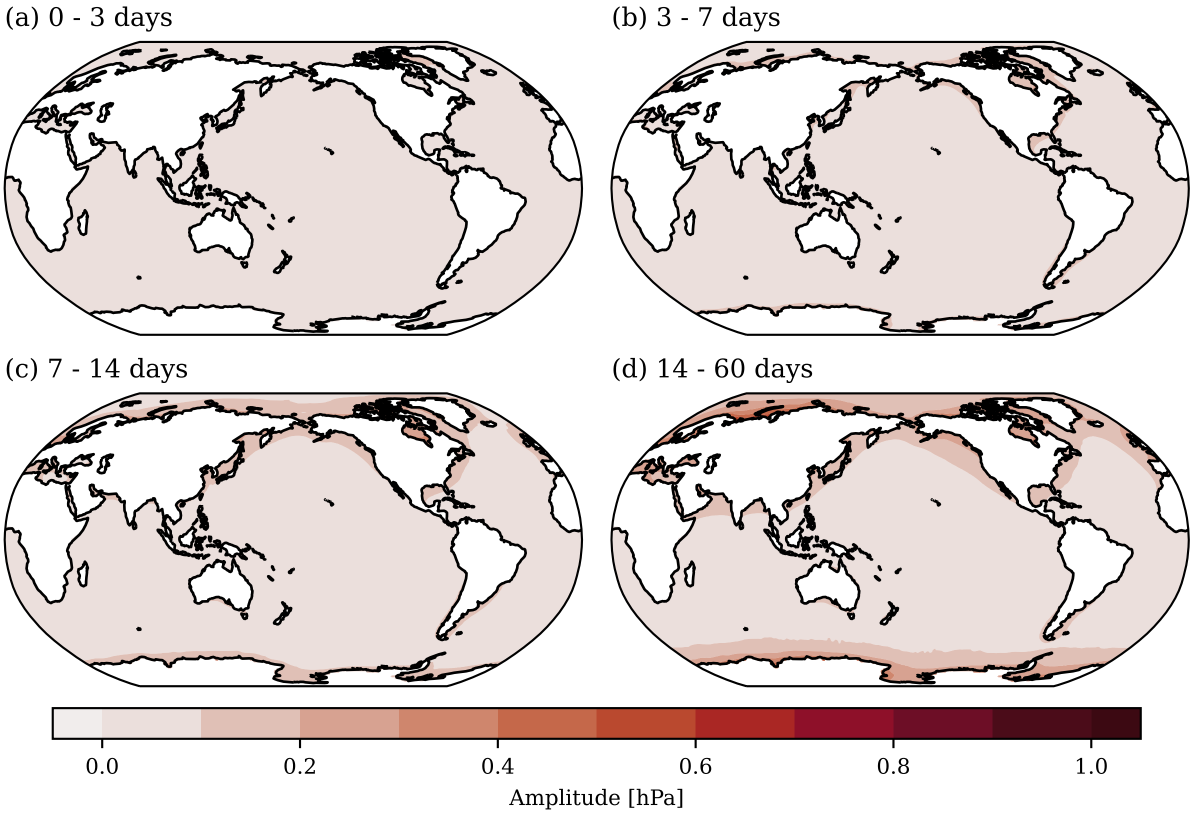

Figure 3.5: Standard deviation of differences in OBA for SAL-SPOBP and SAL-OBP model runs. The results are separated into four frequency bands using a series of Butterworth filters: 0 - 3 days (a), 3 - 7 days (b), 7 - 14 days (c), 14 - 60 days (d).

Fig. 3.5. As the two SAL potential terms do not differ over the open ocean, differences are to be expected mainly in coastal regions. Indeed, Fig. 3.5 (a) shows almost no signal for the high frequency band, suggesting that large scale surface pressure variability over the continents that attracts ocean water masses is not changing rapidly enough to have a notable impact on ocean dynamics. The influence of the surface pressure anomalies increases for longer frequencies and is largest for the low frequency band (Fig. 3.5 d). Here the difference reaches up to 0.5 hPa very close to the coast, while for the open ocean the signal does not exceed 0.1 hPa. We therefore conclude that continental surface pressure forcing has a rather minor impact on ocean dynamics, but can nevertheless be rather easily incorporated into an OGCM.

Fig. 3.6 compares the SAL-OBP and the β-OBP model runs and therefore the difference between the full SAL potential and the scalar approximation. For the high-frequency band, the differences are very localised in shelf areas and locally reach values over 1 hPa. For the intermediate frequency bands the signals are significantly reduced. The most prominent differences are observed for the low frequency band. Here, values of up to, and

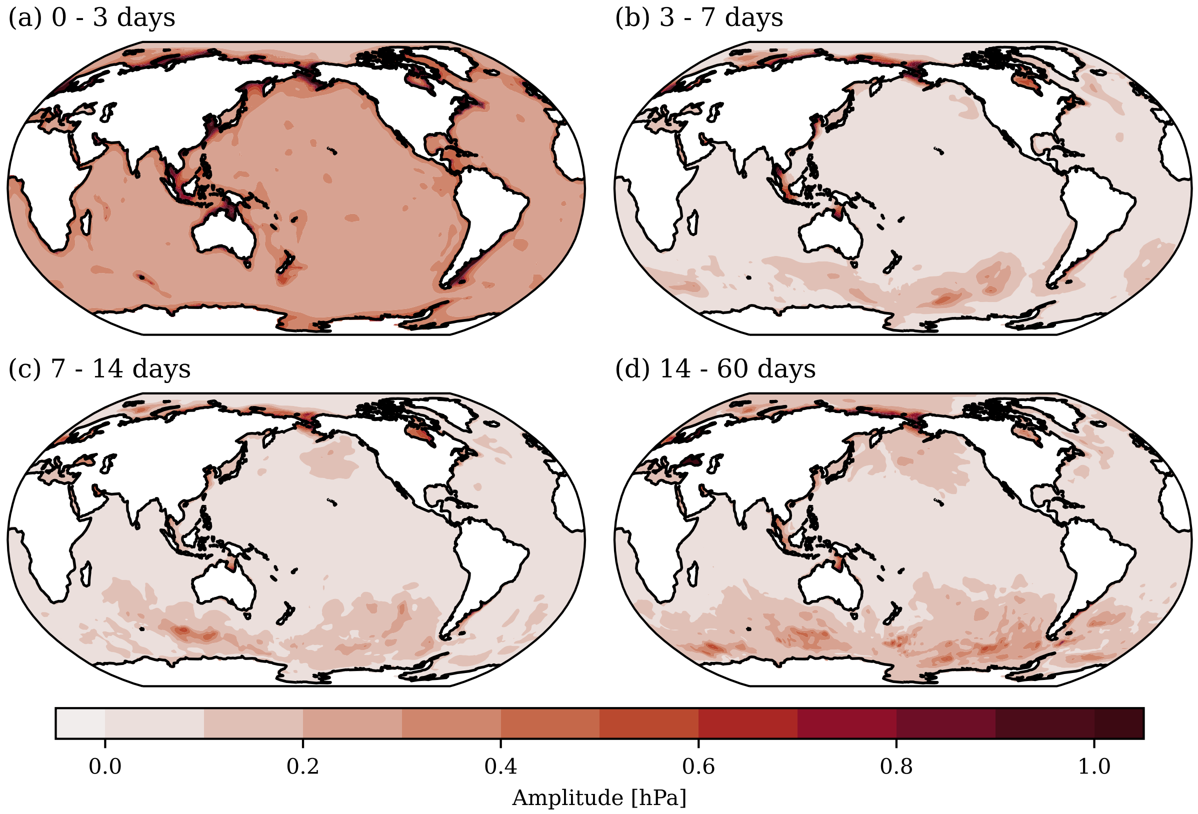

Figure 3.6: Standard deviation of differences in OBA for SAL-OBP and β-OBP model runs. The results are separated into four frequency bands using a series of Butterworth filters: 0 - 3 days (a), 3 - 7 days (b), 7 - 14 days (c), 14 - 60 days (d).

locally exceeding, 2 hPa are reached in parts of the ACC region. These differences are not particularly localised to specific areas but cover most of the ACC region. We rate those differences as substantial, and conclude that it would be advisable to drop the scalar approximation also for the simulation of SAL feedback on the ocean circulation, much in the same way as for the ocean tidal dynamics.

We also compare the influence of the scalar approximation to not including any SAL contribution whatsoever in Fig. 3.7. For the high frequency band differences in coastal areas of more than 1 hPa are found in coastal areas, while for the open ocean values reach up to 0.5 hPa. For this frequency band results are thus comparable to the results shown for the full SAL contribution in Fig. 3.4 (a). Also for the intermediate frequencies (Figs. 3.7 c & d) results are similar to the full SAL contribution. The largest signals are also here found for the low frequency band in the region of the ACC where locally values exceed 2 hPa. Omitting SAL completely would therefore compromise the simulation of the high-frequency wind-driven ocean circulation, so that the incorporation of β-SAL is generally encouraged since it does not impose an additional numerical cost. For precise

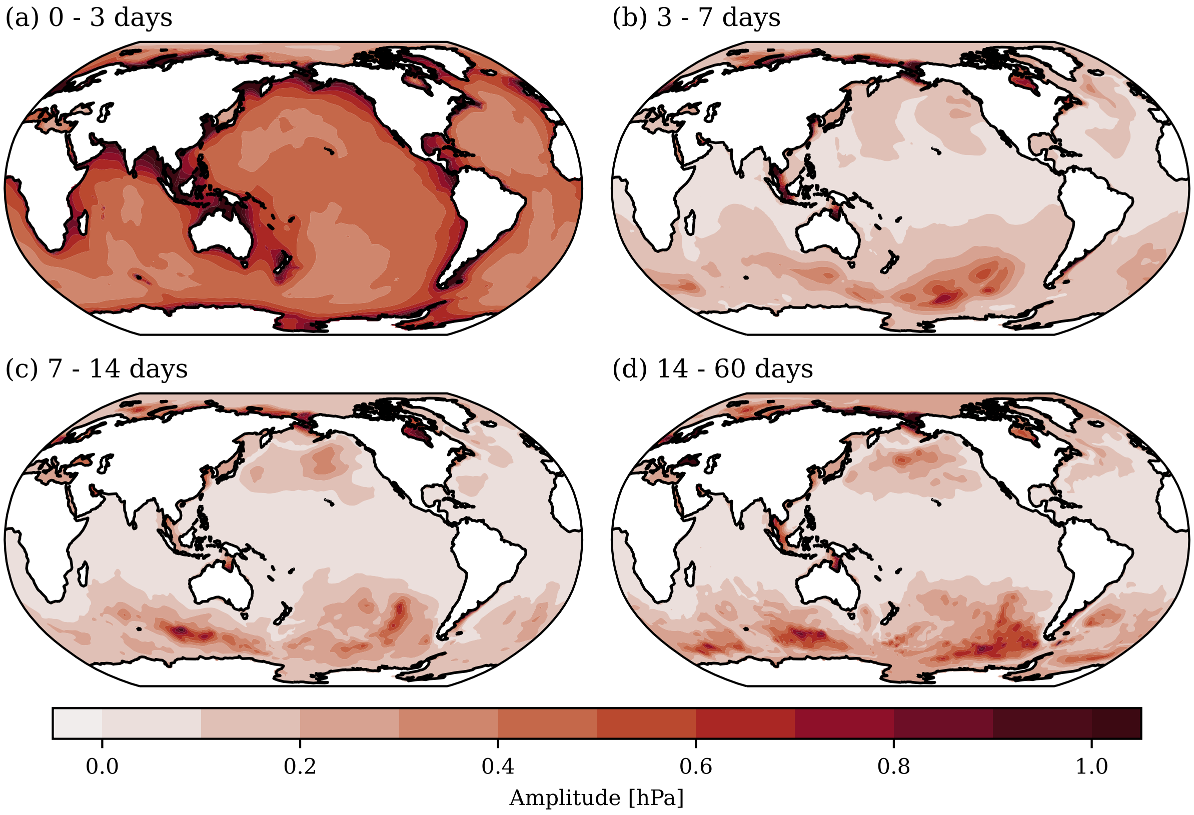

Figure 3.7: Standard deviation of differences in OBA for β-obp and noSAL model runs. The results are separated into four frequency bands using a series of Butterworth filters: 0 - 3 days (a), 3 - 7 days (b), 7 - 14 days (c), 14 - 60 days (d).

simulations focusing on the transient wind-driven dynamics, as, e.g., important for non-tidal ocean de-aliasing (see Dobslaw et al. (2016b)), the full SAL feedback should always be implemented.

3.3.3 Impact of the mean field

All implementations the SAL effects discussed so far are based on pressure anomalies with respect to a long term mean. The choice of the reference field in the computation of the anomalies can thus have an influence on the SAL potential, as errors in the computation or choice of the mean field can result in erroneous horizontal pressure gradients and associated accelerations. To study the influence of the reference field we performed additional model runs with a poorly chosen OBP reference field. Poorly chosen refers here to an OBP mean field that is based on only a single month that is outside of the simulation period.

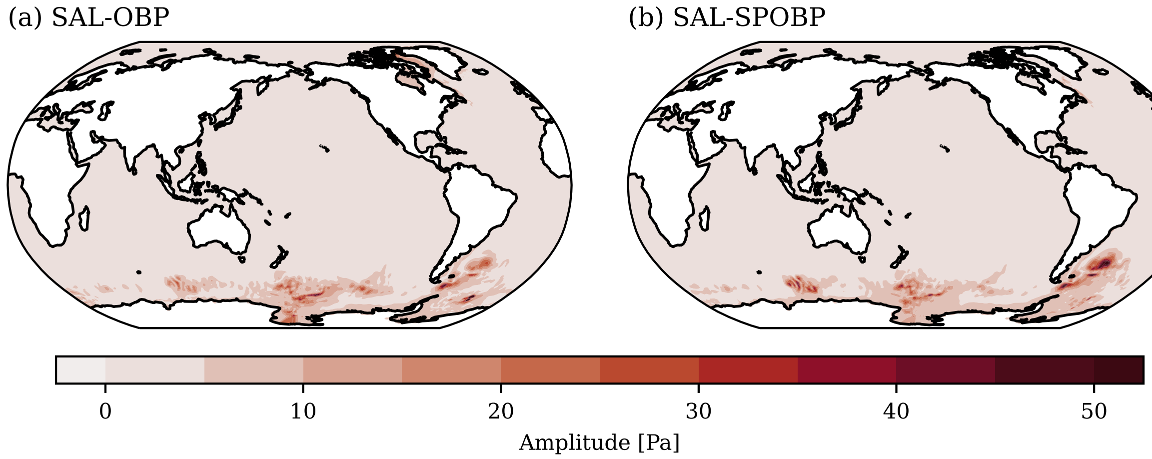

Figure 3.8: Standard deviation of differences in OBA comparing the normal SAL model run with a SAL model run that uses a poorly chosen OBP reference field in the SAL computation. (a) shows the results for the SAL-OBP model run, while (b) shows the results for the SAL-SPOBP model run.

Fig. 3.8 (a) shows the standard deviation differences of OBP between the normal SAL-OBP model run and a SAL-OBP model run with a poorly chosen mean OBP reference field. The results show that the influence of the mean field is mostly limited to the regions of high variability in the Southern Ocean. On larger spatial scales the influence reaches about 20 Pa while locally effects of over 50 Pa are found. The effect on other regions such as the coasts is negligible. From the analysis in different frequency bands it is clear that the coastal influence is mostly found in the high frequency band ($\leq$ 3 days). We thus advise to always use a representative long-term mean field, but conclude that minor errors in the mean field will not induce erroneous feedbacks to the ocean dynamics.

Additionally, we study the influence of the reference OBP field including the surface pressure over the continents. Similar to before, the poorly chosen reference field consists of a mean field over one month that is not included in the simulation period only including the contribution of the surface pressure over land. Fig. 3.8 (b) shows the comparison to the SAL-SPOBP model run. The results when including the surface pressure anomalies are very similar to Fig. 3.8 (a) both in spatial distribution as well as magnitude, indicating that a poorly chosen surface pressure reference field has a much smaller impact compared to the OBP reference field.

3.3.4 Impact on overturning circulation

As the implementation of the effects of SAL are based on OBA, it is expected that the impact of SAL on ocean dynamics vanishes for sufficiently long time periods. In this section we want to show that the influence does indeed vanish and that there is no influence on the long term general circulation. We do this within MPIOM by comparing two long term simulations which are both performed for a period of 30 years, one of which implements the full feedback from SAL while the other has no SAL enabled.

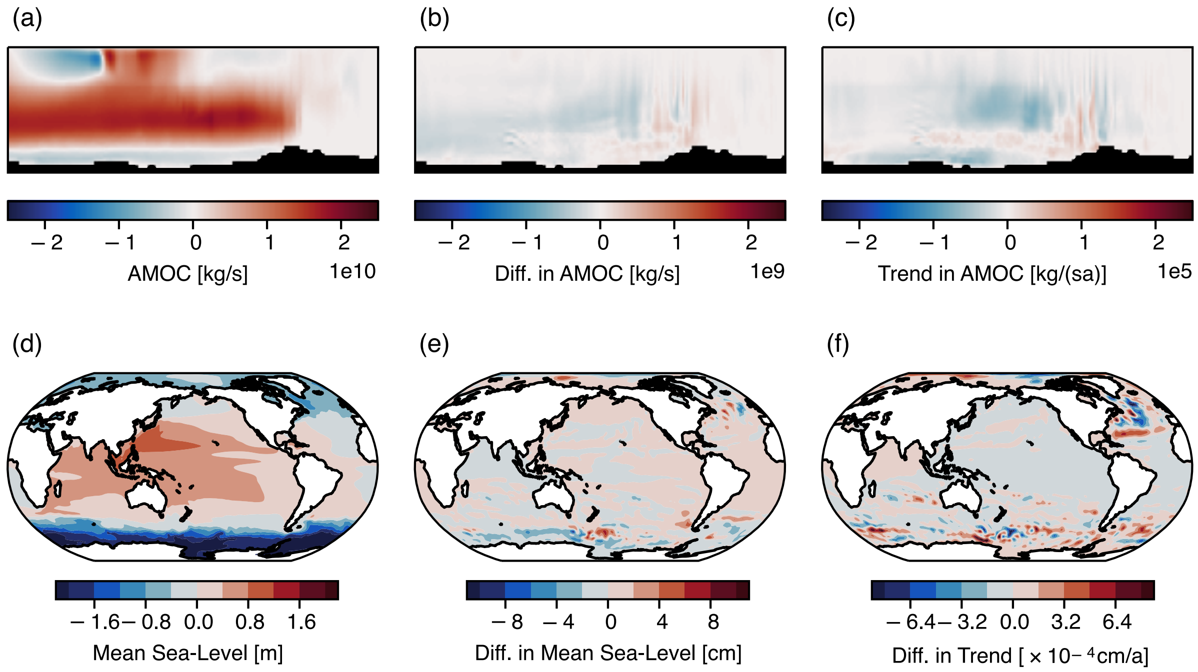

Figure 3.9: Influence of SAL on the long-term general circulation. A long-term mean of the Atlantic meridional overturning circulation (AMOC) stream function is shown in (a), while the mean difference between full SAL and no SAL feedback is shown in (b). The corresponding long-term linear trend is shown in (c). (d)–(f) show the same fields (mean, influence of SAL and trend) but for the sea-surface height.

In Fig. 3.9 we show the influence of SAL on the Atlantic meridional overturning circulation (AMOC) stream function on the left and the sea-surface height on the right. (a) and (d) show the 30 year mean in the AMOC stream function and sea-surface height without any SAL influence. The difference of the long term mean between full SAL and no SAL feedback is shown in (b) and (e), respectively. In (f) and (g) we show the difference in the linear trend for the two simulations.

Comparing the difference between SAL and noSAL model runs to the long term mean, Fig. 3.9 shows that the influence of SAL is on the order of 1% although for most of the grid points even well below that. The largest differences naturally occur in regions where the mean values themselves are largest. Looking at the long term linear trends, the values are on the order of 0.001% per year. In general, the influence of SAL does, as expected, vanish for periods which are sufficiently long.

As a consequence, we note that while we recommend the implementation of SAL for applications where the goal is an accurate representation of the high frequency variability in the ocean, the recommendation does not extend to applications where low frequency effects are the main interest.

3.4 Summary and conclusions

The feedback of self-attraction and loading (SAL) on ocean dynamics is a process that induces additional barotropic pressure gradient forces acting on the sea water. It has therefore consequences for both tidal dynamics and also the non-tidal barotropic circulation. The impact of SAL is strongest on the sub-daily time-scales and vanishes at longer periods, where a quasi-instantaneous adaptation of the sea water to the time-variable external gravity field of the Earth can be safely assumed. SAL is therefore important for the numerical simulations of the rapid (and barotropic) ocean mass variability only.

We have here implemented the SAL feedback into two very different numerical codes employing the shallow-water equations (the TiME global ocean tide model) and the primitive equations (the MPIOM general ocean circulation model). Numerical experiments with the barotropic tidal model TiME indicate that the implementation of the full, non-local effect of SAL is crucial to enable high accuracy results for partial tides of semi-diurnal, diurnal, and also long-period character. The tidal solutions further show that the importance of a full SAL-implementation is much higher for partial tides with shorter periods, as their character is much more dynamic. Nonetheless, the experiments confirm, that a carefully tuned β-approximation can capture a substantial fraction of the SAL-effect on tides and should be always favoured over completely neglecting the impacts of SAL. The results for M_2 based on the MPIOM OGCM are qualitatively similar, even though the SAL influence is somewhat overestimated by up to 30% in various shelf regions. With those comparisons, we demonstrate that a SAL implementation into an OGCM such as MPIOM is both feasible in terms of numerical costs, and also usable for routine simulations.

Additional model experiments with MPIOM were carried out to quantify the consequences of different options for the SAL implementation on the simulated OBP. SAL has an influence on the variability of up to 1 hPa in coastal areas for short periods below 3 d, while on longer periods an influence of up to 0.5 hPa is mainly confined to individual resonant basins in the Southern Ocean in line with previous results from Vinogradova et al. (2015) and Kuhlmann et al. (2011). In extension to those previous studies, we also include the effects of surface pressure anomalies on land in the computation of the SAL potential which are shown to have an influence of up to 0.5 hPa along the coasts.

Previous studies by Schindelegger et al. (2018, 2021) compared OBP estimates from daily GRACE gravity field time-series with various ocean models. AOD1B RL06 (Dobslaw et al., 2017), which is based on a very comparable MPIOM configurations but does not include the effects of SAL, was shown to not sufficiently capture the OBP variability in the GRACE solutions in regions of the Southern Ocean. Similarly, Bonin and Save (2020) studied how well AOD1B explains altimetric variances compared to GRACE solutions and identified similar regions for improvement in the Southern Ocean. The results presented here indicate that including SAL in the model simulations shows the largest influence on the OBP variability in these regions and is thus expected to have a positive impact on the quality of the AOD1B product and should be considered in a new release.

Since the publication of this study of the impact of SAL on both tidal and non-tidal ocean dynamics under Shihora et al. (2022b), SAL has been introduced into other ocean models as well. Barton et al. (2022) have subsequently implemented the feedback of SAL into the Model for Prediction Across Scales (MPAS-Ocean), the ocean component of the Department of Energy Earth system model. The implementation builds on the approach presented here for MPIOM and makes use of a similar transformation and remapping scheme to calculate the SAL potential. While their study focuses on tidal simulations, especially the M_2 tide, the findings are comparable to the results shown here and indicate that the implementation presented in this study is robust and can be used in a wider array of ocean models that feature e.g. grids of variable resolution. For completeness, we also note that Barton et al. (2022) introduced an additional approximation of the full feedbacks of SAL where the SAL potential is held constant for a chosen number of internal model time-steps before being updated. This approximation thus assumes that the SAL potential does not vary substantially on the order of single time-steps which can lead to a reduction in the computational cost as the transformation procedure is not required at every model time-step. While this was only tested for tidal simulations where the approximation yields satisfactory results, the use of this approximation for non-tidal simulations remains untested and could be worthwhile for a follow-up study. For the use of the ocean simulation in the application of satellite gravimetry de-aliasing, however, computational cost is, at least on this scale, not as imperative compared to the accuracy of the simulation, which is why for the next release of AOD1B we choose to use the full implementation of SAL.

4

Non-tidal background modelling for satellite gravimetry based on operational ECMWF and ERA5 reanalysis data: AOD1B RL07

We now focus on the new release 07 of AOD1B. As mentioned in Sect. 2.3, background models form a vital part of the processing chain of satellite gravimetry. AOD1B in particular supplies the a-priori information on non-tidal high-frequency mass variations that contribute to temporal aliasing in the gravity data but also aids in the reduction of spatial leakage effects due to the upward continuation of gravity signals to satellite height and is used for the vertical signal separation in the final application of the time-variable gravity data. The development and inclusion of the feedbacks from SAL as presented in the previous section provide a significant update to the accuracy of the oceanic simulations. However, advances in atmospheric reanalyses and updates to the processing chain can also have a significant impact on the applicability of AOD1B. The new release of AOD1B thus combines the latest available atmospheric reanalysis data, an updated ocean model configuration which also incudes SAL as well as an updated processing chain to arrive at a better representation of the non-tidal high-frequency mass variations in atmosphere and ocean.

In the following, we introduce three experimental datasets (v72, v73 and v74) in preparation of the next RL07 of AOD1B. In Sect. 4.1 we provide details on the datasets in terms of the atmospheric surface pressure, upper air contributions, simulated OBP and transformation into Stokes coefficients. Subsequently, we assess whether ECMWF model changes have an impact on the temporal consistency of the data in Sect. 4.2, and address the impact of possibly higher temporal resolution in Sect. 4.4. The datasets are then compared to the current release RL06 in terms of GRACE-FO K-band range-acceleration pre-fit residuals (Sect. 4.5), line-of-sight gravity differences as measured by the GRACE-FO LRI (Sect. 4.6), and band-pass filtered altimetry data (Sect. 4.7), before we conclude with a final assessment and summary in Sect. 4.8.

4.1 Characteristics of AOD1B RL07

AOD1B RL07 will consist of an atmospheric component based on ECMWF operational and reanalysis data, and an oceanic component based on unconstrained simulations with the Max-Planck-Institute for Meteorology Ocean Model (MPIOM) which is consistently forced with the fields from the corresponding atmospheric model. All three experimental datasets presented here were calculated for the year 2019. Two solutions are based on atmospheric data from ECMWF's ERA5 reanalysis (Hersbach et al., 2020) and given either at hourly (v72) or 3-hourly (v73) time-steps. The dataset v74 is based on ECMWF's operational numerical weather prediction (NWP) model and is given at 3-hourly time-steps. For each experiment, the atmospheric dataset is also used as forcing of the corresponding oceanic simulation by making use of the hourly temporal sampling where available.

4.1.1 Atmospheric surface pressure

Air pressure variations at the surface largely dominate the high-frequency gravity variations induced by atmospheric processes above the continents. Surface pressure is generally decreasing with height, and its representation in models thus critically depends on the height of the surface orography, which varies substantially between individual model configurations. To ensure consistency of the surface pressure time-series, we reduce all datasets to a common reference orography (Dobslaw, 2016) in the same way as for AOD1B RL06.

As AOD1B aims to only describe non-tidal mass variability signals, high-frequency tidal signatures must be estimated and removed from the dataset. Atmospheric tides are primarily induced through the absorption of infrared and ultraviolet radiation in the middle atmosphere as well as periodic deformations of the Earth's crust and sea surface (Dieminger et al., 1996). These signals are removed from the atmospheric data through a harmonic analysis. We consider in total 16 tidal constituents in the least-squares adjustment as given in Tab. 4.1, based on the years 2007 to 2014. The choice of frequencies is based on several criteria such as (i) a minimal amplitude of 10 Pa locally, and (ii) a certain spatial coherence of the waves with similar phases over distances of several hundred km. In contrast to AOD1B RL06, the harmonic analysis newly includes the $\pi 1$, $\psi 1$, K2, S4, S5 and S6 constituents while not considering N2 and L2, which turned out to be negligible in the most recent atmospheric reanalysis ERA5.

Table 4.1: Partial tidal waves reduced from AOD1B RL07 and the associated astronomical arguments as a function of the mean solar time at Greenwich t, the mean longitude of the Moon s, the mean longitude of the Sun h, and the longitude of the Sun's mean perigee p_s. The mean solar time τ is given by $\tau = t - s + h$.

Darwin Name	Frequency [$^\circ$h^{-1}]	Astronomical Argument
$\pi 1$	14.91786609	$t - 2h + p_s - 90^\circ$
P1	14.95893277	$t - h - 90^\circ$
S1	15.00000141	$t + p_s + 90^\circ$
K1	15.04107005	$t + h + 90^\circ$
$\psi 1$	15.08213673	$t + 2h + p_s + 90^\circ$
M2	28.98410705	$2t - 2s + 2h$
T2	29.95893614	$2t - h + p_s$
S2	30.00000282	$2t - 90^\circ$
R2	30.04106950	$2t + h - p_s + 90^\circ$
K2	30.08214010	$2t + 2h$
T3	44.95893559	$3t - h$
S3	45.00000423	$3t + 90^\circ$
R3	45.04107287	$3t + h$
S4	60.00000564	$4t$
S5	75.00000705	$5t$
S6	90.00000846	$6t$

Initially, we focus on the comparison of surface pressure from ERA5 and the ECWMF operational data both given at 3-hourly intervals after mapping to a common reference orography and subtraction of atmospheric tides (Fig. 4.1a). Standard deviations of differences calculated for the year 2019 are well below 80 Pa globally, while most of the signal is found along the ACC where in-situ data coverage is sparse and storm events are imminent. We note that those differences are small with respect to differences with other state-of-the-art global atmospheric reanalyses, and can be related to the common code base of ECMWF's Integrated Forecast System (IFS) that is being used for both the ERA5 reanalysis and the operational NWP model. It is thus acceptable to concatenate ERA5 and the operational data at some point in time to make use of both the long-term consistency of the reanalysis and the low-latency availability of the operational data.

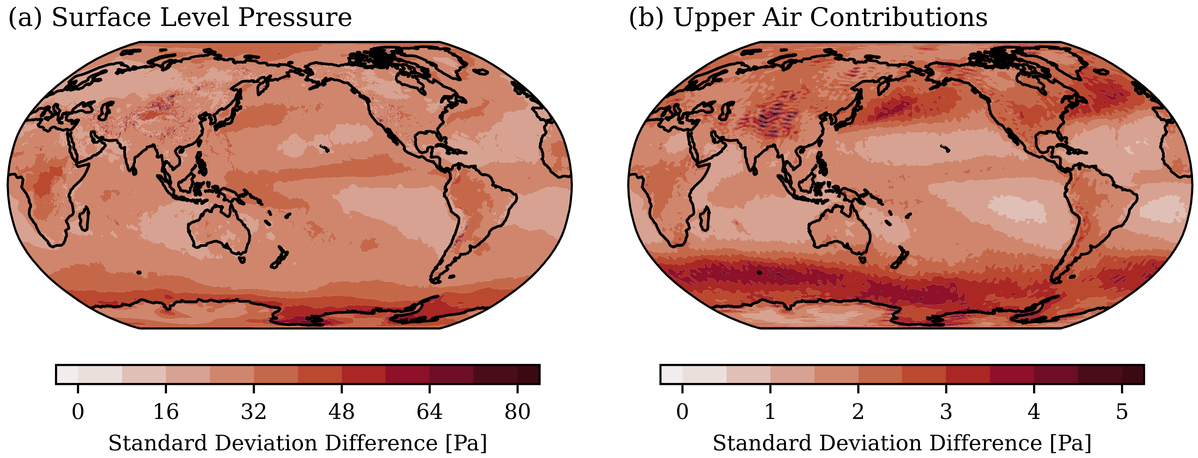

Figure 4.1: Standard deviation of differences between ERA5 and ECMWF operational surface level pressure (a) and upper air contributions (b). ERA5 data is sub-sampled to 3 hourly epochs to ensure equal temporal sampling of both datasets.

4.1.2 Upper-air contributions

In addition to surface pressure, there is also a small contribution of upper-air density anomalies to the gravity field that should not be ignored for precise instruments as employed by GRACE and GRACE-FO (Swenson and Wahr, 2002).

The computation of the upper air density effects is based on a vertical integration of the atmospheric densities calculated at the original hybrid pressure-sigma (model) levels that are smoothly following the surface orography. Geopotential values at the 137 model levels are computed employing 3D temperature and specific humidity fields. After a transformation into mass increments, the gravitational effect is integrated vertically by summing up the contributions of each model level (Dobslaw et al., 2016a). Subsequently, the gravitational effect of the surface pressure is subtracted to only retain the effects of the upper-air masses. Note that no reference orography is employed here but all calculations refer to the original model orography and the associated vertical discretization. We refer the interested reader to Dobslaw et al. (2016a) for further details.

Upper-air anomalies were calculated from 3-hourly ERA5 and operational ECMWF data for the whole year 2019. To facilitate comparison, gravity potential differences are synthesized back into the spatial domain and are displayed in terms of corresponding surface pressure anomalies. The standard deviations of the differences are displayed in Fig. 4.1b. The signals are one order of magnitude smaller than the remaining differences of surface anomalies and amount to 5 Pa only. The largest signals are found in regions of the mid-latitude storm tracks which roughly corresponds to the band of the ACC in the southern hemisphere.

4.1.3 Ocean bottom pressure

To complement the atmospheric mass variability, AOD1B uses simulations with the MPIOM OGCM. Here, we make use of a similar configuration as in Sect. 3, using the TP10L40 configuration which uses a 1° tri-polar Arakawa-C grid with 40 vertical layers and nominal internal model time-step of 20 minutes. The model contains a dedicated sea-ice module. As indicated in the previous section, the full feedback of SAL has been implemented (Shihora et al., 2022b). Additionally, the spatial domain has been extended to also include cavities underneath the Antarctic shelf-ice which were not part of the simulation domain in AOD1B RL06.

Model experiments were initialized from climatologies of observed 3D ocean temperature and salinity distributions (Levitus et al., 2005), followed by a 2000 year long spin-up run under cyclic atmospheric forcing with daily sampling (Röske, 2005).

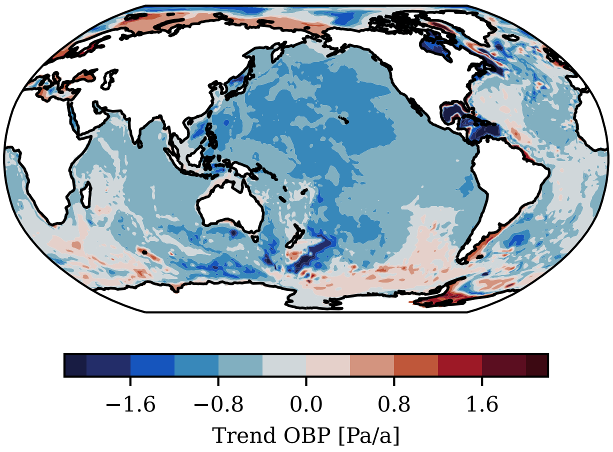

Figure 4.2: Linear trend in OBP over the last 50 years of the 2000 year long spin-up simulation.

Residual linear trends in OBP during the last 50 years of the spin-up simulation are well below 2 Pa/a on regional scales and below 4 Pa/a for all individual grid points (Fig. 4.2). The largest trends are found in (semi-) enclosed seas, which typically take longer to reach a state of equilibrium due the limited exchange of water masses with the open ocean. We note, however, that further spin-up would hardly reduce those residual trends significantly, since these signals are, in fact, not linear, but overlaid by substantial decadal-to-centennial ocean variability. In view of the small magnitude of the remaining drift, we rate this state as fully acceptable starting point of all subsequent experiments with NWP forcing data.

By starting from the same initial state, a transient simulation with hourly ERA5 forcing data is integrated over the years 1980 until 2019. A second simulation with 3-

hourly ECMWF operational forcing extending also until the end of 2019 is initiated in January 2018 with initial conditions taken from the ERA5 run. Note that the atmospheric forcing fields have been modified to accommodate the shielding effect of the Antarctic shelf-ice by setting temperatures to -4° (Bernales et al., 2017), and wind stress as well as atmospheric freshwater fluxes to zero. Surface pressure forcing remains unaffected since it is propagated through the ice body. We also allow for the far-field attraction effects of atmospheric pressure variability on ocean dynamics as detailed in Sect. 3.

While both oceanic simulations do not explicitly include attraction from the luni-solar gravitational potential, tidal signals are still induced in the ocean simulation through periodic variations in atmospheric surface pressure and wind stress. The required subtraction of tidal signals is done using the same procedure as described above for the atmosphere. Again, 16 tidal constituents are considered and the estimation is performed for a single year 2019 only. We note that this estimation is performed independently for both ocean model experiments.

Additionally, we account for artificial fluctuations in the total ocean mass induced by the Boussinesq approximation included in MPIOM's prognostic equations by subtracting the mean OBP signal averaged over the entire ocean domain (Greatbatch, 1994).

In the following, hourly data from the ERA5 experiment is labelled as v72. Data from the same experiment that is sub-sampled to 3 hours by selecting every third time-step will be referred to as v73. The 3-hourly data from the simulation with operational ECMWF forcing is called v74 in the reminder of this section.

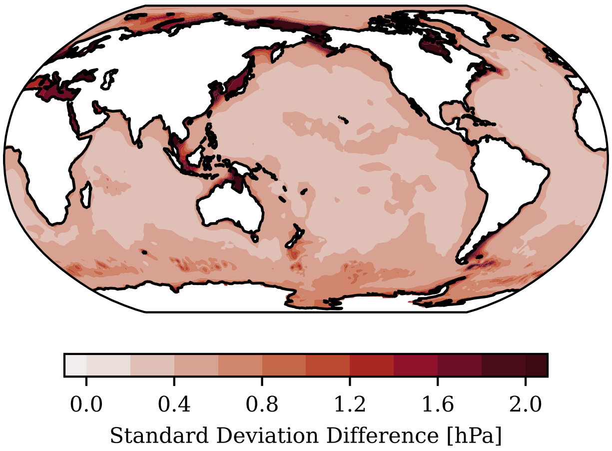

Figure 4.3: Standard deviation of difference in OBP between v73 and v74.

As a first step, we are assessing the impact of different atmospheric forcing sources on the simulated OBP by looking at the standard deviation of the differences between v73 and v74 each after subtracting the estimated tidal signals (Fig. 4.3). In most of the open ocean, the differences are well below 0.5 hPa, with a spatial average over the entire ocean domain of 0.55 hPa. A slightly increased difference in variability is found in the Southern Ocean in the region of the ACC which is the region with the largest variability driven by the atmospheric forcing. We find also strong signals of up to 2 hPa in several coastal and shelf regions. In these regions, most of the variability is in the sub-daily frequency band and thus differences in the spatial and temporal resolution of the atmospheric forcing have a correspondingly stronger impact.

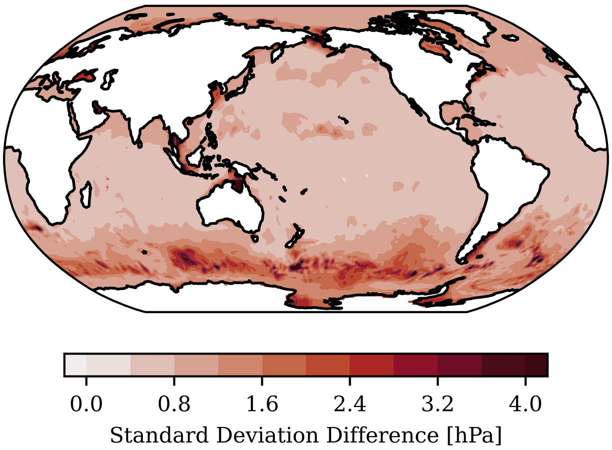

Figure 4.4: Standard deviation of difference in OBP between v74 and AOD1B RL06.

Additionally, we also assess the differences between v74 and the oceanic simulation of AOD1B RL06, which is also forced with ECMWF's operational data in the year 2019 (Fig. 4.4). The simulated OBP is very similar in the tropical and subtropical open ocean with a global average of the standard deviation difference of just under 1 hPa. Notable discrepancies are found in coastal regions and enclosed seas such as the Gulf of Carpentaria, where the effects of SAL have a significant impact as also revealed in a dedicated GRACE-FO LRI along-track analysis (Ghobadi-Far et al., 2022). The most significant differences, however, are found in the Southern Ocean in the region of the ACC. Here, model changes in MPIOM between v74 and RL06 such as the feedback from SAL as well as the inclusion of cavities under the Antarctic ice-shelves have a rather strong effect (Shihora et al., 2022b; Schindelegger et al., 2021).

4.1.4 Transformation into Stokes coefficients

Time-variable background models are traditionally provided in terms of Stokes coefficients. As for previous releases, RL07 will be made available up to spherical harmonic d/o 180. Four individual sets of coefficients (i.e., ATM, OCN, GLO and OBA) will be provided at each time-step that contain individual signal components of the coupled atmosphere-ocean system.

The ATM coefficients contain the contribution of atmospheric surface pressure over the continents, the static contribution of atmospheric surface pressure to OBP elsewhere, and the contribution of upper-air density anomalies over both the continents and ocean. OCN contains the contribution of the dynamic ocean to OBP while excluding the static contribution of the atmosphere. The GLO coefficients form the combination of the ATM and OCN coefficients and are usually applied in precise orbit determination. Finally, OBA are set to zero over the continents and contain the simulated OBP including the surface pressure contribution over the oceans. OBA coefficients deviate from the GLO coefficients by disregarding the comparatively minor contribution of the upper air density anomalies. A detailed description of the data-products including file formats is given in Dobslaw et al. (2016a).

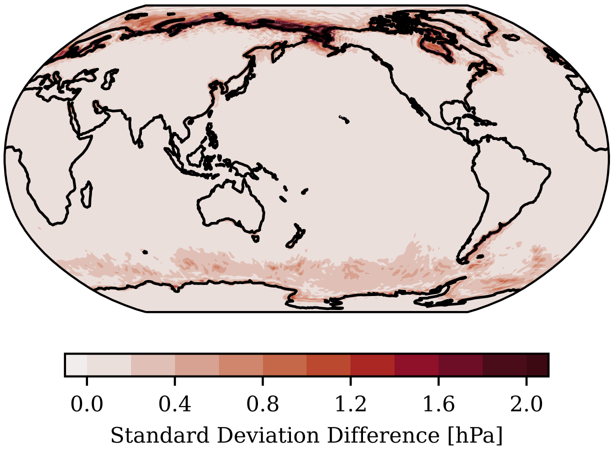

Figure 4.5: Influence of the change to an ellipsoidal reference surface. Differences in the OCN coefficients of v74 when using either a spherical or ellipsoidal reference surface are transformed back to a grid and shown in terms of the standard deviation.

In contrast to previous AOD1B datasets, we here also make use of an ellipsoidal reference surface during the transformation of the OBP fields into Stokes coefficients (Dobslaw et al., 2016a) which so far has been used only for the atmospheric components (Petit and

Luzum, 2010; Ghobadi-Far et al., 2019). To demonstrate the potential impact, Stokes coefficients were computed both at a spherical (as in RL06) and an ellipsoidal surface. After back-transformation into the spatial domain, standard deviations of the differences are shown in Fig. 4.5. Signal magnitudes of up to 2 hPa underline the importance of applying a proper reference surface. Please note that most of the OBP variability is also associated with a corresponding sea-level change induced by changes in wind forcing. It is therefore reasonable to assume that most of the mass change happens close to mean sea-level (which is well approximated by an ellipsoidal surface) and not at the ocean sea floor.

4.2 Impact of ECMWF model changes

It is important to recall that ECMWF operational data is supplied regularly for many years already, and modern improvements to the forecast system are implemented through occasional updates of the Integrated Forecasting System (IFS). Dataset v74, as it is based on the operational data for the year 2019, includes the transition to the IFS cycle 46R1 on June 11th, which implements changes in the data assimilation, observation handling, and physical model changes. We thus assess if, and to what degree, the transition in the IFS affects the dataset v74 as an example of such regular IFS upgrades that typically take place once or twice per year.

We therefore calculate the spatially averaged absolute values of the 3-hourly tendencies, which are computed as differences between consecutive 3 hourly time-steps, for the month of June 2019 around the time of the model change (June 11th). Tendencies are shown for the atmospheric surface pressure (top), simulated OBP (middle) and upper air contributions (bottom). Black curves here represent the ECMWF operational based data, while grey represents the ERA5 based dataset of v73. To recall, the key feature of atmospheric reanalyses is the application of the same model configuration for the whole analysis period. v73 thus serves as a reference that is not affected by any such changes in the IFS. Any prominent offset in a simulated quantity would manifest as a prominent spike in the tendencies.

Fig. 4.6 confirms no significant impact of the IFS model change in 2019 on quantities relevant for satellite gravimetry. The temporal variations of the tendencies are very comparable between v73 and v74 and can be explained by the prevailing weather situation during those days. We note a slightly higher level (20%) of the tendencies from ERA5 for both OBP and the upper air contributions, which is due to a slightly different handling of the wind stress and the different spatial resolutions of both atmospheric models. At

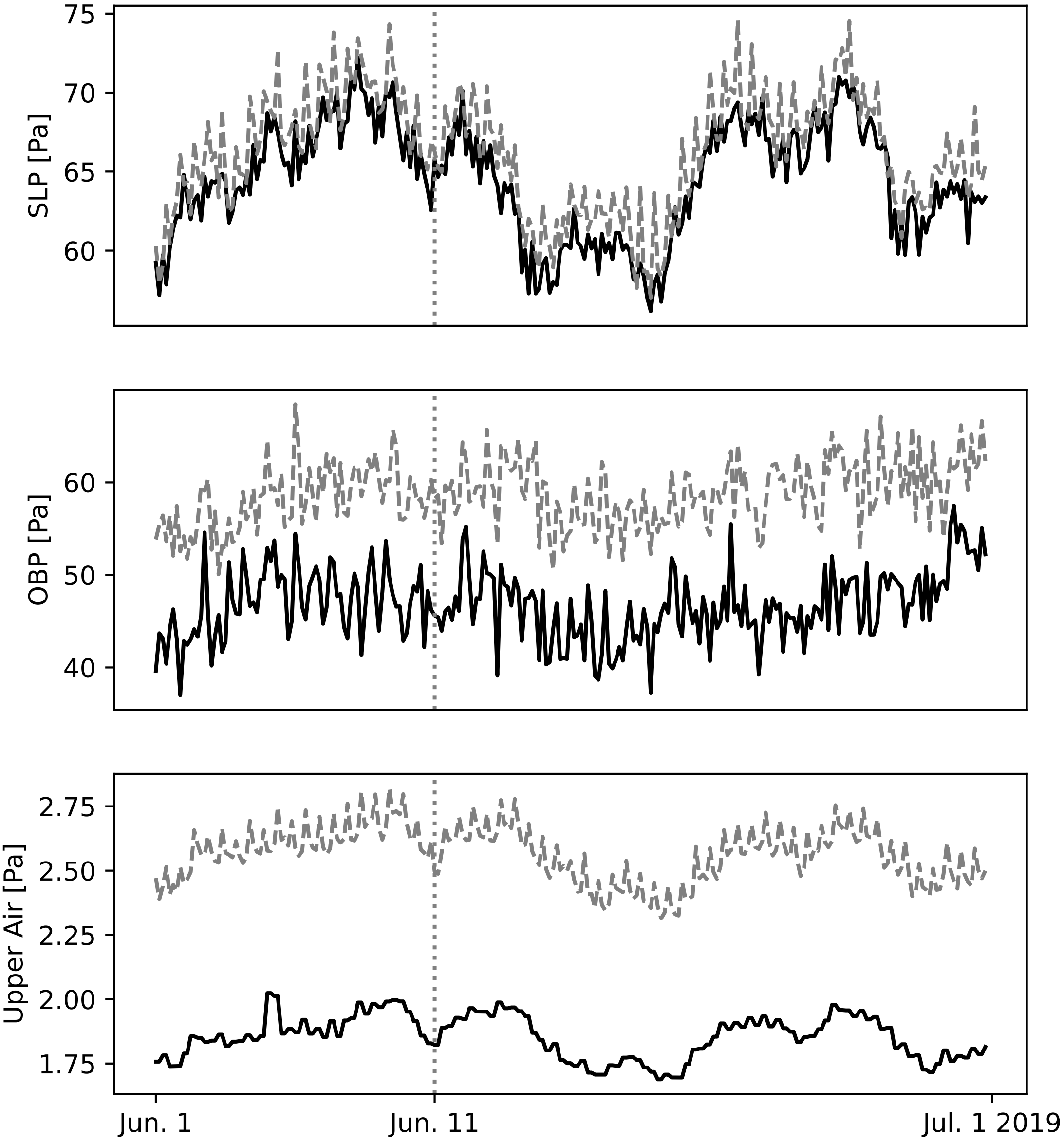

Figure 4.6: Spatially averaged absolute value of 3-hourly tendencies for June 2019 which includes the change to the IFS cycle 46R1 of the ECMWF operational forecasts. Tendencies are given for atmospheric surface level pressure (SLP), simulated ocean bottom pressure (OBP), and upper-air anomalies. Black indicates ECMWF operational based data used in v74, while grey represents ERA5 based data as used in v73.

the date of the IFS transition, no increase in tendencies is found, so that there are thus no indications for any adverse influence of the IFS cycle 46R1 model change on quantities relevant for the calculation of AOD1B.

4.3 Impact of tidal reduction

As noted above, tidal waves are estimated and removed from the non-tidal variability that remains in AOD1B. To assess the impact of this separation, we show the resulting reduction in sub-daily variability for the ERA5 surface pressure, upper-air contributions and OBP (Fig. 4.7) before (left) or after (right) the harmonic analysis.

For the surface pressure, atmospheric tides are very prominent at tropical latitudes, and the variability is reduced drastically at those latitudes, with a global average reduction of 47%. In the regions of mid-latitude storm tracks that are characterized by advecting cyclones, however, almost none of the sub-daily variability is explained by atmospheric tides. The picture is quite different for OBP, where hemispheric waves are excited by the periodic atmospheric forcing leading to the establishment of distinct large-scale amphidromic systems with strong variability in particular along the coasts of major ocean basins. For OBP the reduction in variability is even stronger than for the surface pressure with a global average of 57%. For the upper-air contributions, on the other hand, the impact of atmospheric tides is very minor and can be, in fact, safely neglected in the processing of AOD1B.

We have updated both the procedure as well as the tidal constituents that are estimated and removed from both the atmosphere and ocean components compared to AOD1B RL06. In a dedicated study by Balidakis et al. (2022) we have analysed the atmospheric tidal signals in the ERA5 reanalysis data to determine the relevant tidal constituents. In addition, we have compared the induced tidal signals from the MPIOM simulations with the atmospheric contribution to ocean tides in the dedicated barotropic tidal model TiME (Sulzbach et al., 2021). Validation of the MPIOM and TiME derived tidal signals against tide gauge data and the FES2014 global ocean tide atlas (Lyard et al., 2021) shows that the tidal signals, as simulated with the general circulation model MPIOM, can not match the accuracy of a dedicated tidal model. As a result, in the application of satellite gravimetry de-aliasing, the atmospheric contribution to ocean tides should not be taken from MPIOM but should be derived using a dedicated tidal model instead to achieve the best possible performance.

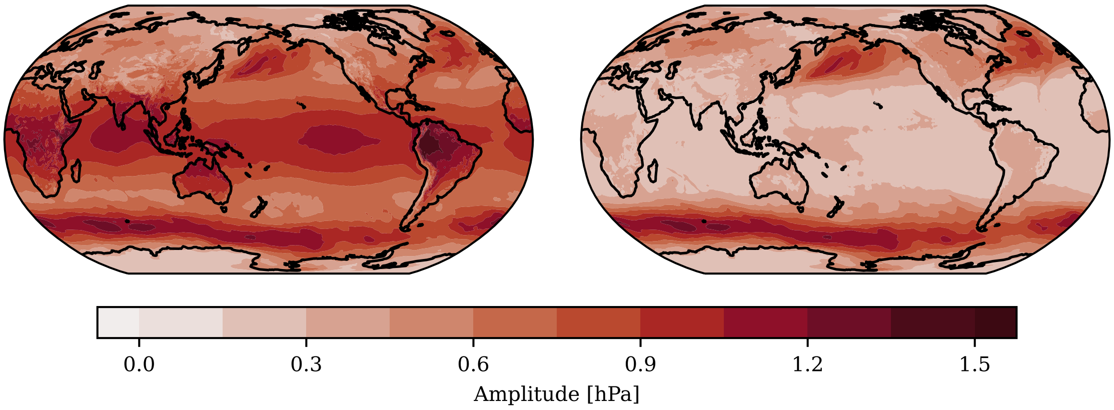
(a) ERA5 SLP (b) ERA5 SLP without tides

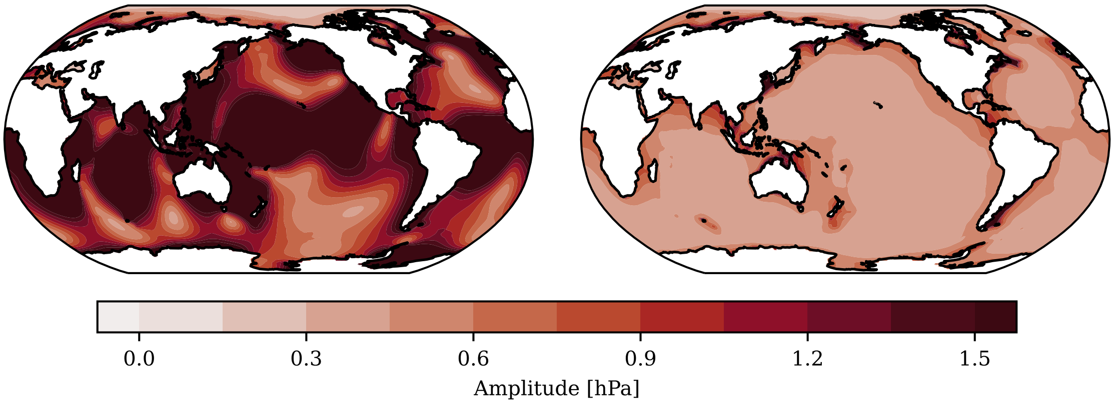
(c) MPIOM OBA (d) MPIOM OBA without tides

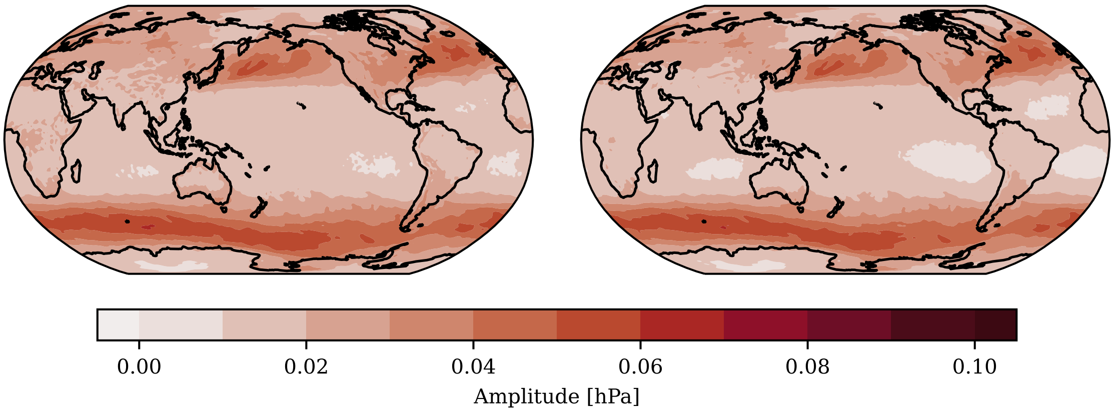
(e) Upper Air (f) Upper Air without tides

Figure 4.7: Sub-daily variability of ERA5 surface pressure (SLP) (a & b), MPIOM ocean bottom pressure (OBP) (c & d) and ERA5 based upper air anomalies (e & f) either including tidal signals (left) or after the removal of tidal signals (right).

4.4 Impact of temporal resolution

RL06 of AOD1B and the datasets v73 and v74 are all given with 3-hourly resolution. Since the ERA5 reanalysis is even available with hourly resolution, it is important to assess the possible gain of such an enhanced temporal resolution. To do so, we sub-sample the hourly v72 data to 3-hourly fields and interpolate back linearly to an hourly sampling in the same way as it would have been done in GRACE precise orbit determination to arrive at background model values for arbitrary epochs in time. Subsequently, the standard deviation of the differences is computed between the original and interpolated data.

Standard deviations of differences for surface pressure, OBP and the upper air contributions show negligible benefits of the hourly temporal resolution particularly after the removal of the tidal signals (Fig. 4.8). We thus conclude that 3-hourly data can easily be interpolated to higher temporal resolutions without greatly compromising the high-frequency variability. The influence of linear interpolation to hourly values only introduces differences of up to 0.5 hPa provided that tidal signals are carefully removed from the underlying dataset. AOD1B RL07 is therefore provided again with a 3-hourly sampling.

4.5 Impact on GRACE-FO K-band pre-fit residuals

We assess now the impact of the new background models on primary sensor data from the GRACE-FO mission. The analysis is based on K-band range-acceleration (KBRA) pre-fit residuals obtained after data screening and precise orbit determination in the GFZ RL06 data processing (Dahle et al., 2019b). The KBRAs are computed by differentiating K-band range-rate residuals and applying a 5th order Butterworth filter with a cut-off frequency of 1/60 Hz. Subsequently, the KBRA residuals are binned into cells with a 3° width before computing standard deviations for each of those grid cells.

Any improvement in the background model data would lead to a better fit with the measured satellite observations, i.e. smaller observation residuals. Consequently, reductions in KBRA residual variability can be interpreted as improvements in the representation of the high-frequency variability in a test dataset. The differences in standard deviation between KBRA residuals for the entire year 2019 are given in Fig. 4.9 for comparisons between AOD1B RL06 and v73 (upper left), RL06 and v74 (upper right) as well as v73 and v74 (bottom).

Based on this assessment of real GRACE-FO data, we note improvements in several semi-enclosed regions as, for example, the Gulf of Carpentaria or the Gulf of Thailand, as well as improvements in the Southern Ocean in the region of the ACC, especially the

(a) ERA5 SLP (b) ERA5 SLP without tides

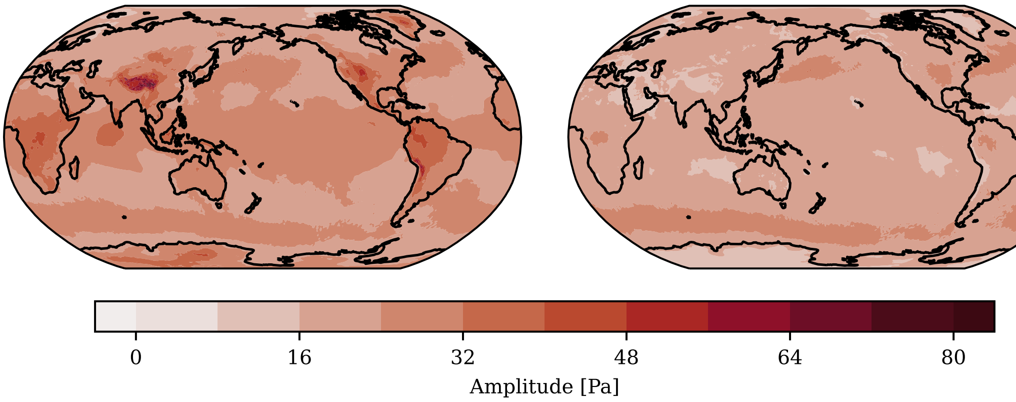

(c) MPIOM OBA (d) MPIOM OBA without tides

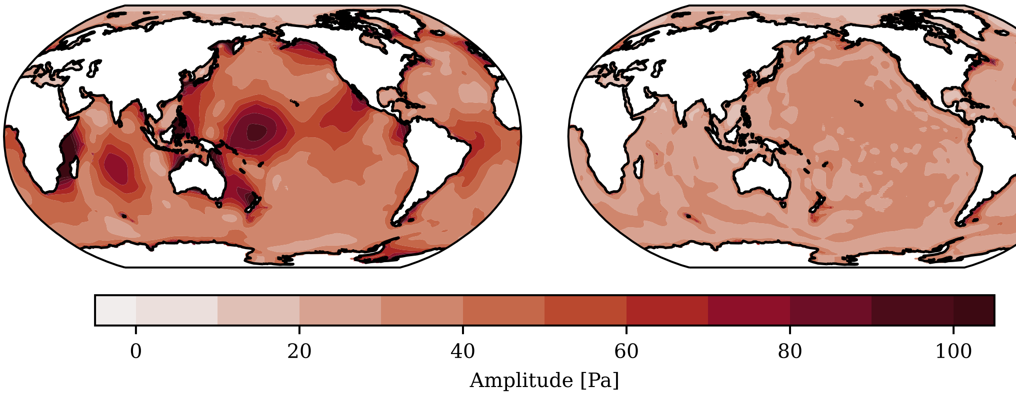

(e) Upper Air (f) Upper Air without tides

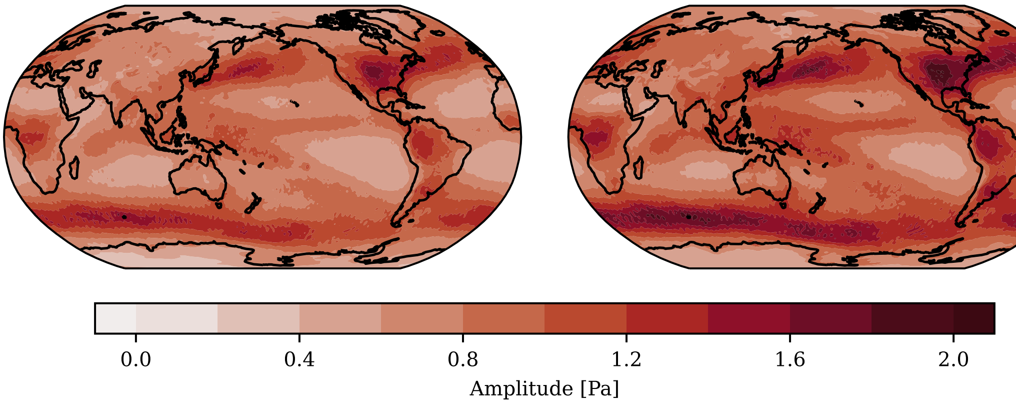

Figure 4.8: Standard deviation of differences between original hourly data and 3-hourly data linearly interpolated to hourly epochs for ERA5 surface pressure (SLP) (a & b), MPIOM ocean bottom pressure (OBP) (c & d) and ERA5 based upper air anomalies (e & f). Figures are given either containing tidal signals (left) or after the subtraction of tidal signals (right).

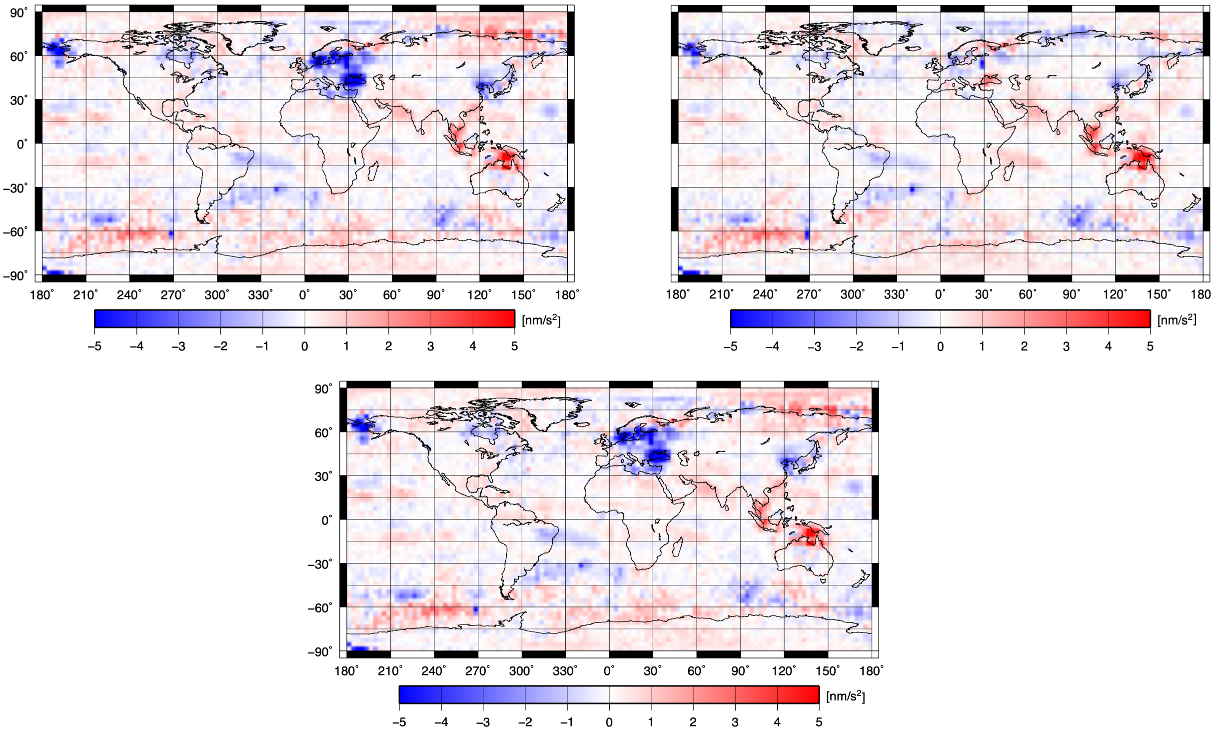

Figure 4.9: Difference of standard deviations of binned K-band range-acceleration pre-fit residuals for the entire year 2019. AOD1B RL06 - v73 is given in the upper left, AOD1B RL06 - v74 is given in the upper right. The lower subfigure shows the difference between v73 and v74. Positive values indicate an improvement, while negative values represent a degradation.

Bellingshausen Basin. Slight degradations are visible for v73 in the region of the Black and Baltic Seas, which are related to a slight overestimation of the variability.

Additionally, we assess the area-weighted median of the KBRA pre-fit residual standard deviation differences between AOD1B RL06 and v74 for several regions in Tab. 4.2. We distinguish between deep and shallow oceanic regions (limit: $H = 1000$m), tropics ($|\phi| = 23.5°$), northern latitudes ($23.5° < \phi < 66°$) and southern latitudes ($-23.5° < \phi < -66°$). The median is computed for all area-weighted grid points in each region requiring a minimal signal of 0.1 nm/s^2. Both on a global scale and the considered areas, v74 outperforms the current RL06 by at least 0.12 nm/s^2.

In summary, v73 and v74 are very comparable and show both regions of improvements compared to AOD1B RL06 that are quite consistent with results for the pair-wise model comparisons presented above.

Table 4.2: Median of differences in KBRA pre-fit residuals between AOD1B RL06 and v74 (Fig. 4.9 upper right) for different regions.

Region	Median of pre-fit differences [nm/s^2]
Global	0.16
Shallow Waters (<1000 m)	0.16
Deep Water, Tropics	0.20
Deep Water, Northern Lat.	0.16
Deep Water, Southern Lat.	0.12

4.6 Impact on GRACE-FO LRI residuals

In addition to the KBR sensor, GRACE-FO is also equipped with an LRI which measures the inter-satellite distance with higher precision (Abich et al., 2019). We use the LRI data in 2019 to study the impact of the new datasets. To that end, we first compute the LRI pre-fit residuals by removing the effect of static gravity and other well-known high-frequency geophysical signals like ocean tides from measured range-rate data. The range-acceleration residuals, obtained by numerical differentiation, are then used to compute the line-of-sight gravity difference (LGD) observations by applying a transfer function (Ghobadi-Far et al., 2020). By removing the slowly-varying time-variable gravity signals using the GRACE-FO Level-2 monthly solutions (Yuan, 2019), we obtain the sub-monthly (or post-fit) LGD LRI observations which partly reflect the high-frequency, non-tidal mass changes in the atmosphere and oceans. Note that, in contrast to KBR dara, the improved accuracy of LRI residuals, which at higher frequencies reaches as much as 1 order of magnitude (Ghobadi-Far et al., 2020), allows for obtaining precise gravitational measurements without applying any low-pass filter.

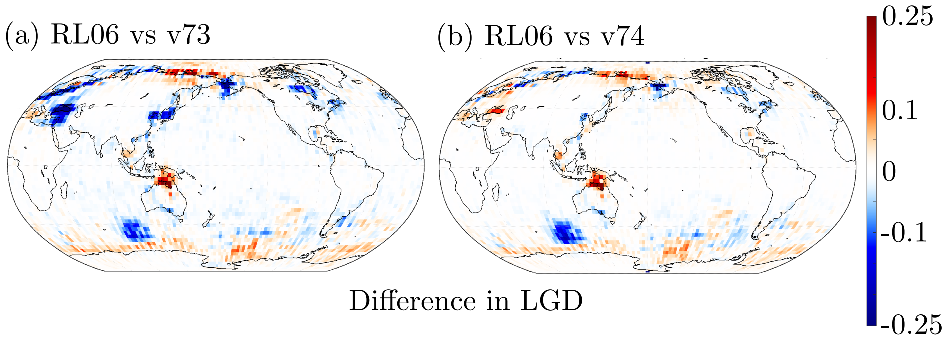

Figure 4.10: Differences in RMS variability of the LRI residuals in nm/s^2 between AOD1B RL06 and v73 (a) or v74 (b) for the year 2019. Positive values indicate an improvement, while negative values represent a degradation.

The sub-monthly (post-fit) LRI residuals in terms of LGD are further reduced by gravitational signals computed from v73, v74 and AOD1B RL06. The difference in RMS

Table 4.3: Median of differences in LRI residuals between AOD1B RL06 and v74 (Fig. 4.10 right) for different regions.

Region	Median difference in RMS variability [nm/s^2]
Global	0.025
Shallow Waters (<1000 m)	0.025
Deep Water, Tropics	0.022
Deep Water, Northern Lat.	0.021
Deep Water, Southern Lat.	-0.020

variability of LRI residuals expressed in nm/s^2 (computed in 3 degree bins) with respect to these models is shown in Fig. 4.10. Regions where the new test-data better matches the GRACE-FO LRI measurements are depicted in red, while areas of degradation are indicated in blue.

The results reveal general improvements in both cases in the Southern Ocean in the band of the ACC as well as the Gulf of Carpentaria and some regions along the Arctic coast. Additionally, v74 shows some improvements in the Mediterranean and Black Sea. There are, however, areas where the test data does not capture the variability as well as RL06 such as a region of the Southern Ocean to the south-west of Australia and the Bering-Sea. v73 also shows a slightly worse performance in some enclosed seas such as the Black and Baltic Seas or the Sea of Japan.

We also compare RL06 and v74 in terms of global and regional median values as done in Sect. 4.5. The results are given in Tab. 4.3 and are computed for the same regions requiring a minimal signal of 0.02 nm/s^2. Considering the generally smaller magnitude of the LRI based values, the results in Tab. 4.3 are in most cases comparable to the ones given in the previous section, indicating a better performance of v74. Only in the deep ocean of the southern latitudes can the new dataset not match the results from RL06 resulting in a negative median of -0.02 nm/s^2. On a global scale, however, v74 still captures the high-frequency variability better than RL06.

In general, the results clearly match the analysis based on KBRA pre-fit residuals, although the picture is more detailed thanks to the substantially lower noise level of the LRI.

Both of the GRACE based analyses so far have focussed on a comparison between the new AOD1B data to the previous release RL06. A separate study by Ghobadi-Far et al. (2022) has focussed on the application of instantaneous LRI LGD and their ability to measure specific high-frequency mass variations. The analysis includes a comparison between RL06 and the new AOD1B data for the specific case of the Gulf of Carpentaria in the beginning of 2019 using along-track GRACE-FO data. This time and region are chosen specifically as a low-pressure system caused a significant amount of rainfall and flooding in the region which also coincided with an increased oceanic variability in the Gulf due to strong surface winds. By computing artificial LGD using either AOD1B RL06 or the new AOD1B data and comparing their difference to actual GRACE-FO along-track LGD, it is clear that the new AOD1B data better represents the oceanic high-frequency variability in the Gulf. While this analysis focused only on a specific highly localized event, it supports the other GRACE based comparisons between the AOD1B datasets and shows that the new data improves on a global and annual time-scale as well as on a regional level and short time-scales.

4.7 Comparison against satellite altimetry

To complete the assessment based on independent geodetic data, we also present a comparison with band-pass filtered along-track altimetry. Sea-level anomalies from the Jason satellites have previously been used to help to determine the accuracy of GRACE and underlying model data at sub-monthly timescales (Bonin and Chambers, 2011; Bonin and Save, 2021). While this method is not ideally suited for regions with a strong mesoscale activity or significant steric sea-level changes, it is still applicable for large parts of the open ocean especially when considered together with the GRACE-based analyses presented above.

The comparison is performed by using Jason-3 along track data for the year 2019 with all standard corrections applied. The sea surface height signals are averaged daily before the application of a 300-km Gaussian filter to each global grid in order to reduce noise. This produces datasets comparable in spatial resolution to the AOD1B grids. For both altimetry and background models, the respective mean is subtracted and the data is binned into cells of 3 degree width. To extract the variability in a 10 day (20 or 30 day) frequency band a sliding window based on a Gaussian distribution with a full width at half maximum of 7 days (15 or 23 days) and a window length of 20 days (30 or 47 days) is applied. Finally, the percent of explained variance (PVE) is computed using the altimetry data as a base series as given in Eq. 4.1,

$$PVE = \left(1 - \frac{\mathrm{var}(Alt. - Model)}{\mathrm{var}(Alt.)}\right) 100\%. \tag{4.1}$$

We show the differences in PVE between RL06 and v73/v74 using altimetry as a base series in Fig. 4.11. In all cases, red areas mark regions where the test-data better captures the variability observed by altimetry and vice-versa for the blue regions.

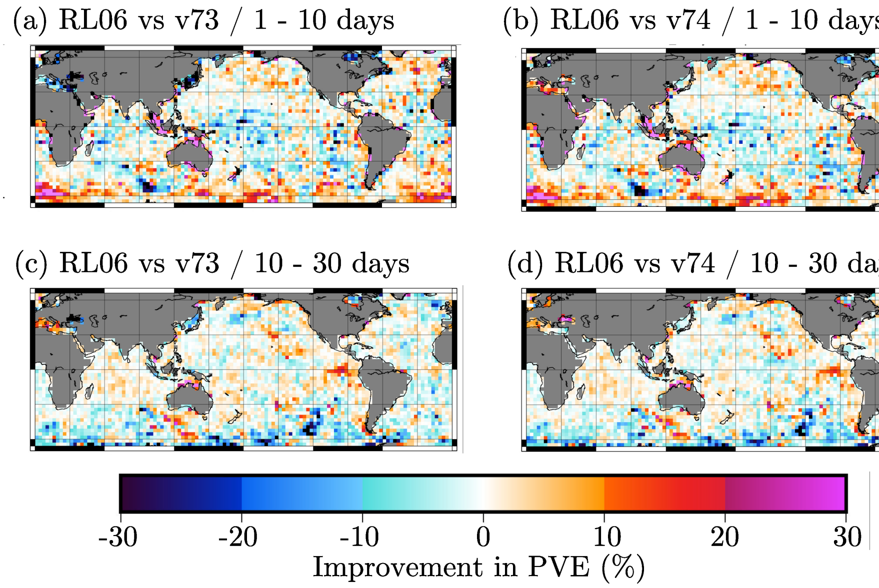

Figure 4.11: Differences in explained variance (PVE) between AOD1B RL06 and v73 (a & c) or v74 (b & d) using JASON altimetry data as the reference.

Table 4.4: Change in percent of altimetry's variance explained by AOD1B RL06 compared to v74 for different regions. Results are split into three frequency bands.

Region	Change in PVE [%]		
	P < 10 day	10 < P < 30 day	P < 30 day
Global	0.67	-0.45	0.55
Shallow Waters (<1000 m)	5.84	2.82	4.46
Deep Water, Tropics	-1.38	0.15	-0.09
Deep Water, Northern Lat.	1.29	-0.07	0.91
Deep Water, Southern Lat.	1.43	-2.18	0.20

In the high-frequency band, both test datasets show an improvement with respect to RL06 in regions of the Southern Ocean as well as some coastal areas such as the Gulf of Carpentaria or the Gulf of Thailand. For a region of the Southern Ocean south-west of Australia and some semi-enclosed seas however, RL06 still performs better. For the 10 to 30 days band there are still some improvements to be found in coastal areas but a reduced performance in the Southern Ocean.

In line with the two previous sections, we here also quantify the difference between v74 and RL06 by computing the change in PVE globally as well as for the oceanic regions described in Sect. 4.5. In order to give more detail on the temporal behaviour of the analysis, we split the results into three frequency bands. Results in Tab. 4.4 are given for frequencies below 10 days, between 10 and 30 days as well as all frequencies below 30 days. In general, the results match our findings in previous sections. Improvements are clearly visible on a global scale and especially in shallow regions. Mixed results are found for the tropics which can be linked to the generally low signal in the region especially in an analysis based on relative values. A reduction in performance is found in the low-frequency band in the Southern Ocean. Here RL06 clearly performs better than v74. The results are, however, compensated by a better performance in the high-frequency band resulting still in an overall improvement.

4.8 Summary and conclusions

In this section, we have assessed three new background model datasets in preparation of the next release RL07 of the GRACE Atmosphere and Ocean De-Aliasing Level-1B (AOD1B) product. The datasets v72 and v73 consist of an ERA5-based atmospheric component, while v74 is based on ECMWF operational data. The oceanic component of all three datasets derives from simulations with the MPIOM general ocean circulation model. In comparison to RL06, we now also utilise an ellipsoidal reference surface for the calculation of the Stokes coefficients. AOD1B RL07 is again provided as a spherical harmonic expansion complete up to d/o 180 and in the same format as the previous versions.

An assessment of 3-hourly tendencies of the ECMWF operational based data shows that there is little indication of an impact of IFS model changes which are known to have impacted AOD1B in the past (Dobslaw et al., 2016a). We also tested the possible gain of providing AOD1B with hourly resolution and found no significant improvements so that RL07 will retain the 3-hourly sampling introduced with RL06. The new background models have been also extensively tested with real geodetic data obtained by the satellites GRACE-FO and Jason-3. Results for K-band pre-fit residuals, LRI residuals, and band-pass filtered sea surface height anomalies are fairly consistent and document improvements with the new models both on a global scale as well as on a regional level and short time-scales. For the particular year 2019 assessed in this study, forcing data from the ECMWF operational model are slightly superior than the corresponding ERA5 dataset. We thus decide to use ERA5 until December 2017 so that it covers the whole GRACE mission period, and will continue with operational data from January 2018 onwards which is well before the launch of GRACE-FO. ERA5-based coefficients are also calculated internally for the years 2018 and 2019 to demonstrate the continuity across the transition period. Further details will be given in the next section of this thesis.

The final AOD1B RL07 data is publicly available at GFZs ISDC and published under Shihora et al. (2022a). The time-series, which starts in 1975 to allow for the consistent processing of the early SLR satellites, comprises several decades of data and is operationally updated every day in near-real-time. Given the length of the overall time-series, a secondary requirement of AOD1B, next to the accuracy of the background data, is its stability. This includes both trends on long time-scales as well as the short-term consistency, especially around changes in the underlying atmospheric data in 2018 or the impact of changes in the ECMWFs IFS. The next section thus focussed specifically on the stability of AOD1B RL07.

5

Assessing the stability of AOD1B atmosphere-ocean non-tidal background modelling for climate applications of satellite gravity data: long-term trends and 3-hourly tendencies

Given the the length of the GRACE and GRACE-FO time-series, which at this point includes over two decades of data, a large majority of the studies utilising satellite gravimetry data focus on trends and inter-annual variations of various mass-change signals over continents and oceans. This includes short and long-term trends in TWS (Rodell et al., 2018), ice-mass loss in Greenland (Sasgen et al., 2020) and Antarctica (Tapley et al., 2019) as well as sea-level variability (Chen et al., 2018) associated with the inflow of water from the continents. Additionally, recent efforts to estimate trends from GRACE and GRACE-FO level 1B data directly have allowed the study of trends with even higher resolution (Loomis et al., 2021). On the other hand, GRACE data have also been used in high-frequency or short-timescale analyses such as the analysis of storm-induced ocean mass variability (Ghobadi-Far et al., 2022), or rapid TWS increases due to flooding (Han et al., 2021).

As shown in the previous Section 3, AOD1B RL07 offers a better representation of the non-tidal high-frequency mass variations in the atmosphere and oceans and is thus expected to help reduce noise in the final gravity solutions of satellite gravimetry. However, especially in light of the above cited scientific applications of the final gravity data, AOD1B is not only required to accurately represent the high-frequency mass variations, but also feature stability and consistency over long time-scales from months to decades. Large trends, low-frequency signals or bias jumps in the background data could be erroneously introduced into the final gravity solutions where they are subsequently interpreted in an entirely different geophysical context. Especially over the continents, such trends might be interpreted in the context of TWS changes or ice-mass changes and have a significant impact on the applicability of the final results from the GRACE and GRACE-FO missions.
As so far most of the discussion has focussed on the accuracy of the new AOD1B release, i.e. the ability of the background model to accurately describe the mass variations in the Earths atmosphere and ocean, we now focus on the stability of the dataset as a second requirement for AOD1B. This includes an analysis of both the trends and annual signal as included in AOD1B RL07 (Sect. 5.1 and 5.2) as well as possible bias jumps by studying 3-hourly tendencies (Sect. 5.3). This is especially important for the transition from atmospheric reanalysis data to operational ECMWF forecast data, as it signifies a marked change in the dataset that carries the risk to induce inconsistencies. We present results for the atmospheric as well as the oceanic component of AOD1B and compare to alternative reanalyses as well as the previous release RL06. We also compare both releases in terms of difference in variability in Sect. 5.4 before concluding in Sect. 5.5 with a summary of the results in the context of the geophysical applications of satellite gravimetry.

5.1 Assessment of linear trends

As a first step, we analyse the trends in the components of AOD1B RL07 in order to assess their possible impact on the estimated GRACE gravity field time series. The analysis is split into the individual components of AOD1B, i.e. (i) the atmospheric surface pressure, (ii) contributions from density anomalies in the upper atmosphere, and (iii) ocean bottom pressure.

5.1.1 Surface pressure

Fig. 5.1 shows the linear trend for the atmospheric surface pressure as it is included in AOD1B RL07 in subfigure (a). It consists of data from the ERA5 reanalysis until 2017 followed by ECMWF operational data starting in 2018. To ensure that there is no impact due to the transition between the two datasets we also show the trend when using only the ERA5 reanalysis (b) as well as surface pressure from the MERRA2 reanalysis (Gelaro et al., 2017) as a reference. The trends are computed starting in January 2002 shortly before the launch of GRACE until the end of the year 2020.

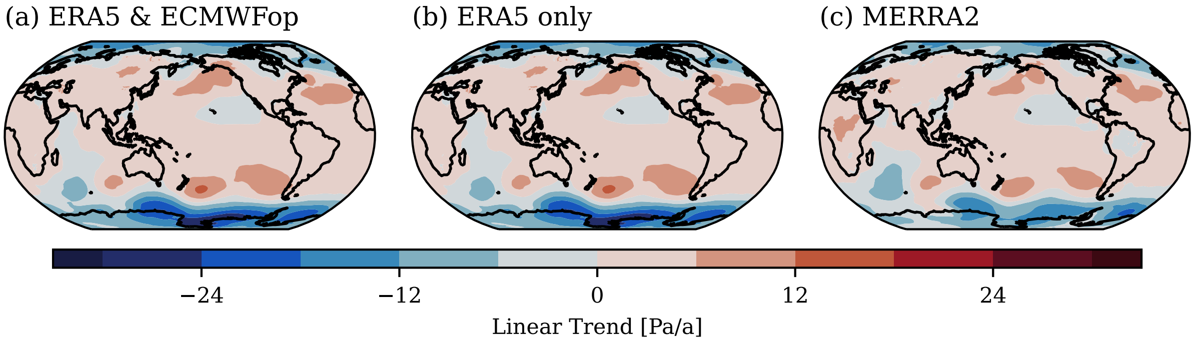

Figure 5.1: Linear trends in surface pressure as it is used for AOD1B RL07 as a combination of ERA5 (2002-2017) and ECMWF operational data (2018-2020) (a). As a reference, (b) and (c) show the linear trends in surface pressure when considering only ERA5 reanalysis data or the MERRA2 reanalysis. All trends are computed from 2002 to 2020.

We conclude that the surface pressure contribution to AOD1B RL07 does not include large trends. The largest local signals are found along the coast of Antarctica and in the Ross Sea with values of up to 30 Pa/a. Over the continents, values are even smaller reaching only up to 5 Pa/a. Trends using the combination of ERA5 and ECMWF operational data (Fig. 5.1a) are very close to the results obtained from using only the ERA5 reanalysis (Fig. 5.1b) indicating that the transition between the datasets does not have a significant effect. Surface pressure trends over the period from 2002 to 2020 from MERRA2 (Fig. 5.1c) show a very similar pattern to the other results. The largest trends are also found in the Southern Ocean close to Antarctica, although the trends are, with values of up to 15 Pa/a, slightly smaller.

Since AOD1B RL07 is produced all the way back to the year 1975, we also compute the linear trend over a longer time-period in Fig. 5.2. The figure shows the linear trend in ERA5 surface pressure for 1975 until 2020. For this period, trends are globally below 8 Pa/a and significantly below 5 Pa/a over the continents with a global average of 0.47 Pa/a. Comparing the trends on longer timescales to the results from Fig. 5.1, the feature along the coast of Antarctica is much reduced, indicating that the pattern is not related to long-term drifts but rather to inter-annual-to-decadal climate variability. In view of the strong variability in surface pressure in the area and the importance of atmosphere-ocean interactions on the long-term evolution of the regional atmospheric circulation, such a trend in the region is indeed plausible. However, the representation of surface pressure signals around Antarctica is likely less accurate due to a sparser coverage of

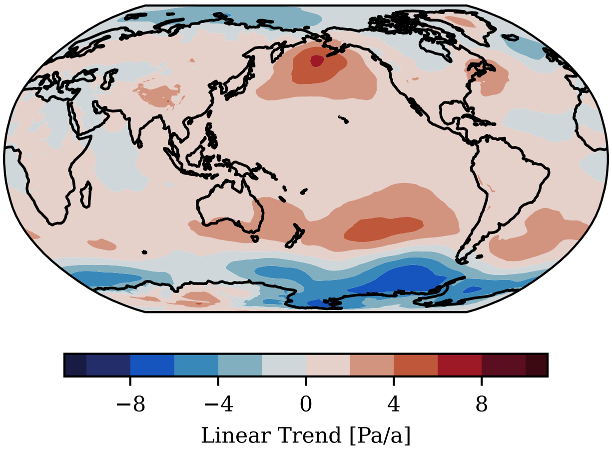

Figure 5.2: Linear trend of ERA5 SP from 1975 to 2020.

assimilated observational data. Part of this can be seen from the difference in trend between ERA5 and MERRA2. This also matches Hobbs et al. (2020) who report that the exact distribution and magnitude of long-term pressure changes around Antarctica varies in different reanalysis datasets. These uncertainties in the atmospheric data will also be considered for a new assessment of the remaining uncertainties of AOD1B RL07 as described in Sect. 6.

5.1.2 Upper-air density anomalies

In addition to surface pressure anomalies, AOD1B RL07 takes the contribution of upper air density anomalies (Swenson and Wahr, 2002) over both continents and oceans into account. To visualize the effects in an accessible way, we transform the upper air gravitational effects into apparent surface pressure variations that would have caused the same effect on the gravity field outside the atmosphere for the trend assessment presented here.

Fig. 5.3 shows the linear trend in the contribution of upper-air density anomalies computed for the years 2002 to 2020. Trends are much smaller compared to contributions from atmospheric surface pressure due to the comparatively small deviations from the hydrostatic balance. Regionally, those trends do not exceed 0.5 Pa/a and for most of the grid points values are even much smaller. On an area-weighted global average, the linear trend amounts to about 0.05 Pa/a which is well within the expected range of natural climate variability and will thus not introduce any artificial trends into AOD1B.

5.1.3 Ocean bottom pressure

OBP forms the third major component of the non-tidal mass variability represented by AOD1B. Transient simulations with MPIOM and forcing from either ERA5 or the op-

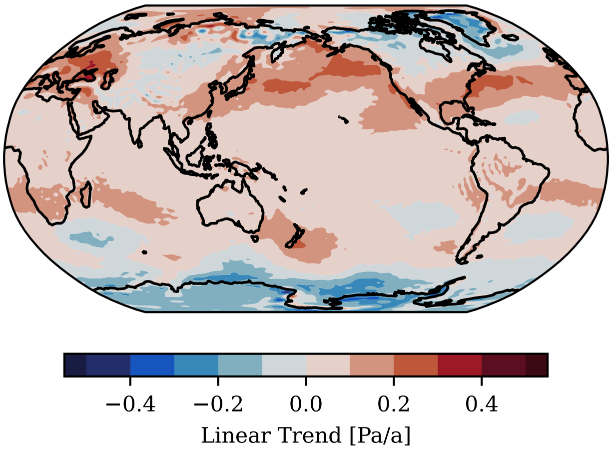

Figure 5.3: Linear trend of the upper-air density anomalies from 2002 to 2020 as included in AOD1B RL07.

erational ECMWF data are used to calculate OBP fields every 3 hours. Especially for oceanic applications of satellite gravimetry, large secular trends in the simulated OBP can also significantly reduce the quality of the gravity field solutions, since monitoring the long-term increase in ocean mass is one of the most important science goals of satellite gravimetry in maritime regions (Chambers et al., 2010).

In Fig. 5.4a, we present the trend in OBP as it is used in AOD1B RL07 based on ERA5 atmospheric forcing until 2017 and operational ECMWF forcing data from 2018. Similar to Sect. 5.1.1, we also compare to OBP trends using only ERA5 atmospheric forcing in the MPIOM simulation (b) in order to gauge the impact of changed forcing data. Additionally, we compare the trends to the previous release 06 of AOD1B (c). Similar to before, all three trends are computed over the period 2002 – 2020.

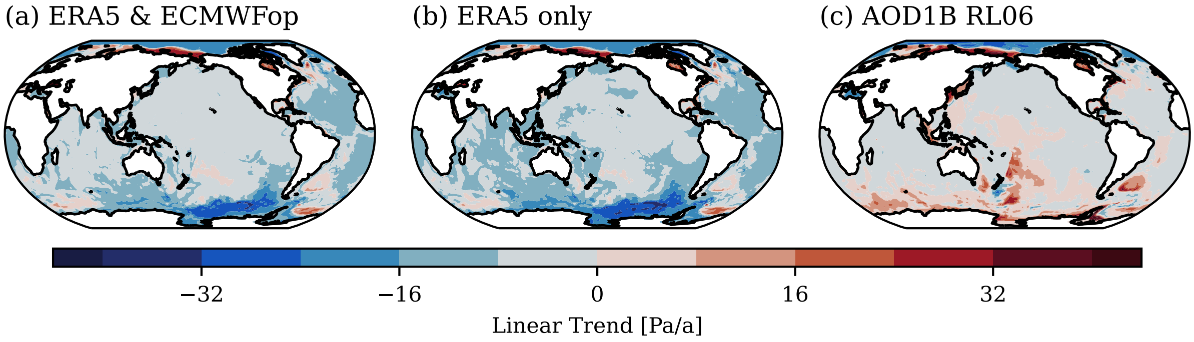

Figure 5.4: Linear trends in the ocean bottom pressure contribution as included in AOD1B RL07 (a) where both ERA5 and ECMWF operational atmospheric forcing data are employed. (b) shows the linear trend when only employing ERA5 atmospheric forcing data. (c) shows the linear trend from AOD1B RL06 for comparison. All trends are computed from 2002 until 2020.

Trends in the oceanic component of AOD1B (Fig. 5.4a) are regionally around 20 Pa/a. The largest trends are found in the south in the region of the ACC, especially in the Bellingshausen Basin. This region experiences some of the highest wind speeds on Earth, and signals in Fig. 5.4 reflect an adjustment of the ocean dynamics to the atmospheric forcing in a region where the shape of the ocean's bathymetry favours resonant ocean mass redistribution. Additionally, shallow parts of Arctic Ocean show trends of similar magnitude but opposite sign. On a global average, the absolute magnitude of linear trends is below 7 Pa/a.

Comparisons with OBP trends based on ERA5 atmospheric forcing only (Fig. 5.4b) reveal very little impact from the transition in forcing data. Both regional patterns as well as the magnitudes of trends are highly similar. Trends in the previous release 06 of AOD1B are generally comparable in magnitude, but show a different regional pattern. Whereas the trends in the Arctic Ocean are largely the same, trends in the Southern Ocean are not as clearly defined. Instead, there are smaller regions with locally increased trends. We attribute these patterns primarily to an insufficient spin-up of the ocean simulation, which has been extended to 2000 years for RL07, and also to the consequences of the higher quality of the (more recent) atmospheric reanalysis data utilised for RL07.

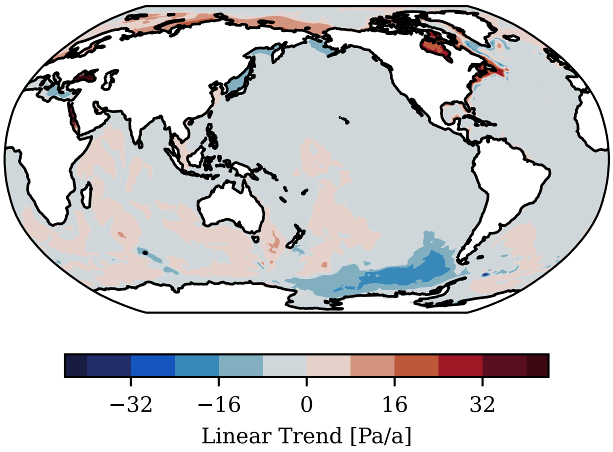

Figure 5.5: Linear trend of MPIOMs OBP from 1975 to 2020.

We also compute the linear trend in OBP over a longer period from 1975 until 2020 in Fig. 5.5. Whereas the spatial pattern in the Southern Ocean is very similar to results in Fig. 5.4a, the overall magnitude of the trend is reduced. Trends in coastal areas and the Arctic Ocean are also significantly smaller. We therefore conclude that the trends in OBP, which are of a comparable amplitude to surface pressure trends, are at an acceptable level of accuracy in AOD1B RL07, but a tiny contribution of artificial drift from the ocean model might still enter the gravity fields.

For comparison, Rodell et al. (2018) estimate the uncertainty of the GRACE-based TWS trend for Antarctica to be ∼40 Gt/a which corresponds to about 0.3 cm/a equivalent water-height which is still larger than the ERA5-based trend signal over the Antarctic region. Similarly, the uncertainty of global ocean mass change as estimated by GRACE is given by Tapley et al. (2019) to be ∼0.4 mm/a which is on the same order of magnitude as the globally averaged OBP trends in AOD1B RL07. Please note that although Chen et al. (2022) give estimates on the order of ±0.05 mm/a, this number is based on the misfit of the GRACE data in the linear regression and does not include uncertainties based on e.g. glacial isostatic adjustment (GIA) and geocenter motion which have additional impacts of ∼ ±0.3 mm/a (Chambers et al., 2010) or ∼ ±0.21 mm/a (Blazquez et al., 2018), respectively.

Whereas the drift remaining in AOD1B RL07 is acceptable at the current level of GRACE-based trends, further efforts are certainly needed in case that a future gravity mission of the next generation is being implemented, which probably shall provide more accurate gravity field data from better instruments, more satellites, and lower orbit altitudes as well as extend the time-series of gravity solutions. In addition, care must be taken in handling background model information when it comes to the computation of GRACE-based trends, as the residual drift in AOD1B is now on the order of magnitude of GRACE trend uncertainties.

5.2 Assessment of the annual signal

Next to long-term linear trends, the accuracy of low-frequency signals, such as annual variations, is of interest. In principle, these long-term signals do not contribute to the temporal aliasing in the gravity field solutions. As satellite gravimetry is, however, inherently incapable of distinguishing between individual vertical contributions to mass variations, background models are often applied also for signal separation. In the analysis of TWS data for instance, atmospheric mass variations must be removed by subtracting the variations as represented by AOD1B. As a result, a proper representation of longer frequencies, such as the annual signal, can be important in many applications of the gravity data.

In Fig. 5.6 we show the amplitude of the annual variations in surface pressure based on ERA5 (Fig. 5.6 a) and MERRA2 (Fig. 5.6 b) data from 2002 to 2020.

The signal is largest over Greenland, where amplitudes of over 12 hPa are reached. Similarly large signals can be found in some coastal areas such as the East China Sea or the Persian Gulf. Over most of the ocean, however, the amplitude is typically below 1 hPa. Comparing the amplitudes from the two reanalyses shows a very small difference. Most of the differences are found in regions with steep orographic gradients which might

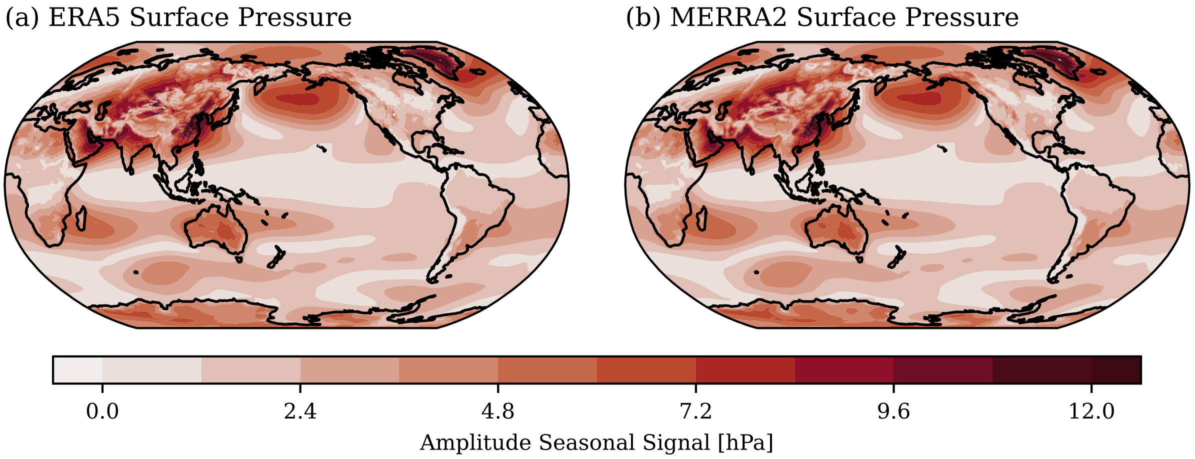

Figure 5.6: Amplitude of the seasonal signal from ERA5 (a) and MERRA2 (b) surface pressure estimated from 2002 to 2020.

be the cause of some of these differences as we did no adjustment to a common orography. The spatially averaged absolute value of the difference reaches only 11 Pa which, given the magnitude of the annual signal, is negligible. The small discrepancy can be attributed to the large weight of the in-situ barometer observations that is similarly assimilated in both reanalyses.

5.3 Assessment of 3-hourly tendencies

So far, the assessment of the individual components of AOD1B RL07 has focused only on the stability over decades. However, errors on short timescales such as bias changes, can have an equally adverse impact on GRACE gravity field solutions (Fagiolini et al., 2015). In this section, we examine 3-hourly tendencies which are an effective statistical metric to reveal abrupt jumps or other subtle discontinuities in the underlying data. 3-hourly tendencies are here defined as the differences between consecutive 3-hourly time-steps and are thus a measure of the amount of change from one data epoch to the next. A sudden large peak in the tendencies would be an indicator of a possible bias jump, which would require further scrutiny. We focus here again on the individual components of RL07, namely the atmospheric component which combines the surface pressure anomalies and the upper air density contributions, as well as the oceanic component. We place a special focus on the transition between the ERA5 and operational ECMWF atmospheric data as this marks a significant change within the time-series where ensuring consistency is particularly important since it coincides with the gap between the two missions GRACE and GRACE-FO.

5.3.1 Atmospheric component

First, we consider the tendencies of the atmospheric contribution to RL07. In Fig. 5.7 we show the 3 hourly tendencies as a single time-series by computing the area-weighted mean of the absolute value of the tendencies. The time-series is shown for RL07 (a) as well as RL06 (b) for comparison. The dotted vertical line marks the epoch of transition from reanalysis to the operational ECMWF atmospheric data in the respective release (i.e., January 1st, 2007 in RL06, and January 1st, 2018 in RL07).

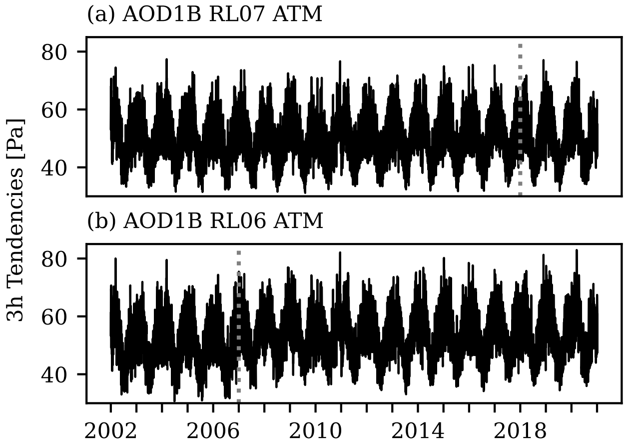

Figure 5.7: Area-weighted spatial mean of the absolute value of 3-hourly tendencies for the atmospheric component of AOD1B. Results are shown for RL07 (a) and RL06 (b). The transition from reanalysis data to operational ECMWF data is indicated by the vertical dotted lines.

The atmospheric tendencies for RL07 are largely comparable to the corresponding results from RL06. Both the overall magnitude of the tendencies as well as the scatter of the intra-annual variations agree well as shown in Fig. 5.7. In addition, there is no evidence for trends or significant peaks visible which would indicate a bias jump in the atmospheric data. While RL06 shows a slight increase in the tendencies after 2007 due to the change in spatial resolution after the transition from ERA-Interim to operational ECMWF data, the impact of the transition for RL07 in 2018 is even smaller.

5.3.2 Oceanic component

Next, we consider the tendencies for the oceanic component of AOD1B RL07. Similar to the previous section, we compute the area-weighted absolute value of the tendencies to arrive at time-series for both RL06 and RL07 as shown in Fig. 5.8. Both tendency time-series are comparable in terms of seasonal variation, however, the RL07 results show overall slightly larger values. In addition, there is a change in the tendencies visible over the transition from reanalysis to operational atmospheric forcing data. In RL07, we note a decrease in the tendencies after 2018, whereas for RL06 the oceanic tendencies increase after 2007. For RL06, the change from ERA-Interim to operational ECMWF data included a notable change in spatial resolution and as a result shows a slight impact on the variability in the MPIOM simulation. The change in RL07 is rather due to the different atmospheric forcing frequency in the simulation. As RL07 aims to take full advantage of the newly increased 1-hourly resolution of the ERA5 reanalysis, the transition to operational data also includes a reduction in the forcing frequency of MPIOM to 3-hourly sampled forcing fields. As a result, a decrease in the variability from each time-step to the next is found, since advected atmospheric fronts are less sharply defined with fewer time-steps. The sensitivity to the change in atmospheric forcing thus shows that the tendencies can indeed identify even very subtle changes in the underlying data.

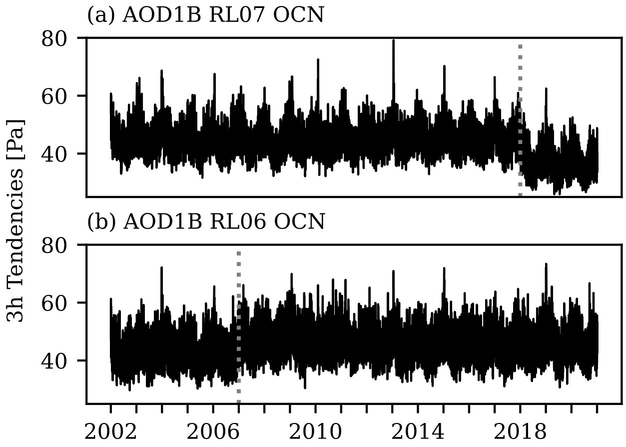

Figure 5.8: Area-weighted spatial mean of the absolute value of 3-hourly tendencies for the oceanic component of AOD1B. Results are shown for RL07 (a) and RL06 (b). The transition in atmospheric forcing data from reanalysis to operational ECMWF data as is indicated by the vertical dotted lines.

We also show the tendencies for a much shorter period around the transition in forcing data in Fig. 5.9 to ensure that there are indeed no abrupt changes. The figure shows the tendencies for two months around the transition to operational forcing for the oceanic part of RL07. As a reference, we also show the tendencies over the same period for RL06 which does not include any change in atmospheric data during that time. The comparison between the two time-series reveals no conspicuous features. While the tendencies decrease, they do so rather smoothly and well within the usual range of the otherwise typical variability.

As the analysis has so far focused on the consistency on a global scale, we now also analyse the impact of the forcing transition in two key regions of the world. Fig. 5.10 (a) shows the tendencies around the transition epoch for the Arctic Ocean, which is usually under-represented in the global average analysis due to its rather small total area but

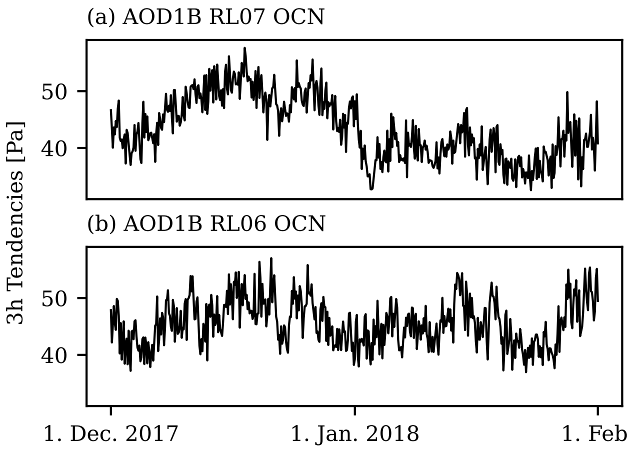

Figure 5.9: Area-weighted spatial mean of the absolute value of 3-hourly tendencies for the oceanic component of AOD1B for the transition from 2017 to 2018 which signifies the transition in the atmospheric forcing data. Results are shown for RL07 (a) and RL06 (b).

features a comparatively high variability in OBP. In Fig. 5.10 (b), we show tendencies for the Baltic Sea, which is a semi-enclosed sea and thereby challenging to model given the spatial resolution of MPIOM. Whereas the tendencies for those two regions show a larger amount of variability than the global average, there is no indication of an adverse impact of the transition in atmospheric forcing data even on those regional scales.

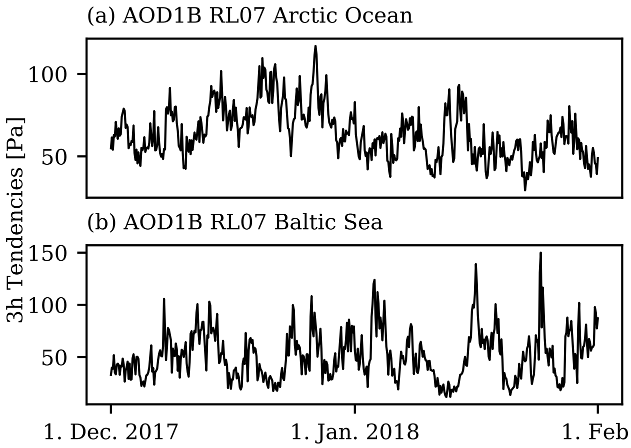

Figure 5.10: Area-weighted spatial mean of the absolute value of 3-hourly tendencies for the oceanic component of AOD1B RL07 for the transition from 2017 to 2018 which signifies the transition in the atmospheric forcing data. Tendencies are computed using only the Arctic Ocean (a) or the Baltic Sea (b).

A second notable feature of the tendencies shown in Fig. 5.8 (a) are small peaks that appear at irregular intervals in some years. Those peaks are visible at the same times also in the tendencies calculated from RL06. As they appear in two separate time-series that are based on both different ocean model configurations and different atmospheric forcing datasets, they are likely a physical feature in the simulation rather than a bias jump. To verify, we first show a detailed view of the tendencies for one of the peaks in Fig. 5.11. The figure shows that the increase in tendencies is not due to a single time-step, which would indicate a bias jump, but instead stretches for about 1 week around the end of December 2018. As the time-series shown in Fig. 5.11 is based on a spatial average, we also determine the spatial distribution of the increased tendencies. We average the absolute value of the tendencies for the week of increased tendencies and subsequently subtract a long-term mean. The difference is shown in Fig. 5.12. Regions that contribute to the temporary increase in tendencies are thus shown as spatially coherent positive signals. Based on the figure we can identify three core regions which have the largest contributions: the Mozambique Channel, the Tasman Sea and the western equatorial Pacific. All three of these regions are, due to their basin-geometry, resonant at very short periods extending over a few hours. This can be readily seen for example from the spatial distribution of semi-diurnal ocean tides (Sulzbach et al., 2021). While other regions in Fig. 5.12 also show a positive difference, such as the Arctic or the North Sea, a close inspection of the time-series of these regions reveals that they do not contribute to the temporary increase in variability. These regions, instead, have a generally larger variability and thus happen to feature in the figure. Based on the assessments of Figs. 5.11 and 5.12, we conclude that the increase in variability is not due to a change in bias or a technical issue but rather caused by occasionally happening resonances in certain oceanic regions.

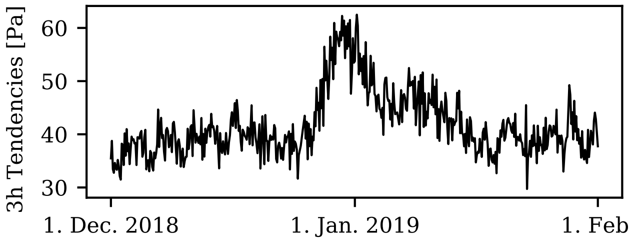

Figure 5.11: Area-weighted spatial mean of the absolute value of 3-hourly tendencies for the oceanic component of AOD1B RL07 from Dec. 2018 to Feb. 2019.

5.3.3 ERA5 Back Extension

As AOD1B RL07 is starting in 1975, the first four years are based on the so-called Back Extension of the ERA5 reanalysis (Bell et al., 2021) which covers the years from 1950 to 1978. To assess the transition between the Back Extension and the regular ERA5 data, we also compute tendencies for the components of AOD1B RL07 across the transition. Fig. 5.13 shows the area-weighted absolute value of the tendencies for both the atmosphere (Fig. 5.13 a) as well as the oceanic component (Fig. 5.13 b) from 1978 to 1979.

The 3-hourly tendencies clearly show an impact of the change from Back Extension to

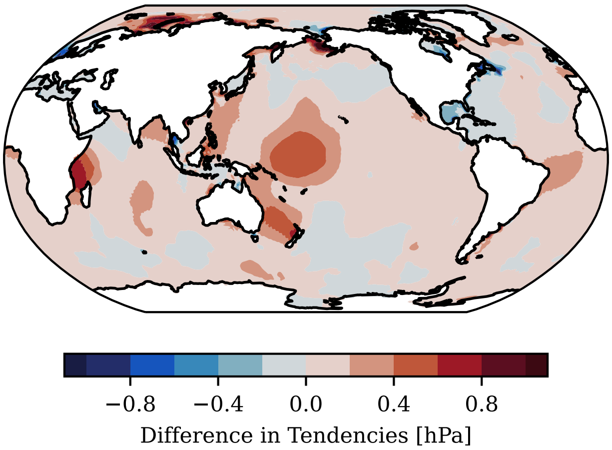

Figure 5.12: Spatial distribution of the increased tendencies for the last week of Dec. 2018. Tendencies are averaged over 1 week around the increase in the tendencies and a long term mean is subsequently subtracted.

the regular ERA5 data both for the atmosphere as well as the simulated OBP data forced with the atmospheric data. For the atmosphere, the Back Extension based data exhibit a significantly larger variation in the tendencies. Bell et al. (2021) report a significant improvement in the quality of the surface pressure data beginning in 1979 coinciding with the introduction of the TIROS Operational Vertical Sounder (TVOS) satellite data (see Fig. 9 of Bell et al. (2021)). A corresponding change is visible in the oceanic tendencies as well. Both the variation as well as the overall magnitude of the 3-hourly tendencies changes across the transition.

While the impact is not overly large, there is thus a change in the highest frequencies of AOD1B RL07 for the earliest years. We believe that this will not significantly impact applications such as the processing of the earliest SLR satellites as the accuracy of the early SLR tracking data is significantly lower than today. As an example, the assimilation of normal points for the ITRF2020 from the ILRS starts in 1983 (Noll et al., 2019) only, which is in part driven by the reduced accuracy of instruments as well as a poorer coverage of ground stations. Nonetheless, the impact of the lower accuracy of the ERA5 Back Extension based years in AOD1B should be kept in mind when using the years 1975 to 1979 for any geodetic application.

5.4 Comparison to AOD1B RL06

We finally assess the overall impact of the various changes in AOD1B RL07 on the surface mass variability in general. To that end, we compare the so called GLO coefficients – which combine the effects of atmosphere and ocean and are routinely applied during

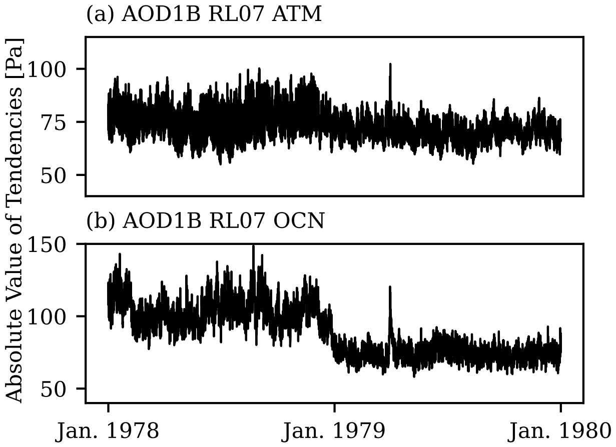

Figure 5.13: Area-weighted spatial mean of the absolute value of 3-hourly tendencies. Results are given for surface pressure (a) as well as AOD1Bs oceanic component (b) for 1978 - 1979. The period covers the transition from the Back Extension to regular ERA5 reanalysis data.

the GRACE gravity field processing – from RL06 and RL07. In Fig. 5.14 we show the standard deviation difference between the GLO coefficients that have been re-synthesized from the Stokes coefficients into the spatial domain.

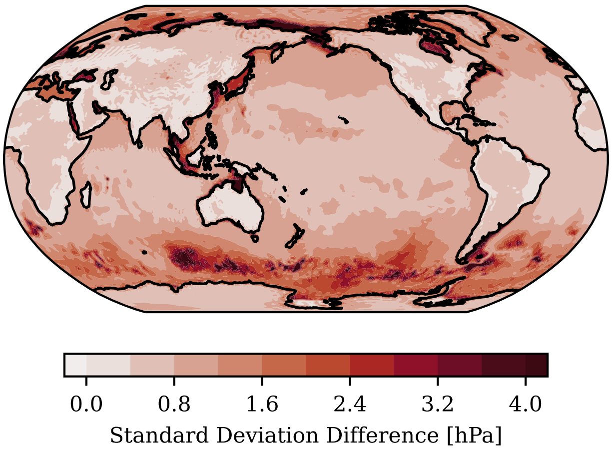

Figure 5.14: Standard deviation of the difference between AOD1B RL07 and RL06 GLO coefficients after re-transformation from spherical harmonic coefficients.

The difference in variability between RL07 and RL06 generally reaches an amplitude of about 4 hPa on regional scales. Especially in the Southern Ocean and the region of the ACC as well as several coastal areas. In contrast, the differences over the continents are significantly smaller and are well below 1 hPa. Generally, the differences in the atmospheric contribution between RL07 and RL06 are much smaller than in the oceanic component. This is largely due to the common code base of the ERA5 and ERA-Interim reanalyses which are the basis of the RL07 and RL06 atmospheric components, respectively. The oceanic component, as it is based on unconstrained ocean simulations, has undergone more significant changes such as the inclusion of the feedback of SAL to the ocean dynamics (Shihora et al., 2022b). In combination with the change to the ERA5 reanalysis as atmospheric forcing data which offers higher spatial and temporal resolutions, this changes the OBP signals significantly, as shown in the previous section. Together with differences due to intrinsic variability which are prominent in the Southern Ocean (Zhao et al., 2021), and the lack of observational constraints, larger differences in the oceanic components between RL07 and RL06 are the consequence.

Whereas validation of the previous RL06 of AOD1B with altimetry (Bonin and Save, 2020) and experimental daily GRACE solutions (Schindelegger et al., 2021) have indicated deficiencies especially for the ocean component of AOD1B, we are confident that differences between RL06 and RL07 as visible in Fig. 5.14 reflect in particular improvements in the high-frequency mass variations as evidenced in the previous section. This, however, raises the question of how large the remaining uncertainties are, so that residual errors in background modelling can be properly incorporated into the stochastic modelling of the GRACE gravity field processing. The latest thorough error assessment for AOD1B is based on AOD1B RL05 (Dobslaw, 2016), which was vetted as applicable to RL06 within a subsequent simulation study (Poropat et al., 2019). Differences found between RL06 and RL07 suggest, however, that this assessment is no longer representative and needs to be revisited. This is especially important, as the inclusion of background model uncertainties has been shown to have a positive impact on the gravity field estimation process (Zenner et al., 2010; Kvas et al., 2019) and in dedicated mission performance simulation studies (Abrykosov et al., 2021). We will thus revisit this topic in Sect. 6 of this thesis.

5.5 Summary and conclusions

With the production of the new release of AOD1B RL07, which covers over four decades of data (starting in 1975), an assessment of the stability over both long and short time-scales is highly important. We thus have assessed both long-term trends as well as short-term inconsistencies such as bias jumps that might have a significant impact on the GRACE gravity field solutions.

Section 5.1 focused on identifying and quantifying potential long-term trends in all three components of AOD1B: the atmospheric surface pressure anomalies, contributions from density anomalies in the atmosphere and OBP anomalies. For all three components we conclude that the existing trends are at an acceptable level for the inclusion in AOD1B RL07. The largest contribution to the linear trend, when computed over a 40 year time-span, comes from the oceanic component where trends still do not exceed 30 Pa/a. Trends over the same period for the atmospheric contributions are much smaller. GRACE-based trends, such as analysed by Loomis et al. (2021) or TWS based trend as published by Rodell et al. (2018), are generally on the order of 1 cm/a which is equivalent to 1 hPa/a. The uncertainties of the trends are, as an example, estimated to be on the order of 30 Pa/a equivalent water-height for ice-mass loss in Antarctica and thus still larger that the trends included in AOD1B RL07. Atmospheric trends in AOD1B RL07 are also comparable to previous releases and current state-of-the-art reanalysis data which, due to their observational basis, do not include large artificial trends. For the ocean, the trends are acceptable given the current accuracy of satellite gravimetry based trend analyses. For future gravity missions, however, efforts should be made to further reduce the remaining drift.

To assess the consistency over short time-scales the analysis included the computation of 3-hourly tendencies for the atmospheric and oceanic contributions separately. These tendencies are defined as differences between consecutive 3-hourly time-steps. The change in the atmospheric forcing of the ocean simulation from reanalysis data to operational ECMWF data can be identified in the tendencies, showing that they are indeed a sensitive diagnostic to identify possible issues. They have also been employed for the assessment of previous releases of AOD1B and have helped to identify possible model changes such as changes in the integrated forecast system of the operational ECMWF atmospheric data which might include changes in the resolution. As they are also an easily computed quantity, tendencies make a useful tool for the assessment of other model-based datasets both during preparation as well as during operational production. At GFZ, this includes effective angular momentum functions (Dobslaw et al., 2010) and non-tidal loading grids (Dill and Dobslaw, 2013) which are produced from data sources similar to AOD1B.

A closer examination of the transition in atmospheric forcing in the ocean simulation shows that there are no inconsistencies or bias jumps induced by the change. This is found to be true also for rather sensitive areas of the ocean domain such as the Arctic Ocean or the Baltic Sea.

An additional assessment of the impact of the ERA5 Back Extension, which is used for the years 1975 to 1978 of AOD1B RL07, shows that there is indeed a difference in the variability of atmospheric surface pressure and thus also simulated ocean bottom pressure. While this will likely not negatively affect the processing of e.g. the earliest SLR satellite data, these differences should be kept in mind when using the earliest years of AOD1B. In summary, there is no indication of unexpected behaviour that could negatively affect the application of the background model data in either the oceanic or atmospheric component of AOD1B RL07 especially for the application in satellite gravimetry from GRACE and

GRACE-FO.

Atmospheric and oceanic background models are not only applied in the processing of satellite gravimetry but are also applied in e.g. altimetry via the Dynamic Atmospheric Corrections (DAC) product (Carrere and Lyard, 2003; Carrere et al., 2016). Also for these background models, tendencies can be a valuable tool for the routine assessment of the consistency of the data due to their sensitivity to model changes or inconsistencies and their straightforward computation.

Lastly, this section assessed the differences in the mass variations of RL06 and RL07. The largest differences are found in the ocean domain, which is to be expected given then more significant changes in the ocean model configuration for RL07. As analyses of RL07 indicate a globally improved representation of the mass variations with respect to RL06, we conclude that previous studies on the uncertainties of AOD1B are not sufficiently applicable to RL07 and suggests a new assessment of the residual uncertainties in AOD1B.

6

Updated uncertainty assessment for AOD1B RL07: AOe07

There are different approaches for mitigating the impact of residual aliasing errors in GRACE data processing. Most notably, several studies have shown that including an estimation of the uncertainty of the background model data can have a significant impact on the quality of the gravity field solutions. Zenner et al. (2010) and Kvas et al. (2019) suggested that including uncertainty estimations allows a weighting of the measurements according to the associated model error. As a result, measurements associated with a larger model uncertainty have a reduced impact on the final gravity field solutions and therefore mitigate some of the effects from residual temporal aliasing. Similarly, employing the uncertainty estimates of ocean tide models has been shown to have a positive impact on the gravity solutions in dedicated performance simulation studies (Abrykosov et al., 2021).

While assessments of the residual errors of AOD1B have been performed in the past (Dobslaw et al., 2016b), they were only based on AOD1B RL05. Even though been found to be applicable to AOD1B RL06 as well (Poropat et al., 2019), this assessment is now believed to be no longer representative for the uncertainties of AOD1B RL07 given the numerous changes made over the last two releases and as presented in the previous sections. In this part of the thesis, we thus derive a new estimation of the non-tidal atmosphere and ocean background model errors associated with AOD1B RL07 that can be readily used in the gravity field estimation process of satellite gravimetry as well as in simulation studies.

This is especially timely, given the ongoing efforts towards developing future generations of satellite gravimetry missions which include both double-pair constellations as well as novel quantum gravity concepts (Schlaak et al., 2022; Zhou et al., 2023).

This section starts with an assessment of the signal content in AOD1B RL07 and how the represented variability has changed, especially for the oceanic component in Section 6.1. This is done by comparing the AOD1B update to the ITSG2018 daily gravity field solutions (Kvas et al., 2019; Mayer-Gürr et al., 2018). Next, an estimation of the uncertainties in the atmospheric component of AOD1B through a comparison of the employed ERA5 reanalysis data to other state-of-the-art atmospheric reanalyses (Sect. 6.2) is developed. In Section 6.3 we focus on the uncertainties in the oceanic component which are addressed through ensemble simulations where we quantify both the impact of the atmospheric forcing as well as the impact of the intrinsic variability. The derivation of a new time-series of true errors representative of the uncertainties within AOD1B RL07 is presented in Section 6.4 and the computation of new error variance-covariance matrices for the application in simulation studies will be described in Section 6.5. The section concludes with early application examples of the newly derived stochastic information for GRACE-like simulations (Sect. 6.6) and a summary in Section 6.7.

6.1 Comparing AOD1B to ITSG daily solutions

We start by examining the signal content of AOD1B RL07 in relation to residual signals remaining in previously published GRACE/GRACE-FO gravity field time-series. A comparison of the new release RL07 to its predecessor RL06 shows that the largest differences in variability are found in the oceanic domain. The atmospheric differences over the continents are in contrast much smaller as shown in Sect. 5. This can be expected given the lack of assimilated observations in the ocean simulation. In turn, this also suggests that the uncertainties of AOD1B are going to be dominated by the dynamic contribution of the simulated OBP. To assess the degree to which the oceanic mass variations are not captured in RL07 we make use of a series of daily gravity field solutions provided by the Institute of Geodesy at Graz University of Technology (ITSG). ITSG-GRACE2018 (ITSG2018 in the following) is provided in terms of spherical harmonic coefficients up to d/o 40 and is based on a combination of GRACE measurements and prior stochastic information in a Kalman-smoother framework (Kvas et al., 2019; Mayer-Gürr et al., 2018). These daily solutions incorporated AOD1B RL06 in its processing in conjunction with the previous estimate of the associated AOD1B uncertainties. They thus represent residual mass variations not captured by AOD1B RL06. Due to their observational basis

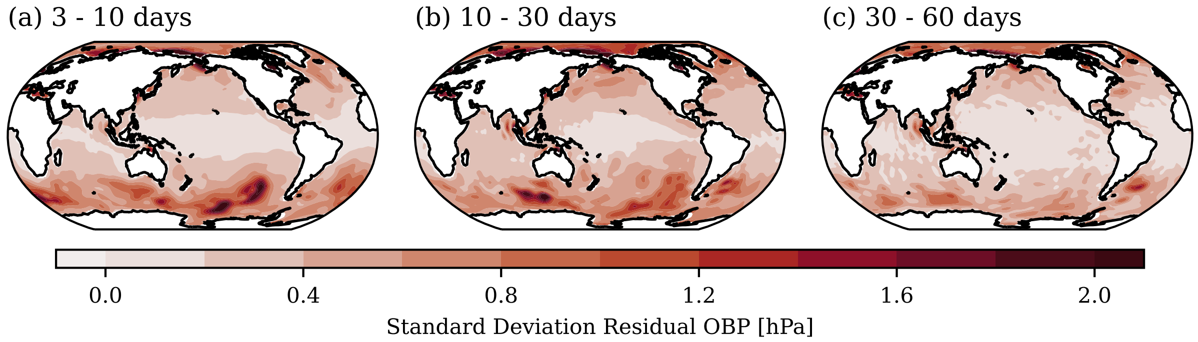

Figure 6.1: Standard deviation of the residual circulation signal given by the ITSG2018 daily gravity field time-series. Results are bandpass filtered into 3 frequency bands: 3 – 10 days (a), 10 – 30 days (b), 30 – 60 days (c). Note that the residual circulation given by ITSG2018 already includes the AOD1B RL06 background model data.

and global coverage, the daily gravity field solutions have already been applied successfully in several oceanic applications (Bonin and Save, 2020) and were also utilised in the assessment of differences in high-frequency ocean model simulations (Schindelegger et al., 2021).

For our analyses, we synthesise an equiangular one-degree grid based on spherical harmonic coefficients from daily ITSG2018 solutions for 2004 to 2006. Similar to the approaches of Eicker et al. (2020) and Schindelegger et al. (2021), we transform a binary land-ocean mask from spherical harmonics onto the same grid and reject all grid-points with a value below 0.8 to generate a coastal buffer. As a reference, the resulting standard deviation of the residual OBP signal of the ITSG2018 solutions is shown in Fig. 6.1 for three frequency bands as obtained from a fourth order Butterworth filter. The variability is shown for 3 – 10 days (Fig. 6.1 a), 10 – 30 days (Fig. 6.1 b) and 30 – 60 days (Fig. 6.1 c).

For the highest frequencies, the residual OBP variations are mainly located in coastal regions as well as in the Southern Ocean in the band of the ACC. Especially in the Bellingshausen Basin the residual variability reaches values up to 2 hPa, i.e. 2 cm in equivalent water-height. The picture is similar for the moderate frequencies (10 – 30 days) although the strongest signals are now found south-west of Australia. For the longest frequencies we consider here (30 – 60 days), the residual OBP variability is generally much weaker suggesting that the OBP variations at these frequencies are better captured by the AOD1B RL06 background model data which was subtracted during the satellite data processing.

Next, we consider the impact of the new release AOD1B RL07 on the residual OBP variations. As the ITSG2018 time-series already considers the AOD1B RL06 background model data, we compare the ITSG signal content only to the update of AOD1B, i.e. the difference (RL07 - RL06). We then assess the impact of the model update by computing explained variances using:

$$\mathrm{PVE} = \left(1 - \frac{\mathrm{var}(\mathrm{ITSG} - \Delta_{\mathrm{AOD1B}})}{\mathrm{var}(\mathrm{ITSG})}\right) \tag{6.1}$$

where Δ_{AOD1B} is the update to the AOD1B background model data through RL07. The results are shown in Fig. 6.2 for the same three frequency bands as before. In all three bands there are clear regions where the update to AOD1B captures part of the residual circulation signal (red) and regions where the update does not capture the residual variability (blue). The blue regions are found especially for the highest frequencies in the lower latitudes. While the same is true for the 10 – 30 day and 30 – 60 day bands, the effect is less pronounced. Regions where the AOD1B update captures the residual variability are in all three cases found in the band of the ACC as well as in the Arctic Ocean for the medium and long periods. Comparing the results to the amount of residual variability presented in Fig. 6.1 shows that the regions with negative explained variances correspond largely to areas where there is very little residual variability present in the ITSG time-series. This is especially clear for the shortest periods where the ITSG variability around the equator is close to zero. As a result, the explained variances, which are a metric relative to the ITSG variability, likely appear as highly exaggerated. When focusing only on regions with a significant amount of residual circulation signal, however, it turns out that these correspond to the areas with a positive explained variance. Examples are for instance the Bellingshausen Basin for the 3 – 10 days band, or off the coast of south-western Australia in the 10 – 30 days case. This suggests that, while not all of the residual circulation is captured by the AOD1B update, at least some part of the variability is indeed better represented by the new release AOD1B RL07. Those conclusions also match nicely with previous evidence based on satellite altimetry and GRACE-FO along-track data presented in Sect. 4.

Based on the results presented so far, there are local improvements when considering the new release of AOD1B. However, not all of the residual oceanic mass variations present in the ITSG2018 daily solutions are captured. Given these changes, the uncertainty of the background model data can be expected to show significant changes compared to the earlier estimation of Dobslaw et al. (2016b) and a new assessment is certainly required. In the following section, we thus focus on the calculation of a new realisation of true errors for AOD1B RL07 based on model differences from atmospheric reanalyses as well as differences in ocean model simulations for subsequent use in satellite gravity data analysis.

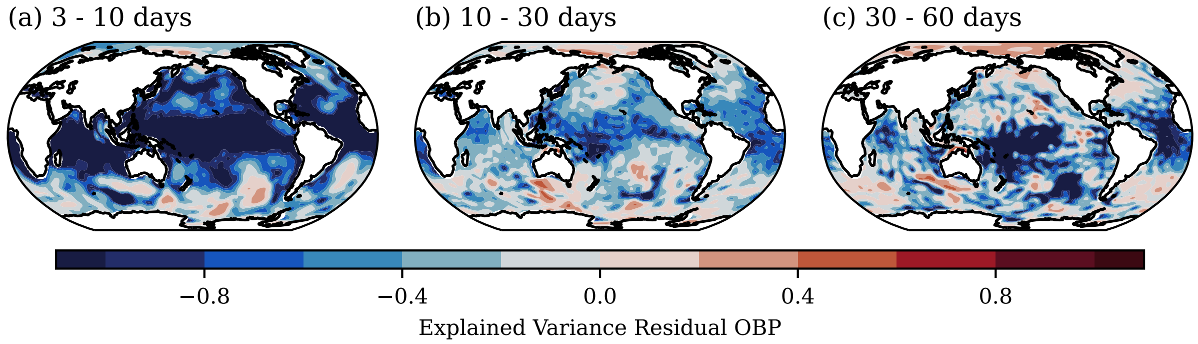

Figure 6.2: Amount of variance explained by the update of AOD1B, i.e. the difference (RL07 - RL06) using the residual circulation signal from ITSG2018 daily gravity field solutions as a base time-series. Results are bandpass filtered into 3 frequency bands: 3 – 10 days (a), 10 – 30 days (b), 30 – 60 days (c). Red indicates areas where the update of AOD1B captures more of the residual signal.

Table 6.1: Summary of atmospheric reanalysis products used in the estimation of the residual AOD1B uncertainties.

Name	Resolution	Data Assimilation	Period
ERA5	0.28×0.28, hourly	4D-VAR	1940 - present
MERRA2	0.5×0.625, hourly	3D-VAR	1980 - present
JRA55	1.25×1.25, 3-hourly	4D-VAR	1958 - present

6.2 Atmospheric surface pressure differences

AOD1B considers the non-tidal mass variations from both the oceans as well as the atmosphere. For RL07 the atmospheric component is based on the ECMWF's ERA5 reanalysis data (Hersbach et al., 2020) until 2017 followed by operational ECMWF data from 2018 onward. While the reanalysis data are constrained through observations, they will still include errors induced by insufficient or conflicting observations as well as insufficient modelling of atmospheric dynamics. These uncertainties are typically distributed globally and depend for example on parametrisations, orography, etc. and a common approach to address these is through the comparison of NWM fields published by different institutions.

We thus here compare the ERA5 surface pressure data to two other state-of-the-art atmospheric reanalyses: the Modern-Era Retrospective Analysis for Research and Applications, Version 2 (MERRA2) (Gelaro et al., 2017) from NASA's Global Modelling and Assimilation Office, and the Japanese 55-year Reanalysis (JRA55) (Kobayashi et al., 2015) from the Japan Meteorological Agency. Some characteristics regarding resolutions and data assimilation scheme are given in Tab. 6.1.

As all three reanalyses feature a different horizontal resolution, we unify all datasets by

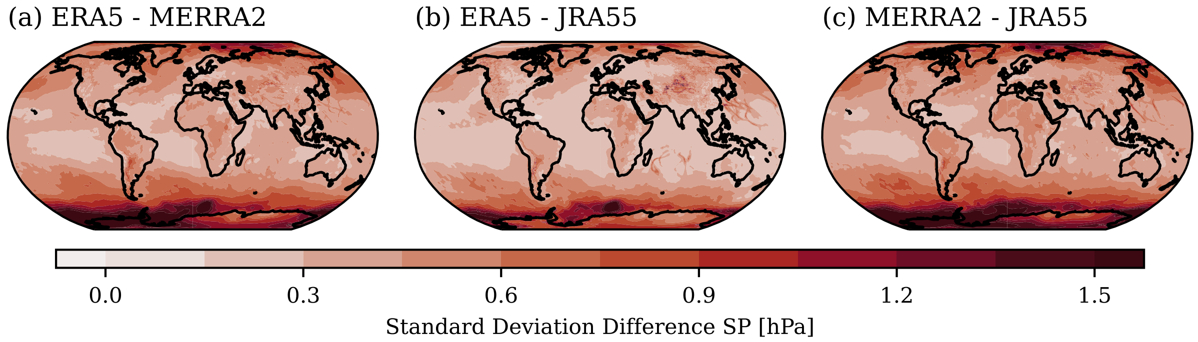

Figure 6.3: Standard deviation differences of surface pressure (SP) from three different atmospheric reanalyses. Subfigures show the results for differences between ERA5 and MERRA2 (a), ERA5 and JRA55 (b) as well as MERRA2 and JRA55 (c). All surface pressure fields are bandpass filtered using a 4th order Butterworth filter to only contain periods in the 1 – 30 days band.

remapping to a regular 0.5° grid following Dobslaw et al. (2016b), resample to a six-hourly temporal resolution and subtract the mean surface pressure in each case. This is also in line with the resolution of the previous error assessment. To eliminate the impact of low frequencies and high-frequency atmospheric tidal signals which are not part of AOD1B, we subsequently apply a bandpass filter with cutoff periods of 1 and 30 days. The results are shown in Fig. 6.3 as standard deviation differences between ERA5 & MERRA2 (a), ERA5 & JRA55 (b) and MERRA2 & JRA55 (c).

In all three cases, the largest differences in surface pressure variations are found in the Southern Ocean and Antarctica. Differences between ERA5 & MERRA2 as well as MERRA2 & JRA55 reach values of up to 2 hPa in the Ross and Weddell Seas. Over the rest of the continents, differences are much smaller and generally at or below 0.5 hPa, although the differences between ERA5 & JRA55 are the smallest. Computing area-weighted spatial averages of the absolute value gives an average difference of 0.4 hPa in the ERA5 & MERRA2 and MERRA2 & JRA55 cases. The average difference between ERA5 & JRA55 is with 0.3 hPa slightly smaller, i.e. the ERA5 and JRA55 reanalysis correspond better to each other than to the MERRA2 reanalysis. In general, however, the differences between the surface pressure data from the reanalyses are small, especially when compared to the standard deviation of just ERA5 surface pressure as given in Fig. 6.4 (a) where the surface pressure variability exceeds 10 hPa in high latitudes.

These small relative differences between the reanalyses shows that surface pressure is generally well captured by all three of them, which can be attributed to the high impact of the assimilated observational data. Only in regions where the density of observations is sparse, e.g. in Antarctica, are larger differences found. Based on the differences in the reanalyses presented in this section, we thus choose to base the atmospheric component

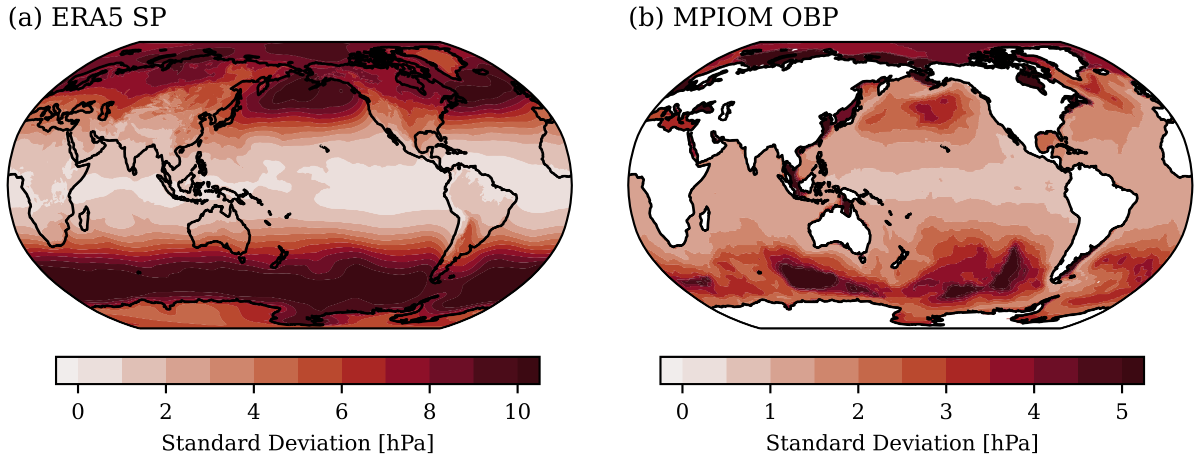

Figure 6.4: Standard deviation of ERA5 surface pressure (SP) and simulated ocean bottom pressure (OBP) from MPIOM using atmospheric ERA5 forcing data. Results are bandpass filtered using a 4th order Butterworth filter to only contain periods in the 1 – 30 days band.

of the new uncertainty estimation on the differences between ERA5 and MERRA2.

6.3 MPIOM ensemble simulations

Next to the residual uncertainties in the atmospheric component, we also consider uncertainties in the ocean domain. In contrast to the atmospheric mass variations provided by NWMs, the OBP variability is not observationally constrained. Instead, it is based on unconstrained simulations using MPIOM forced using atmospheric fields from the ERA5 reanalysis. More details on the configuration of the ocean model are given in the previous sections. Based on the lack of assimilated observations, the residual uncertainties in AOD1B RL07 are expected to be much larger compared to the atmospheric component as it was already the case for the previous estimation. To get an estimate of the residual uncertainty of the oceanic component of AOD1B we set up an ensemble simulation using MPIOM as a base model. In particular, we focus on two sources of uncertainty: the differences in the atmospheric reanalyses will result in differences in the ocean dynamics and subsequently also in differences in the OBP variability. In the following we will refer to the variability induced by the atmosphere as “forced variability”. Secondly, chaotic intrinsic variability can arise through non-linear ocean processes. While they are typically associated with smaller scales, they can map into larger variations through non-linear interactions (Arbic et al., 2012; Zhao et al., 2021). We will refer to these variations as “intrinsic variability” going forward.

6.3.1 Forced variability

Ocean dynamics are largely determined through the interaction with the atmosphere. Excluding tides, high-frequency mass variations are largely caused by surface winds leading to a redistribution of water masses. These wind-driven barotropic changes are particularly pronounced in moderate to high latitudes. Differences in atmospheric surface pressure over the oceans can also drive relevant OBP variations (Ponte, 1993). While at low frequencies the ocean surface can be expected to compensate the atmospheric pressure anomalies, at higher frequencies, surface pressure anomalies induce lateral pressure gradients and thus changes in ocean mass. While atmospheric reanalyses aim to capture the atmospheric dynamics as accurately as possible, they are of course not perfect and residual uncertainties remain as shown in the previous section. This includes presented differences in surface pressure, but also differences in other relevant atmospheric fields such as surface winds.

To assess the impact of these atmospheric differences on the MPIOM simulations, we perform three model experiments from 1995 to 2020. One is forced using atmospheric ERA5 data. This simulation is thus equivalent to the simulation used in AOD1B RL07 with the only difference being that for the simulation here we have used a 3-hourly forcing frequency in order to be consistent with the other two experiments. The second and third MPIOM runs use either the MERRA2 or the JRA55 reanalysis data for the atmospheric forcing. In both of these cases we also use 3-hourly forcing. The atmospheric forcing considers contributions from atmospheric pressure, near-surface horizontal wind speed and stresses, solar radiation, precipitation, cloud cover, temperature and dew point temperature. We extract OBP fields from the ocean model, subtract the temporal mean and bandpass filter the results using 1 and 30 day cutoff periods.

As a reference, we show the OBP variability, i.e. standard deviation, of the ERA5 forced run alone in Fig. 6.4 (b). Regions with the highest variability exceeding 5 hPa are found most prominently in the Southern Ocean in the region of the ACC, especially in the Bellingshausen Basin and the South-Australian Basin. Additionally, high variability is found in shelf areas as well as the Arctic Ocean where OBP variations are largely driven by barotropic pressure changes (Bingham and Hughes, 2008).

We now turn to the differences between the differently forced simulations. Fig. 6.5 shows the OBP standard deviation differences between the ERA5 and MERRA2 runs (a), the ERA5 and JRA55 runs (b), and the MERRA2 and JRA55 runs (c). In all three cases, the largest differences in variability match the regions that show a high variability in the first place as shown in Fig. 6.4 (b). The largest signals are found again in the Southern Ocean where the wind-driven barotropic variability is generally high but also differences in the atmospheric reanalysis data are largest (see Fig. 6.3). In these regions the OBP differences reach values of up to 1 hPa which is a significant percentage of the overall variability

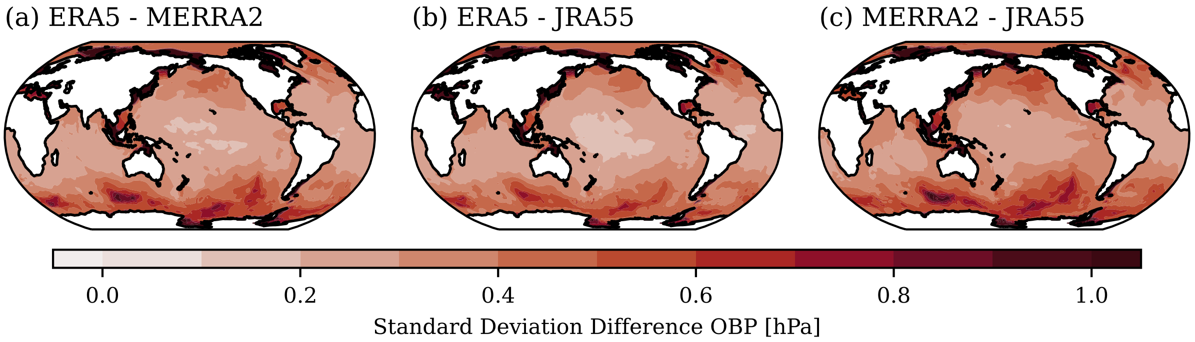

Figure 6.5: Standard deviation differences of ocean bottom pressure (OBP) from three different MPIOM simulations where the atmospheric forcing is varied. Subfigures show the results for differences between ERA5 vs. MERRA2 atmospheric forcing (a), ERA5 vs. JRA55 forcing (b) as well as MERRA2 vs. JRA55 forcing (c). All OBP fields are bandpass filtered using a 4th order Butterworth filter to only contain periods in the 1 – 30 days band.

in those places. This highlights the sensitivity of the high-frequency mass variations in the Southern Ocean to the atmospheric forcing. Comparing the individual subfigures reveals that the differences between the ERA5 and JRA55 forced runs are smaller than the difference of either to the MERRA2 forced simulation. Again, this matches the differences in atmospheric surface pressure where the differences between ERA5 and JRA55 tend to be the smallest.

6.3.2 Intrinsic variability

Next, we turn to the estimation of the contribution due to intrinsic variability in MPIOM. Oceanic intrinsic variations emerge not through variations in the atmospheric forcing but instead through mesoscale turbulence on scales of $O(10-100)$ km and $O(10-100)$ days (Sérazin et al. (2015) and references therein). The impact of this initial intrinsic variability is also found at much larger and longer (i.e. inter-annual) scales (Penduff et al., 2011), suggesting a spontaneous inverse cascade to these scales (Sérazin et al., 2018). Studies show that this intrinsic variability has a significant impact on a number of oceanic variables such as sea-level (Sérazin et al., 2015), ocean heat content (Penduff et al., 2019), transports (Cravatte et al., 2021) or OBP (Zhao et al., 2021) on various time-scales. In order to disentangle the impact of the atmospheric forcing from the intrinsic variations, a common approach is to perform parallel ocean simulations with identical forcing that only differ in some small initial perturbations. Differences in the resulting variability can then be used to examine intrinsic variations (Sérazin et al., 2015). This is the approach we use in the following as well.

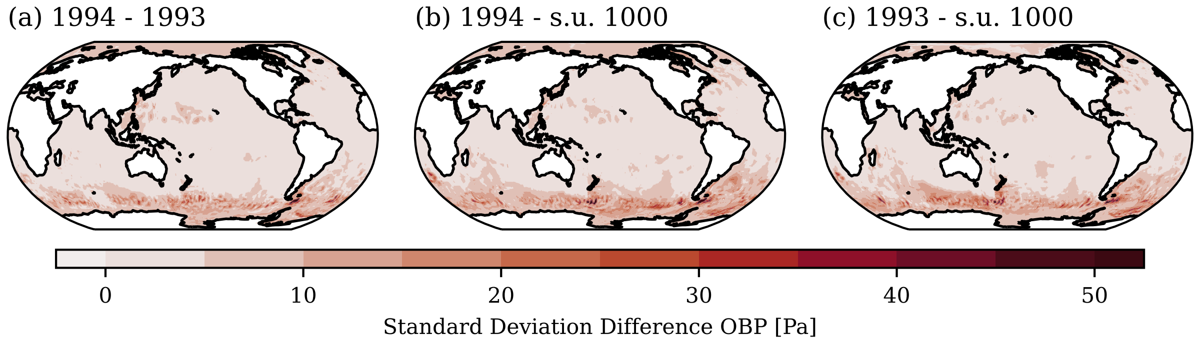

Figure 6.6: Standard deviation differences of ocean bottom pressure (OBP) from three different MPIOM simulations where the initial conditions are varied. Subfigures show the results for differences between using the correct initial conditions for 1994 vs. a one-year shift in initial conditions (a), 1994 vs. initial conditions after half of the spin-up simulation (i.e. 1000 years of spin-up) (b) as well as a one-year shift vs. using the ocean state after half of the spin-up (c). All OBP fields are bandpass filtered to only contain periods in the 1 – 30 days band.

We performed three MPIOM simulations that are all based on ERA5 atmospheric forcing data. All simulations start in the year 1994 from a transient ERA5 run started in 1960 based on a 2000 year long spin-up simulation with daily climatological forcing. One simulation, the reference, uses the "correct" initial conditions for the year 1994. For the second simulation we start the run in 1994 but employ the initial conditions based on the year 1993, thus shifting the initial state by one year. The third run uses the initial conditions after only 1000 years of the spin-up. This represents a larger difference in the initial conditions for comparison. We then compute differences in 3-hourly OBP between all three simulations and band-pass filter the results to only include frequencies in the 1 - 30 day range. The results in terms of OBP standard deviation differences are given in Fig. 6.6. Subfigure 6.6 (a) shows the difference between the reference simulation and the simulation with the initial conditions shifted by one year, whereas Fig. 6.6 (b) shows the difference between the reference and the simulation using the initial conditions after half the spin-up. The last subfigure 6.6 (c) shows the difference between the two simulations using shifted initial conditions.

The impact of the initial conditions varies strongly with latitude. Differences are largest in the Southern Ocean along the band of the ACC and reach values of up to 30 Pa. In contrast to the impact of the atmospheric forcing the differences are thus smaller by a factor of at least 3. Other regions show a very limited impact of the initial conditions. Most of the open ocean and also coastal areas are largely unaffected. Comparing the three standard deviation differences with each other shows that the spatial distribution and magnitude are very similar suggesting that the distance in time by which the initial conditions are shifted is not relevant here. As the MPIOM configuration used here and in AOD1B is not eddy-permitting, there is likely little mesoscale activity and consequently also a reduced amount of intrinsic variability (Penduff et al., 2019). This might explain why the impact of the initial conditions is comparatively small compared to the forced variability and compared to results presented by Zhao et al. (2021).

6.4 The AOe07 time-series

In the previous sections we have analysed and compared atmospheric mass variations from different state-of-the-art reanalyses which gives an estimate of the residual atmospheric uncertainty. Similarly, we have examined the oceanic uncertainty in the forced variability and intrinsic chaotic variability in MPIOM through ensemble simulations. Next, we combine the individual components to derive a single time-series of true errors representative for AOD1B RL07 that can be used in the processing of either satellite gravimetry or in simulation studies of next generation gravity missions (NGGM).

The final time-series should merge the atmospheric information over the continents with the oceanic uncertainties elsewhere. For the atmosphere we choose to use the differences between the ERA5 and the MERRA2 reanalyses. This combination is (a) compatible with AOD1B RL07 which is also based on atmospheric ERA5 data but (b) also shows the larger differences in atmospheric mass variations and is thus deemed a better estimate of the residual uncertainties. For the ocean component we combined the impact of the forced variability and the intrinsic variability in OBP. This is done through a new MPIOM simulation forced with atmospheric MERRA2 data that is also based on a shift in the initial conditions by one year. The uncertainty information over the oceans is then given by the difference between the new simulation to the reference simulation based on ERA5 data. Atmospheric tides in the surface pressure data and atmospherically induced tides in the simulated OBP are estimated and subtracted in the same way as for AOD1B RL07 and as described by Balidakis et al. (2022). The atmospheric and oceanic components as subsequently combined into a single time-series of 6-hourly fields and then high-pass filtered using a cutoff frequency of 30 days in order to only represent the high frequencies relevant for satellite gravimetry.

There is, however, an issue that needs to be addressed especially for the ocean component. As the uncertainty estimation is based on differences between OGCM simulations with MPIOM only, the uncertainties are likely underestimated in their magnitude. As indicated by Quinn and Ponte (2011), model differences, as they are used here, tend

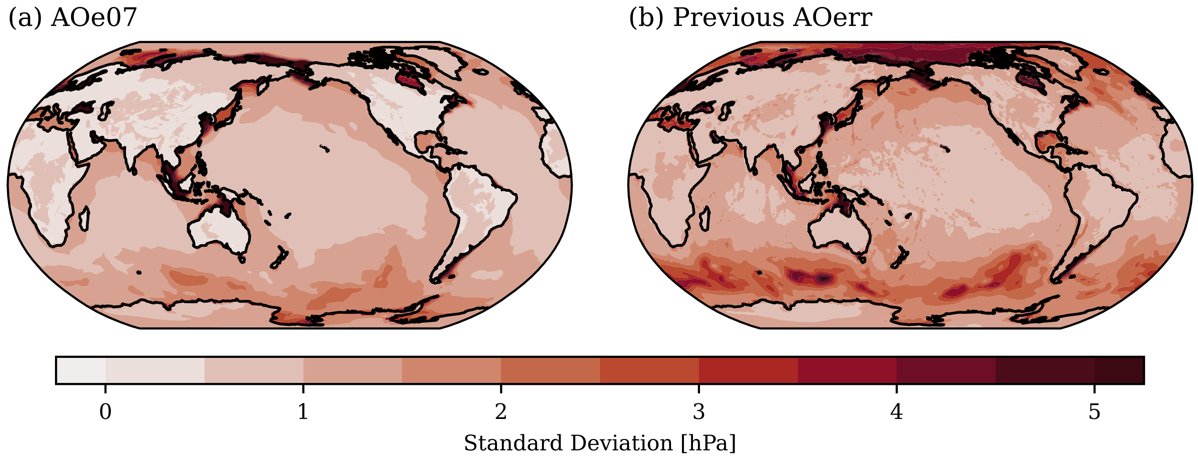

Figure 6.7: Standard deviation of the new time-series of true errors adapted for AOD1B RL07 (a) and the previous error estimation (b). In both cases 12 years from 1995 to 2006 are used.

to underestimate the high-frequency OBP variations, especially when they are based on simulations using the same ocean model. Similarly, the impact of the intrinsic variability greatly depends on the resolution of the ocean model (Sérazin et al., 2015). We here use, just as in AOD1B RL07, MPIOMs TP10L40 configuration based on a 1-degree tri-polar grid and thus expect the intrinsic variations to be under-represented in the ensemble configuration. (We anticipate that the spatio-temporal pattern of OBP variability are realistically captured but their magnitude is certainly underestimated.) Similar to the approach of the previous uncertainty estimation (Dobslaw et al., 2016b), we thus need to calculate a scaling factor for the oceanic component.

This is done through a comparison of the oceanic uncertainty estimate to the residual OBP variations in the ITSG2018 daily solutions after RL07 has been subtracted. We then select a global scaling factor to adjust the uncertainty time-series up to the ITSG variability without exceeding it. Note that the global factor of 2.4 is applied to the oceanic component of the time-series only. For the atmospheric contribution over the continents, the strong impact of the assimilated barometer data means that no scaling is required. We note, however, that this procedure does not introduce any actual GRACE or GRACE-FO gravity information from the ITSG solutions into the error time-series. This approach merely compares the overall magnitude in variability.

The thus computed final error time-series, labelled AOe07, can then be considered an estimation of the residual uncertainties in the AOD1B RL07 background model. In Fig. 6.7 we compare the standard deviation of the new AOe07 time-series (a) to the previous version (b). In both cases, the plots are based on data from the 12 years 1995 to 2006.

Globally, the new time-series features a smaller variability, reflecting the improvements

made to the AOD1B background model data over the years. The reduction is both visible over the oceans as well as over the continents. The discrepancy in the accuracy of the background model data between the atmospheric component over land and the simulated OBP is still reflected in the new time-series.
The largest uncertainties are found in the coastal areas where the amplitude of the barotropic high-frequency variations is also comparatively high. Additionally, increased uncertainties are also found in the Southern Ocean, as described in Sect. 6.3.1. Compared to the previous release, the magnitude is smaller in the Southern Ocean although the regions where the uncertainties are elevated remain similar. In contrast to the previous estimation, however, the uncertainties in the Arctic Ocean are significantly reduced which can be attributed to MPIOMs much better representation of the Arctic Ocean due to the use of a tri-polar grid.

Technically, AOe07 is available as a series of fully normalized Stokes coefficients from a spherical harmonic expansion up to d/o 180 and has a temporal resolution of six hours. The time-series covers 26 years from 1995 to 2020 and thus extends the previous version by 14 years. The data can be accessed, together with the previous uncertainty assessment, via the ESA ESM repository under *ftp://ig2-dmz.gfz-potsdam.de/ESAESM/*.

6.5 Variance-covariance matrices

One way to include the error estimation of background models is through the use of a variance-covariance matrix (VCM) which represents the spatio-temporal uncertainties. Such a VCM can then be used either in the gravity field estimation process or in dedicated simulation studies, as shown by Abrykosov et al. (2021) for the case of ocean tides. In the latter case, the approach offers an opportunity to significantly improve the gravity field retrieval performance if the non-tidal background stochastic modelling is improved as well. In this section, we derive a new VCM based on the updated AOe07 time-series that captures the spatio-temporal uncertainties of the non-tidal atmosphere and ocean high-frequency mass variations.

The calculation of the VCM is based on the computation of both variances as well as covariances between the Stokes coefficients via

$$\mathrm{cov}(X_{l_1,m_1}, X_{l_2,m_2}) = \frac{1}{N_t - 1} \sum_t (X_{l_1,m_1} - \overline{X}_{l_1,m_1}) \cdot (X_{l_2,m_2} - \overline{X}_{l_2,m_2}) \tag{6.2}$$

where X_{l_1,m_1} stands for the C and S Stokes coefficients of degree l_1 and order m_1 while $\overline{X}$ represents the temporal mean value. Variances are computed analogously using $l_1 = l_2$

and $m_1 = m_2$.

Based on Eq. 6.2, a fully populated stationary VCM is calculated up to d/o 40. This then matches the resolution of current GRACE daily solutions such as ITSG2018. Additionally, a second diagonal matrix, containing thus only variances, is calculated up to the full d/o 180. Like the AOe07 time-series, both matrices are publicly available under Shihora et al. (2023a).
In the following, we will turn to possible applications in GRACE-like and NGGM simulations.

6.6 Application in simulation studies

In the context of satellite gravimetry, the background model uncertainties (as given by AOe07) can be applied in a variety of ways. Specifically in the context of the current GRACE and GRACE-FO data processing, AOe07 can be applied in the gravity field estimation process to weight observations according to the uncertainty of the associated background model information. Secondly, the data set can be used in dedicated satellite gravimetry simulation studies. Especially the estimation of gravity field retrieval errors is regularly performed in the context of future gravity mission scenarios and their comparison. Here we present an example application of AOe07 in GRACE-FO-like simulations similar to Flechtner et al. (2016).

We performed a GRACE-FO baseline simulation for the year 2002 using the ESA Earth-System Model (ESA ESM) as a time-variable source model and GFZs EPOS-OC software (Zhu et al., 2004). For the recovery, the background model that represents the non-tidal atmospheric and oceanic variations is based on the so called DEAL coefficients (Dobslaw et al., 2016b), perturbed by the uncertainty information. We performed two gravity field recoveries using either the previous uncertainty estimation AOerr or the new dataset AOe07 as the source for those perturbations. Finally, gravity field retrieval errors were computed by subtracting the HIS component (i.e. terrestrially stored water, continental ice-sheets and solid Earth) of the ESA ESM from the recovered gravity field. This is done once considering only the noise contribution from the atmosphere and ocean (AO) and once in a full-noise scenario which additionally considers the noise in other background models as well as non-gravitational contributions to the noise. We note, that since the DEAL + AO error coefficients are used in the recovery, the results also include the aliasing error due to the HIS components. However, since these are identical in the AOerr and AOe07 recoveries, this does not impact the interpretation of the results.

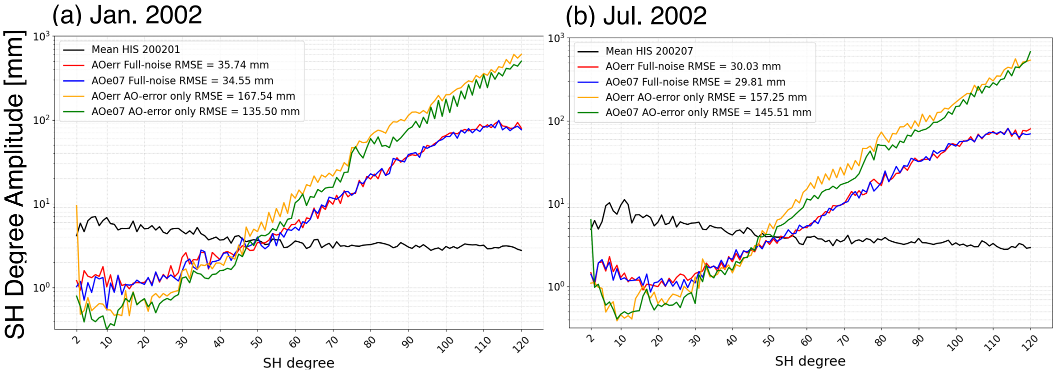

Figure 6.8: Simulated degree amplitudes of gravity retrieval errors in mm EWH considering either AO noise only or a full noise scenario. In the AO-noise only case, the new AOe07 is given in green and the previous AOerr in yellow. The full noise simulation results are in blue for AOe07 and red for AOerr. The mean HIS signal is given in black and RMSE values are given in the legend. Results are shown for Jan. and Jul. of 2002.

Results shown in Fig. 6.8 indicate the gravity field retrieval error for the new AOe07 error time-series (green and blue) in comparison to the previous AOerr time-series (yellow and red). The mean HIS signal is given in black as indicator for the actual geophysical signal that needs to be captured by a satellite mission. Considering the AO error only, the simulation results indicate an overall reduction in the retrieval error of a few mm EWH, which we consider as relevant for single-pair missions. For the two months shown here, the RMSE is reduced by about 30 and 12 mm. While some reduction is also seen in parts at low degrees, the reduction is best visible for degrees above about d/o 30 and as a result, the mean HIS signal is recoverable to slightly higher spatial resolution. While there are slight variations from month to month, the results are fairly consistent for all computed months of the year 2002, indicating that when AO errors are considered, the simulated gravity retrieval error is reduced using the new AOe07 error estimation. Most likely, this can be attributed to the overall reduced amplitude of the new error time-series compared to its predecessor. In the full-noise simulation, the results remain qualitatively similar, i.e. the gravity field error is reduced when considering the new AOe07 time-series, the improvement is, however, much smaller with a reduction in the RMSE of 1.2 and 0.2 mm. Most likely this is due to the dominance of other contributions to the overall noise level.

In consequence, error budget assessments for future missions are recommended to be based on AOe07 instead of AOerr in order to properly account for the most recent developments in AOD1B background modelling.

6.7 Summary and conclusions

This section has described and examined a new estimation of the remaining uncertainties in the latest release 07 of the AOD1B product. The newly updated uncertainty estimation is called AOe07 and can be used both for the processing of monthly gravity field solutions for mitigating the impact of residual temporal aliasing, as well as for dedicated simulation studies of future satellite gravimetry mission concepts.

We have shown that the new release of AOD1B does indeed improve the representation of the oceanic high frequency variability by comparing both RL07 and RL06 to the daily ITSG2018 gravity field solutions in regions where ITSG displays a significant amount of variability. Considering that the represented variability of AOD1B is less accurate over the oceans compared to the atmospheric contribution over land (Shihora et al., 2023b), an update of the residual uncertainty estimation was deemed necessary.

The new estimation is based on model inter-comparisons both for the atmosphere and the ocean. For the atmospheric part we rest the estimation on model differences between the latest ECMWF reanalysis ERA5, which is the basis of AOD1B RL07, and the MERRA2 reanalysis. Over the oceans, we calculate model differences between unconstrained MPIOM simulations forced with ERA5 and MERRA2, whereas the latter also includes shifted initial conditions in order to capture the impact of the intrinsic variability. The final AOe07 time-series then combines the atmospheric contributions over land and the oceanic contributions into a single 6-hourly time-series of Stokes coefficients up to d/o 180.

As, however, the oceanic component is based on model differences from the same ocean model, the uncertainties are most likely underestimated. Similar to the previous release by Dobslaw et al. (2016b), this issue has been addressed through a time-invariant global scaling factor that is applied to the entire oceanic domain. The scaling factor is determined based on a comparison of the model differences to the residual variability in the daily ITSG data. While this is not an ideal approach, large parts of the spatio-temporal pattern of the OBP variability and the overall magnitude are fairly well captured. However, we note that the ratio of intrinsic versus forced variability is smaller than in comparable studies (Zhao et al., 2021). We attribute this to the limited spatial resolution of the MPIOM configuration, which does not resolve mesoscale processes which are the ultimate driver of the intrinsic variability. It is believed that, given the ongoing progress towards the next generation of satellite gravimetry missions and the associated studies, the timely availability of applicable background model uncertainties is important, so that AOe07 has been published despite that obvious weakness. In a possible future refinement, additional investigations that specifically address the impact of the ocean model resolution as well as exploring differences based on different ocean models including high-resolution shallow-water codes should be considered. In that way, an even more realistic uncertainty estimate could be provided.

Based on the AOe07 time-series, a variance-covariance matrix that represents explicitly the (time-averaged) spatial correlations for further use in simulation studies is also provided. A successful example of the application of VCMs is given in Abrykosov et al. (2021) for the case of ocean tides. Lastly, we have demonstrated the application of the new dataset in an exemplary single-pair satellite gravimetry simulation. The results, which compare the gravity field retrieval error when using either the new AOe07 data or the previous error estimation, show a general improvement in the monthly retrieval by several mm EWH, especially at higher degrees, and thus demonstrate a better signal recovery by a few degrees. While the example given here is based on a single-pair simulation, AOe07 is also intended to serve as a basis for future gravity mission simulation studies. To that end, it is recommended that simulation studies are based on the ESA ESM DEAL coefficients in combination with AOe07 to arrive at a realistically perturbed de-aliasing model that is compatible with recent developments in background models.

7

Summary and outlook

This dissertation presents the development, production and first assessment of a new Atmosphere and Ocean dealiasing Level-1B product RL07. The AOD1B product is vital in the processing of satellite gravimetry measurements, as it provides a-priori information on the high-frequency mass variations in the atmosphere and ocean that, if unaccounted for, would induce temporal aliasing artefacts in the final gravity field solutions from GRACE and GRACE-FO. In addition, it is applied in the analysis and interpretation of the gravity field solutions, as it aids in the separation of mass variations in the vertical direction since satellite gravimetry is inherently incapable of distinguishing between e.g. mass variations in the atmosphere or at the Earth's surface. As these kinds of background models are always an imperfect representation of the real world, residual errors in the final gravity field solutions due to temporal aliasing remain. In the case of the GRACE measurements, the errors due to imperfect de-aliasing are even among the largest contributions to the overall GRACE error. As a result, improvements in the applied background models offer a chance to greatly improve the quality of the GRACE measurements and thus directly impact the wide array of applications that rely on the measurements.

As a fist step towards a new release of AOD1B, we have focused on improvements of the ocean model MPIOM that is used for AOD1B to include feedbacks from self-attraction and loading. At high frequencies, mass anomalies in the ocean will induce a gravitational attraction of the surrounding water masses and at the same time cause a deformation of the solid Earth. Both of those effects change horizontal pressure gradients that cause secondary ocean currents to occur. While the importance of SAL has been well established for tidal dynamics, its impact on the non-tidal ocean dynamics has received far less attention. The first part of this thesis presents the results of implementing SAL into both a barotropic ocean tide model (TiME) as well as the baroclinic OGCM MPIOM to study the impact on both ocean tides as well as the general circulation. In the case of the M_2 tidal constituent, as simulated using the TiME ocean model, including the feedbacks from SAL reduces the tide-gauge RMS by about 82%. While the impact is smaller for longer frequencies, the inclusion of SAL is vital there as well. The impact on the general circulation, as simulated with MPIOM, is similarly significant. Including SAL in a non-tidal simulation results in a difference of up to 1 hPa especially in coastal areas. In the Southern Ocean, differences of up to 0.5 hPa are found in particular resonant basins in the region of the Antarctic Circumpolar Current. These findings, combined with studies of the previous release of AOD1B (RL06) which does not include any SAL feedback, suggest that including SAL in the ocean model has a significant impact on the accuracy of the high-frequency non-tidal mass variations in the ocean and should thus be included in a new release of AOD1B.

The improvements due to the inclusion of SAL together with an update to the ocean model configuration, newly released atmospheric reanalysis data and an updated processing scheme form the changes made to AOD1B for the new release RL07. Section 4 compiles the changes that have been made for the new release. In addition it includes comparisons to the previous release RL06 by using actual GRACE-FO KBR and LRI data as well as altimetry measurements. All of these comparisons to the previous release RL06 show an overall improvement in the representation in the non-tidal high-frequency mass variations. Most notably are improvements in the Southern Ocean, the region of the Antarctic Circumpolar Current, as well as some shelf regions such as the Gulf of Carpentaria or around Indonesia. As the Southern Ocean is the region with the largest high-frequency variability in the ocean due to the impact of strong surface winds, changes in the atmospheric forcing as well as the feedbacks from self-attraction and loading have a notable effect here. Similarly, the variability in the coastal regions is typically characterized by mass variations on daily or even sub-daily time-scales. As a result, the higher temporal resolution of the atmospheric forcing again in combination with the feedbacks from self-attraction and loading have a strong impact. Especially the improvements in the Gulf of Carpentaria were also the focus of the detailed study by Ghobadi-Far et al. (2022) which found a significantly better representation of the mass variations in that region during a tropical cyclone using instantaneous GRACE-FO line-of-sight gravity differences.

The accurate representation of atmospheric and oceanic mass variations is, however, not the only requirement of AOD1B, which is why we also assessed the stability of the dataset. Residual long-term trends in AOD1B can, when used as a background model in the processing of satellite gravimetry, introduce these trends into the final gravity solutions. The induced trends are then prone to be analysed and interpreted in an entirely different geophysical context and thus degrade the reliability of the satellite gravimetry measurements for applications. In addition, short term inconsistencies such as bias jumps, can negatively affect the gravity inversion process and thus degrade the individual gravity field solutions. This is especially important for the switch in the employed atmospheric data in AOD1B in the beginning of 2018. As this change coincides with the measurement gap between GRACE and its successor GRACE-FO, any inconsistency across that transition in AOD1B would negatively impact the continuity of the entire gravity field time-series. The analysis of linear trends shows that they are comparable to previous releases of AOD1B and, in the case of the atmospheric component, comparable to other state-of-the-art reanalyses. While the residual trends are at an acceptable level given the current accuracy of GRACE-based trend estimates such as by Rodell et al. (2018) or Loomis et al. (2021), efforts should be made for a further reduction in the future to account for the higher accuracies of future satellite gravimetry missions. Assessing possible inconsistencies in RL07 shows no indication of problematic behaviour such as bias jumps. While changes induced by the switch in atmospheric forcing are visible by computing 3-hourly tendencies, the impact is gradual and to be expected given the change in resolution. An impact due to updates in ECMWFs Integrated Forecast System, which is the basis for the operational ECMWF data, was, however, not identified. Nonetheless, the 3-hourly tendencies must be monitored also during the operational production of AOD1B, in order to catch any inconsistencies that might arise in the future.

While AOD1B RL07 improves the de-aliasing of satellite gravimetry data due to a better representation of high-frequency mass variations in atmosphere and oceans, background models are inherently imperfect and thus residual errors due to temporal aliasing will remain. These residual errors can be further reduced by considering information on the uncertainty of the background models in the gravity field estimation process. This has been used for previous releases of AOD1B by Kvas and Mayer-Gürr (2019) and has also been shown for ocean tide background model errors by Abrykosov et al. (2021). While previous estimates of the uncertainties in AOD1B exist, they are based on AOD1B RL05 and thus deemed not applicable to the new release RL07 given the changes made to the new release as highlighted above. We therefore developed a new time-series of true errors, labelled AOe07, that is compatible with AOD1B RL07 and can be used in the gravity field inversion process as well as simulation studies. The product is based on model inter-comparisons for both the atmospheric and the oceanic components separately. The resulting data shows, compared to its predecessor AOerr, a reduced variability and thus represents a reduction in the background model uncertainties which is in line with the improvements made to AOD1B and which is also captured in the reduced simulated gravity field retrieval errors. While there are certainly some elements of the oceanic uncertainty that are not perfectly captured, given the ongoing progress towards the next generation of satellite gravimetry missions and the associated studies, the timely availability of applicable background model uncertainties is especially important. Nevertheless, there might be the need for a more detailed and comprehensive analysis in the future.

All of the work presented here allows for better mitigation of temporal aliasing effects in GRACE and GRACE-FO gravity field data and will consequently contribute to a higher quality of the final monthly gravity field solutions and thus accomplishes the initial goal of this work as presented in the beginning. This is especially timely due to the ongoing work towards a reprocessing of the GRACE time-series. But also on longer time-scales, these changes can be a first step to further improve the quality of satellite gravimetry measurements. Especially as background models for satellite gravimetry will continue to play an important role for future missions. While the nominal mission lifetime of GRACE-FO ends in 2023, it is planned to continue until about 2028 (Wiese et al., 2022) depending on the solar activity in the coming years and continuous concerns about fuel leaks on GF2. Due to two single points of failure on the satellites, the end of the mission could, however, also be much sooner. As one of the major objectives for future satellite gravimetry missions is the continuity of the time-series without any gaps, work towards these new missions is ongoing (Wiese et al., 2022; Haagmans and Tsaoussi, 2020; Massotti et al., 2021). Initial funding has been approved both by the German government, NASA as well as by the ESA Council in 2023. Naturally, work towards future gravity missions also extends to improvements in the quality of the observations. This includes especially satellite constellations featuring more than one pair of satellites, such as described by Wiese et al. (2022) and Massotti et al. (2021) which can, in theory, allow the inversion of a gravity field solution with shorter accumulation periods and thus reduce the impact of temporal aliasing. However, even if multiple satellite pairs are combined, such as in the currently favoured Bender-constellation (Bender and Nerem, 2008), mass variations at the highest frequencies will still not be able to be resolved through the measurement data alone. Thus, background models that offer a-priori information on the high-frequency mass variations will still be required and need to be improved even further. In summary, the developments presented in this thesis, while having a positive impact on the gravity field processing, will need to be continued in the future to further improve AOD1Bs representation of mass variations in the atmosphere and oceans.

As described earlier, most of the sub-monthly oceanic mass variations, which are driven by atmospheric forcing through surface winds and pressure differences, are barotropic. As such, they might adequately be captured by an ocean model based on the shallow water equations if the primary interest is in the high-frequency variability (Bingham and Hughes, 2008). Given that these models are computationally less demanding this would open the door to changes in the ocean model configuration such as increases in the spatial resolution which would be especially important in e.g. coastal and shelf-areas or for the proper representation of semi-enclosed seas which are often poorly represented at coarse resolutions. However, the degree to which all high-frequency mass variations can be captured by such a configuration will certainly require detailed analysis and comparisons to other models and observations. Secondly, background models and their applications in satellite gravimetry so far assume that tidal and non-tidal mass variations are independent from each other. While to a first approximation this might be true, there are certainly interactions which are currently not captured by background models.

Tidal and non-tidal simulations typically have different requirements. While it is already possible to perform combined forward simulations, the results, especially for the tidal signals, can not compete with the current accuracy of partial-tide simulations. However, given the recent progress in tidal forward simulations (see for example Sulzbach et al. (2021)) this gap has gotten smaller. Combined simulations with an appropriate accuracy might now be reachable and work towards that goal is ongoing (e.g. Barton et al. (2022)). In addition, even if a proper representation of the interaction of both types of ocean dynamics is not yet possible, an estimation of the error that is made by neglecting it can be a valuable first step and might be included in future uncertainty estimations.

With regards to uncertainty assessments, the work on AOe07 as presented here is not completely exhaustive. There is an additional benefit to a more detailed study of the uncertainties in the background models, namely by extending the model inter-comparisons to include different ocean model configurations and resolutions as well as even different ocean models such as those based on the shallow-water equations. Lastly, given the ongoing development of next generation gravity missions, requirements of the spatial or temporal resolutions of the background models might change over the next years. In general, these very coarsely sketched possible paths forward offer the opportunity to improve background modelling far into the future in parallel with the improvements in the observation system, such that important changes in the Earths system can be captured with even greater accuracy.

Lastly, there is also an additional application of the presented work outside of satellite gravimetry. The developed MPIOM configuration will also be used in the calculations of non-tidal oceanic surface loading deformations (Dill and Dobslaw, 2013) and oceanic angular momentum functions (Dobslaw and Dill, 2018) as they are routinely provided by the GFZ. Mass transports from the described simulations have been saved as well so that they can be used in earth orientation parameter prediction and the simulations can thus be of benefit to a wider geodetic community. Finally, the described implementation of the full feedbacks of SAL in MPIOM has been made available to the Max-Planck-Institute for Meteorology so that it may be included in the main branch of the MPIOM model and possibly also the newly developed OGCM ICON-O (Korn et al., 2022) in the future. That way, the implementation may be of use to the wider oceanographic community.

List of Figures

List of Tables

Nomenclature

ACC	Antarctic circumpolar current
AMOC	Atlantic meridional overturning circulation
AOD1B	Atmosphere and Ocean De-Aliasing Level-1B product
AOe07	Atmosphere and ocean uncertainty estimation adapted to AOD1B RL07
DAC	Dynamic atmospheric corrections
ECMWF	European Centre for Medium-Range Weather Forecasts
ERA5	ECMWF Re-Analysis 5
EWH	Equivalent water height
FES14	Finite element solution global ocean tidal atlas 2014
GFZ	Deutsches GeoForschungsZentrum
GIA	Glacial isostatic adjustment
GRACE	Gravity Recovery and Climate Experiment
GRACE-ACC	GRACE accelerometer
GRACE-FO	Gravity Recovery and Climate Experiment Follow-On
GRD	Gravity, rotation and deformation
HIS	Hydrology, ice-Sheets, solid Earth
HOPE	Hamburg Ocean Primitive Equation Model
IFS	Integrated forecast system
ILRS	International Laser Ranging Service
ITRF2020	International Terrestrial Reference Frame 2020
ITSG	Institute of Geodesy at Graz University of Technology
JPL	Jet Propulsion Laboratory

JRA55	Japanese 55-year Reanalysis
KBR	K-band ranging instrument
KBRA	K-band range-acceleration
LEO	Low Earth orbit
LGD	Line-of-sight gravity difference
LRI	Laser ranging interferometer
MERRA2	Modern-Era Retrospective analysis for Research and Applications, Version 2
MPIOM	Max-Planck-Institute for Meteorology Ocean Model
NGGM	Next generation gravity mission
NWP	Numerical weather prediction model
OBA	Ocean bottom pressure anomalies
OBP	Ocean bottom pressure
OGCM	Ocean general circulation model
PVE	Percent of explained variance
RMS	Root-mean square
RMSE	Root-mean square error
SAL	Self-attraction and loading
SDS	GRACE science data system
SH	Spherical harmonics
SLR	Satellite laser ranging
SP	Surface pressure
TiME	Tidal Model forced by Ephemerides
TWS	Terrestrial water storage
VCM	Variance-covariance matrix

Bibliography

Abich, K., Abramovici, A., Amparan, B., Baatzsch, A., Okihiro, B. B., Barr, D. C., Bize, M. P., Bogan, C., Braxmaier, C., Burke, M. J., Clark, K. C., Dahl, C., Dahl, K., Danzmann, K., Davis, M. A., de Vine, G., Dickson, J. A., Dubovitsky, S., Eckardt, A., Ester, T., Barranco, G. F., Flatscher, R., Flechtner, F., Folkner, W. M., Francis, S., Gilbert, M. S., Gilles, F., Gohlke, M., Grossard, N., Guenther, B., Hager, P., Hauden, J., Heine, F., Heinzel, G., Herding, M., Hinz, M., Howell, J., Katsumura, M., Kaufer, M., Klipstein, W., Koch, A., Kruger, M., Larsen, K., Lebeda, A., Lebeda, A., Leikert, T., Liebe, C. C., Liu, J., Lobmeyer, L., Mahrdt, C., Mangoldt, T., McKenzie, K., Misfeldt, M., Morton, P. R., Müller, V., Murray, A. T., Nguyen, D. J., Nicklaus, K., Pierce, R., Ravich, J. A., Reavis, G., Reiche, J., Sanjuan, J., Schütze, D., Seiter, C., Shaddock, D., Sheard, B., Sileo, M., Spero, R., Spiers, G., Stede, G., Stephens, M., Sutton, A., Trinh, J., Voss, K., Wang, D., Wang, R. T., Ware, B., Wegener, H., Windisch, S., Woodruff, C., Zender, B., and Zimmermann, M. (2019). In-Orbit Performance of the GRACE Follow-on Laser Ranging Interferometer. *Phys. Rev. Lett.*, 123:031101.

Abramowitz, M. and Stegun, I. A. (1972). *Handbook of Mathematical Functions.* U.S. Dep. of Comm., Washington D. C.

Abrykosov, P., Sulzbach, R., Pail, R., Dobslaw, H., and Thomas, M. (2021). Treatment of ocean tide background model errors in the context of GRACE/GRACE-FO data processing. *Geophysical Journal International*, 228(3):1850–1865.

Accad, Y. and Pekeris, C. L. (1978). Solution of the Tidal Equations for the M_2 and S_2 Tides in the World Oceans from a Knowledge of the Tidal Potential Alone. *Philosophical Transactions of the Royal Society of London Series A*, 290(1368):235–266.

Arbic, B. K., Scott, R. B., Flierl, G. R., Morten, A. J., Richman, J. G., and Shriver, J. F. (2012). Nonlinear Cascades of Surface Oceanic Geostrophic Kinetic Energy in the Frequency Domain. *Journal of Physical Oceanography*, 42(9):1577 – 1600.

Arendt, A., Luthcke, S., Gardner, A., O'Neel, S., Hill, D., Moholdt, G., and Abdalati, W. (2013). Analysis of a GRACE global mascon solution for Gulf of Alaska glaciers. *Journal of Glaciology*, 59(217):913–924.

Backhaus, J. O. (1985). A Three-Dimensional Model for the Simulation of Shelf Sea Dynamics. *Dtsch. Hydrol. Zeitung*, 4:165–186.

Balidakis, K., Sulzbach, R., Shihora, L., Dahle, C., Dill, R., and Dobslaw, H. (2022). Atmospheric Contributions to Global Ocean Tides for Satellite Gravimetry. *Journal of Advances in Modeling Earth Systems*, 14(11).

Barton, K. N., Pal, N., Brus, S. R., Petersen, M. R., Arbic, B. K., Engwirda, D., Roberts, A. F., Westerink, J. J., Wirasaet, D., and Schindelegger, M. (2022). Global barotropic tide modeling using inline self-attraction and loading in MPAS-Ocean. *Journal of Advances in Modeling Earth Systems*.

Behzadpour, S., Mayer-Gürr, T., and Krauss, S. (2021). GRACE Follow-On Accelerometer Data Recovery. *Journal of Geophysical Research: Solid Earth*, 126(5):e2020JB021297.

Bell, B., Hersbach, H., Simmons, A., Berrisford, P., Dahlgren, P., Horányi, A., Muñoz-Sabater, J., Nicolas, J., Radu, R., Schepers, D., Soci, C., Villaume, S., Bidlot, J.-R., Haimberger, L., Woollen, J., Buontempo, C., and Thépaut, J.-N. (2021). The ERA5 global reanalysis: Preliminary extension to 1950. *Quarterly Journal of the Royal Meteorological Society*, 147(741):4186–4227.

Bender, P.L., W.-D. and Nerem, R. (2008). A Possible Dual-GRACE Mission with 90 Degree and 63 Degree Inclination Orbits. *Proceedings of the 3rd International Symposium on Formation Flying, Missions and Technologies, ESA/ESTEC, Noordwijk*, pages 1–6.

Bergmann, I. and Dobslaw, H. (2012). Short-term transport variability of the Antarctic Circumpolar Current from satellite gravity observations. *Journal of Geophysical Research: Oceans*, 117(C5).

Bernales, J., Rogozhina, I., and Thomas, M. (2017). Melting and freezing under Antarctic ice shelves from a combination of ice-sheet modelling and observations. *Journal of Glaciology*, 63(240):731–744.

Bingham, R. J. and Hughes, C. W. (2008). The relationship between sea-level and bottom pressure variability in an eddy permitting ocean model. *Geophysical Research Letters*, 35(3):L03602.

Blazquez, A., Meyssignac, B., Lemoine, J., Berthier, E., Ribes, A., and Cazenave, A. (2018). Exploring the uncertainty in GRACE estimates of the mass redistributions at the Earth surface: implications for the global water and sea level budgets. *Geophysical Journal International*, 215(1):415–430.

Boergens, E., Güntner, A., Dobslaw, H., and Dahle, C. (2020). Quantifying the Central European Droughts in 2018 and 2019 With GRACE Follow-On. *Geophysical Research Letters*, 47(14).

Bonin, J. A. and Chambers, D. P. (2011). Evaluation of high-frequency oceanographic signal in GRACE data: Implications for de-aliasing. *Geophysical Research Letters*, 38(17).

Bonin, J. A. and Save, H. (2020). Evaluation of sub-monthly oceanographic signal in GRACE “daily” swath series using altimetry. *Ocean Science*, 16(2):423–434.

Bonin, J. A. and Save, H. (2021). Using GRACE to improve altimetry’s ocean de-aliasing model. *Journal of Geophysical Research: Oceans*, page e2021JC017711.

Carrere, L., Faugère, Y., and Ablain, M. (2016). Major improvement of altimetry sea level estimations using pressure-derived corrections based on era-interim atmospheric reanalysis. *Ocean Science*, 12(3):825–842.

Carrere, L. and Lyard, F. (2003). Modeling the barotropic response of the global ocean to atmospheric wind and pressure forcing - comparisons with observations. *Geophysical Research Letters*, 30(6).

Cesare, S., Allasio, A., Anselmi, A., Dionisio, S., Mottini, S., Parisch, M., Massotti, L., and Silvestrin, P. (2016). The European way to gravimetry: From GOCE to NGGM. *Advances in Space Research*, 57(4):1047–1064.

Chambers, D. P., Wahr, J., Tamisiea, M. E., and Nerem, R. S. (2010). Ocean mass from GRACE and glacial isostatic adjustment. *Journal of Geophysical Research: Solid Earth*, 115(B11).

Chen, J., Cazenave, A., Dahle, C., Llovel, W., Panet, I., Pfeffer, J., and Moreira, L. (2022). Applications and Challenges of GRACE and GRACE Follow-On Satellite Gravimetry. *Surveys in Geophysics*, 43(1):305–345.

Chen, J., Tapley, B., Save, H., Tamisiea, M. E., Bettadpur, S., and Ries, J. (2018). Quantification of Ocean Mass Change Using Gravity Recovery and Climate Experiment, Satellite Altimeter, and Argo Floats Observations. *Journal of Geophysical Research: Solid Earth*, 123(11):10,212–10,225.

Chen, J. L., Wilson, C. R., and Seo, K.-W. (2006). Optimized smoothing of Gravity Recovery and Climate Experiment (GRACE) time-variable gravity observations. *Journal of Geophysical Research: Solid Earth*, 111(B6).

Cravatte, S., Serazin, G., Penduff, T., and Menkes, C. (2021). Imprint of chaotic ocean variability on transports in the southwestern Pacific at interannual timescales. *Ocean Science*, 17(2):487–507.

Cushman-Roisin, B. and Beckers, J.-M. (2011). *Introduction to Geophysical Fluid Dynamics - Physical and Numerical Aspects*, volume 101. Academic Press.

Dahle, C., Flechtner, F., Murböck, M., Michalak, G., Neumayer, K. H., Abrykosov, O., Reinhold, A., and König, R. (2019a). GRACE-FO Geopotential GSM Coefficients GFZ RL06 (Level-2B Product). V. 0002.

Dahle, C., Murböck, M., Flechtner, F., Dobslaw, H., Michalak, G., Neumayer, K., Abrykosov, O., Reinhold, A., König, R., Sulzbach, R., and Förste, C. (2019b). The GFZ GRACE RL06 Monthly Gravity Field Time Series: Processing Details and Quality Assessment. *Remote Sensing*, 11(18):2116.

Dieminger, W., Hartmann, G. K., and Leitinger, R. (1996). Atmospheric Tides. pages 97–109. Springer Berlin Heidelberg.

Dill, R. and Dobslaw, H. (2013). Numerical simulations of global-scale high-resolution hydrological crustal deformations. *Journal of Geophysical Research: Solid Earth*, 118(9):5008–5017.

Dobslaw, H. (2016). Homogenizing surface pressure time-series from operational numerical weather prediction models for geodetic applications. *Journal of Geodetic Science*, 6(1).

Dobslaw, H., Bergmann-Wolf, I., Dill, R., Poropat, L., and Flechtner, F. (2016a). Product Description Document for AOD1B Release 06, Rev. 6.0. *GFZ Potsdam, Potsdam, Germany.* Available at: ftp://isdcftp.gfz-potsdam.de/grace/DOCUMENTS/Level-1/GRACE_AOD1B_Product_Description_Document_for_RL06.pdf.

Dobslaw, H., Bergmann-Wolf, I., Dill, R., Poropat, L., Thomas, M., Dahle, C., Esselborn, S., König, R., and Flechtner, F. (2017). A new high-resolution model of non-tidal atmosphere and ocean mass variability for de-aliasing of satellite gravity observations: AOD1B RL06. *Geophysical Journal International*, 211(1):263–269.

Dobslaw, H., Bergmann-Wolf, I., Forootan, E., Dahle, C., Mayer-Gürr, T., Kusche, J., and Flechtner, F. (2016b). Modeling of present-day atmosphere and ocean non-tidal de-aliasing errors for future gravity mission simulations. *Journal of Geodesy*, 90(5):423–436.

Dobslaw, H. and Dill, R. (2018). Predicting earth orientation changes from global forecasts of atmosphere-hydrosphere dynamics. *Advances in Space Research*, 61(4):1047–1054.

Dobslaw, H., Dill, R., Bagge, M., Klemann, V., Boergens, E., Thomas, M., Dahle, C., and Flechtner, F. (2020). Gravitationally Consistent Mean Barystatic Sea Level Rise From Leakage-Corrected Monthly GRACE Data. *Journal of Geophysical Research: Solid Earth*, 125(11):e2020JB020923.

Dobslaw, H., Dill, R., Grötzsch, A., Brzeziński, A., and Thomas, M. (2010). Seasonal polar motion excitation from numerical models of atmosphere, ocean, and continental hydrosphere. *Journal of Geophysical Research: Solid Earth*, 115(B10).

Dobslaw, H. and Thomas, M. (2005). Atmospheric induced oceanic tides from ECMWF forecasts. *Geophysical Research Letters*, 32(10).

Doodson, A. T. (1921). The Harmonic Development of the Tide-Generating Potential. *Proc. R. Soc. London*, 100:305–329.

Drijfhout, S., Heinze, C., Latif, M., and Maier-Reimer, E. (1996). Mean Circulation and Internal Variability in an Ocean Primitive Equation Model. *Journal of Physical Oceanography*, 26(4):559–580.

Eicker, A., Jensen, L., Wöhnke, V., Dobslaw, H., Kvas, A., Mayer-Gürr, T., and Dill, R. (2020). Daily GRACE satellite data evaluate short-term hydro-meteorological fluxes from global atmospheric reanalyses. *Scientific Reports*, 10(1):4504.

Fagiolini, E., Flechtner, F., Horwath, M., and Dobslaw, H. (2015). Correction of inconsistencies in ECMWF's operational analysis data during de-aliasing of GRACE gravity models. *Geophysical Journal International*, 202(3):2150–2158.

Farell, W. E. (1973). Earth tides, Ocean Tides and Tidal Loading. *Philos. Trans. R. Soc. London. Ser. A*, 274:253–259.

Farrell, W. E. (1972). Deformation of the Earth by surface loads. *Reviews of Geophysics*, 10(3):761–797.

Farrell, W. E. and Clark, J. A. (1976). On postglacial sea level. *Geophysical Journal of the Royal Astronomical Society*, 46(3):647–667.

Flechtner, F., Neumayer, K.-H., Dahle, C., Dobslaw, H., Fagiolini, E., Raimondo, J.-C., and Güntner, A. (2016). What Can be Expected from the GRACE-FO Laser Ranging Interferometer for Earth Science Applications? *Surveys in Geophysics*, 37(2):453–470.

Flechtner, F., Reigber, C., Rummel, R., and Balmino, G. (2021). Satellite Gravimetry: A Review of Its Realization. *Surveys in Geophysics*, 42:1029–1074.

Fukumori, I., Raghunath, R., and Fu, L.-L. (1998). Nature of global large-scale sea level variability in relation to atmospheric forcing: A modeling study. *Journal of Geophysical Research: Oceans*, 103(C3):5493–5512.

Gelaro, R., McCarty, W., Suárez, M. J., Todling, R., Molod, A., Takacs, L., Randles, C. A., Darmenov, A., Bosilovich, M. G., Reichle, R., Wargan, K., Coy, L., Cullather, R., Draper, C., Akella, S., Buchard, V., Conaty, A., da Silva, A. M., Gu, W., Kim, G.-K., Koster, R., Lucchesi, R., Merkova, D., Nielsen, J. E., Partyka, G., Pawson, S., Putman, W., Rienecker, M., Schubert, S. D., Sienkiewicz, M., and Zhao, B. (2017). The Modern-Era Retrospective Analysis for Research and Applications, Version 2 (MERRA-2). *Journal of Climate*, 30(14):5419 – 5454.

Ghobadi-Far, K., Han, S.-C., McCullough, C. M., Wiese, D. N., Ray, R. D., Sauber, J., Shihora, L., and Dobslaw, H. (2022). Along-Orbit Analysis of GRACE Follow-On Inter-Satellite Laser Ranging Measurements for Sub-Monthly Surface Mass Variations. *Journal of Geophysical Research: Solid Earth*, 127(2).

Ghobadi-Far, K., Han, S.-C., McCullough, C. M., Wiese, D. N., Yuan, D.-N., Landerer, F. W., Sauber, J., and Watkins, M. M. (2020). GRACE Follow-On Laser Ranging Interferometer Measurements Uniquely Distinguish Short-Wavelength Gravitational Perturbations. *Geophysical Research Letters*, 47(16).

Ghobadi-Far, K., Šprlák, M., and Han, S.-C. (2019). Determination of ellipsoidal surface mass change from GRACE time-variable gravity data. *Geophysical Journal International*, 219(1):248–259.

Greatbatch, R. J. (1994). A note on the representation of steric sea level in models that conserve volume rather than mass. *Journal of Geophysical Research: Oceans*, 99(C6):12767–12771.

Gregory, J., Griffies, S., Hughes, C., Lowe, J., Church, J., Fukimori, I., Gomez, N., Kopp, R., Landerer, F., Cozannet, G. L., Ponte, R., Stammer, D., Tamisiea, M., and van de Wal, R. (2019). Concepts and terminology for sea level: Mean, variability and change, both local and global. *Surveys in Geophysics*, 40(6):1251–1289.

Haagmans, R., Siemes, C., Massotti, L., Carraz, O., and Silvestrin, P. (2020). ESA's next-generation gravity mission concepts. *Rendiconti Lincei. Scienze Fisiche e Naturali*, 31(S1):15–25.

Haagmans, R. and Tsaoussi, L. E. (2020). Next Generation Gravity Mission as a Mass-change And Geosciences International Constellation (MAGIC) Mission Requirements Document. *Earth and Mission Science Division, European Space Agency; NASA Earth Science Division.*

Hamlington, B. D., Gardner, A. S., Ivins, E., Lenaerts, J. T. M., Reager, J. T., Trossman, D. S., Zaron, E. D., Adhikari, S., Arendt, A., Aschwanden, A., Beckley, B. D., Bekaert, D. P. S., Blewitt, G., Caron, L., Chambers, D. P., Chandanpurkar, H. A., Christianson, K., Csatho, B., Cullather, R. I., DeConto, R. M., Fasullo, J. T., Frederikse, T., Freymueller, J. T., Gilford, D. M., Girotto, M., Hammond, W. C., Hock, R., Holschuh, N., Kopp, R. E., Landerer, F., Larour, E., Menemenlis, D., Merrifield, M., Mitrovica, J. X., Nerem, R. S., Nias, I. J., Nieves, V., Nowicki, S., Pangaluru, K., Piecuch, C. G., Ray, R. D., Rounce, D. R., Schlegel, N.-J., Seroussi, H., Shirzaei, M., Sweet, W. V., Velicogna, I., Vinogradova, N., Wahl, T., Wiese, D. N., and Willis, M. J. (2020). Understanding of Contemporary Regional Sea-Level Change and the Implications for the Future. *Reviews of Geophysics*, 58(3):e2019RG000672.

Han, S.-C., Yeo, I.-Y., Khaki, M., McCullough, C. M., Lee, E., and Sauber, J. (2021). Novel Along-Track Processing of GRACE Follow-On Laser Ranging Measurements Found Abrupt Water Storage Increase and Land Subsidence During the 2021 March Australian Flooding. *Earth and Space Science*, 8(11).

Hartmann, T. and Wenzel, H. (1994). The harmonic development of the Earth tide generating potential due to the direct effect of the planets. *Geophys. Res. Lett.*, 21(18):1991–1993.

Hartmann, T. and Wenzel, H.-G. (1995). The HW95 tidal potential catalogue. *Geophyical Res. Lett.*, 22(24):3553–3556.

Heiskanen, W. and Moritz, H. (1967). *Physical Geodesy.* Freeman. San Francisco.

Henderschott, M. C. (1972). The Effects of Solid Earth Deformation on Global Ocean Tides. *Geophysical Journal of the Royal Astronomical Society*, 29:389–402.

Hersbach, H., Bell, B., Berrisford, P., Hirahara, S., Horányi, A., Muñoz-Sabater, J., Nicolas, J., Peubey, C., Radu, R., Schepers, D., Simmons, A., Soci, C., Abdalla, S., Abellan, X., Balsamo, G., Bechtold, P., Biavati, G., Bidlot, J., Bonavita, M., De Chiara, G., Dahlgren, P., Dee, D., Diamantakis, M., Dragani, R., Flemming, J., Forbes, R., Fuentes, M., Geer, A., Haimberger, L., Healy, S., Hogan, R. J., Hólm, E., Janisková, M., Keeley, S., Laloyaux, P., Lopez, P., Lupu, C., Radnoti, G., de Rosnay, P., Rozum, I., Vamborg, F., Villaume, S., and Thépaut, J.-N. (2020). The ERA5 global reanalysis. *Quarterly Journal of the Royal Meteorological Society*, 146(730):1999–2049.

Hobbs, W. R., Klekociuk, A. R., and Pan, Y. (2020). Validation of reanalysis Southern Ocean atmosphere trends using sea ice data. *Atmospheric Chemistry and Physics*, 20(23):14757–14768.

Jungclaus, J. H., Fischer, N., Haak, H., Lohmann, K., Marotzke, J., Matei, D., Mikolajewicz, U., Notz, D., and von Storch, J. S. (2013). Characteristics of the ocean simulations in the Max Planck Institute Ocean Model (MPIOM) the ocean component of the MPI-Earth system model. *Journal of Advances in Modeling Earth Systems*, 5(2):422–446.

Kobayashi, S., Ota, Y., Harada, Y., Ebita, A., Moriya, M., Onoda, H., Onogi, K., Kamahori, H., Kobayashi, C., Endo, H., Miyaoka, K., and Takahashi, K. (2015). The JRA-55 Reanalysis: General Specifications and Basic Characteristics. *Journal of the Meteorological Society of Japan. Ser. II*, 93(1):5–48.

Korn, P., Brüggemann, N., Jungclaus, J. H., Lorenz, S. J., Gutjahr, O., Haak, H., Linardakis, L., Mehlmann, C., Mikolajewicz, U., Notz, D., Putrasahan, D. A., Singh, V., von Storch, J.-S., Zhu, X., and Marotzke, J. (2022). ICON-O: The Ocean Component of the ICON Earth System Model—Global Simulation Characteristics and Local Telescoping Capability. *Journal of Advances in Modeling Earth Systems*, 14(10):e2021MS002952.

Kuhlmann, J., Dobslaw, H., and Thomas, M. (2011). Improved modeling of sea level patterns by incorporating self-attraction and loading. *Journal of Geophysical Research: Oceans*, 116(C11).

Kvas, A., Behzadpour, S., Ellmer, M., Klinger, B., Strasser, S., Zehentner, N., and Mayer-Gürr, T. (2019). ITSG-Grace2018: Overview and Evaluation of a New GRACE-Only Gravity Field Time Series. *Journal of Geophysical Research: Solid Earth*, 124(8):9332–9344.

Kvas, A. and Mayer-Gürr, T. (2019). GRACE gravity field recovery with background model uncertainties. *Journal of Geodesy*, 93(12):2543–2552.

Landerer, F. W., Flechtner, F. M., Save, H., Webb, F. H., Bandikova, T., Bertiger, W. I., Bettadpur, S. V., Byun, S. H., Dahle, C., Dobslaw, H., Fahnestock, E., Harvey, N., Kang, Z., Kruizinga, G. L. H., Loomis, B. D., McCullough, C., Murböck, M., Nagel, P., Paik, M., Pie, N., Poole, S., Strekalov, D., Tamisiea, M. E., Wang, F., Watkins, M. M., Wen, H.-Y., Wiese, D. N., and Yuan, D.-N. (2020). Extending the Global Mass Change Data Record: GRACE Follow-On Instrument and Science Data Performance. *Geophysical Research Letters*, 47(12).

Landerer, F. W., Wiese, D. N., Bentel, K., Boening, C., and Watkins, M. M. (2015). North Atlantic meridional overturning circulation variations from GRACE ocean bottom pressure anomalies. *Geophysical Research Letters*, 42(19):8114–8121.

Levitus, S., Antonov, J., and Boyer, T. (2005). Warming of the world ocean, 1955–2003. *Geophysical Research Letters*, 32(2).

Loomis, B. D., Felikson, D., Sabaka, T. J., and Medley, B. (2021). High-Spatial-Resolution Mass Rates From GRACE and GRACE-FO: Global and Ice Sheet Analyses. *Journal of Geophysical Research: Solid Earth*, 126(12).

Lyard, F., Lefevre, F., Letellier, T., and Francis, O. (2006). Modelling the global ocean tides: Modern insights from FES2004. *Ocean Dyn.*, 56(5-6):394–415.

Lyard, F. H., Allain, D. J., Cancet, M., Carrère, L., and Picot, N. (2021). FES2014 global ocean tide atlas: design and performance. *Ocean Science*, 17(3):615–649.

Marsland, S., Haak, H., Jungclaus, J., Latif, M., and Röske, F. (2003). The Max-Planck-Institute global ocean/sea ice model with orthogonal curvilinear coordinates. *Ocean Modelling*, 5:91 – 127.

Massotti, L., Siemes, C., March, G., Haagmans, R., and Silvestrin, P. (2021). Next Generation Gravity Mission Elements of the Mass Change and Geoscience International Constellation: From Orbit Selection to Instrument and Mission Design. *Remote Sensing*, 13(19).

Mayer-Gürr, T., Behzadpour, S., Ellmer, M., Kvas, A., Klinger, B., Strasser, S., and Zehentner, N. (2018). ITSG-Grace2018 - Monthly, Daily and Static Gravity Field Solutions from GRACE. *GFZ Data Services*.

Munk, W. and MacDonald, G. J. F. (1960). *The Rotation of the Earth - A Geophysical Discussion*, volume 134. Cambridge Univ. Press, Cambridge U. K.

Noll, C. E., Ricklefs, R., Horvath, J., Mueller, H., Schwatke, C., and Torrence, M. (2019). Information resources supporting scientific research for the international laser ranging service. *Journal of Geodesy*, 93(11):2211–2225.

Nycander, J. (2005). Generation of internal waves in the deep ocean by tides. *J. Geophys. Res. C Ocean.*, 110(10):1–9.

Pekeris, C. L. (1974). A derivation of Laplace's tidal equation from the theory of inertial oscillations. *Proc. R. Soc. London*, 374:81–86. http://www.jstor.org/stable/2990346.

Penduff, T., Juza, M., Barnier, B., Zika, J., Dewar, W. K., Treguier, A.-M., Molines, J.-M., and Audiffren, N. (2011). Sea Level Expression of Intrinsic and Forced Ocean Variabilities at Interannual Time Scales. *Journal of Climate*, 24(21):5652 – 5670.

Penduff, T., Llovel, W., Close, S., Garcia-Gomez, I., and Leroux, S. (2019). Trends of Coastal Sea Level Between 1993 and 2015: Imprints of Atmospheric Forcing and Oceanic Chaos. *Surveys in Geophysics*, 40(6):1543–1562.

Petit, G. and Luzum, B. (2010). *IERS Convention (2010) (IERS Technical Note no. 36).* Verlag des Bundesamtes für Kartographie und Geodäsie, Frankfurt am Main. http://www.iers.org/IERS/EN/Publications/TechnicalNotes/tn36.html.

Ponte, R. M. (1993). Variability in a homogeneous global ocean forced by barometric pressure. *Dynamics of Atmospheres and Oceans*, 18(3–4):209–234.

Poropat, L., Kvas, A., Mayer-Gürr, T., and Dobslaw, H. (2019). Mitigating temporal aliasing effects of high-frequency geophysical fluid dynamics in satellite gravimetry. *Geophysical Journal International*, 220(1):257–266.

Quinn, K. J. and Ponte, R. M. (2011). Estimating high frequency ocean bottom pressure variability. *Geophysical Research Letters*, 38(8).

Ray, R. D. (1998). Ocean self-attraction and loading in numerical tidal models. *Marine Geodesy*, 21(3):181–192.

Ray, R. D. (2013). Precise comparisons of bottom-pressure and altimetric ocean tides. *J. Geophys. Res. Ocean.*, 118(9):4570–4584.

Riva, R. E. M., Bamber, J. L., Lavallée, D. A., and Wouters, B. (2010). Sea-level fingerprint of continental water and ice mass change from GRACE. *Geophysical Research Letters*, 37(19).

Rodell, M., Famiglietti, J. S., Wiese, D. N., Reager, J. T., Beaudoing, H. K., Landerer, F. W., and Lo, M.-H. (2018). Emerging trends in global freshwater availability. *Nature*, 557(7707):651–659.

Röske, F. (2005). Global oceanic heat and fresh water forcing datasets based on ERA-40 and ERA-15. *Reports on Earth System Science*, 13.

Russo, L. and Levy, S. (2003). *The Forgotten Revolution: How Science Was Born in 300 BC and Why it Had to Be Reborn*. Springer Berlin Heidelberg.

Sasgen, I., Wouters, B., Gardner, A. S., King, M. D., Tedesco, M., Landerer, F. W., Dahle, C., Save, H., and Fettweis, X. (2020). Return to rapid ice loss in Greenland and record loss in 2019 detected by the GRACE-FO satellites. *Communications Earth and Environment*, 1(1):8.

Save, H., Bettadpur, S., and Tapley, B. D. (2016). High-resolution CSR GRACE RL05 mascons. *Journal of Geophysical Research: Solid Earth*, 121(10):7547–7569.

Schaeffer, N. (2013). Efficient spherical harmonic transforms aimed at pseudospectral numerical simulations. *Geochemistry, Geophysics, Geosystems*, 14(3):751–758.

Schindelegger, M., Green, J. A., Wilmes, S. B., and Haigh, I. D. (2018). Can We Model the Effect of Observed Sea Level Rise on Tides? *J. Geophys. Res. Ocean.*, 123(7):4593–4609.

Schindelegger, M., Harker, A. A., Ponte, R. M., Dobslaw, H., and Salstein, D. A. (2021). Convergence of Daily GRACE Solutions and Models of Submonthly Ocean Bottom Pressure Variability. *Journal of Geophysical Research: Oceans*, 126(2).

Schlaak, M., Pail, R., Jensen, L., and Eicker, A. (2022). Closed loop simulations on recoverability of climate trends in next generation gravity missions. *Geophysical Journal International*, 232(2):1083–1098.

Schwiderski, E. (1980). Ocean tides, Part I: Global ocean tidal equations. *Marine Geodesy*, 3:161–217.

Seiler, U. (1991). Periodic changes of the angular momentum budget due to the tides of the World Ocean. *Journal of Geophysical Research: Solid Earth*, 96(B6):10287–10300.

Shihora, L., Balidakis, K., Dill, R., and Dobslaw, H. (2022a). Atmosphere and Ocean Non-Tidal Dealiasing Level-1B (AOD1B) Product RL07. GFZ Data Services.

Shihora, L., Balidakis, K., Dill, R., and Dobslaw, H. (2023a). AOe07 Variance-Covariance-Matrix. GFZ Data Services.

Shihora, L., Balidakis, K., Dill, R., and Dobslaw, H. (2023b). Assessing the stability of AOD1B atmosphere–ocean non-tidal background modelling for climate applications of satellite gravity data: long-term trends and 3-hourly tendencies. *Geophysical Journal International*, 234(2):1063–1072.

Shihora, L., Sulzbach, R., Dobslaw, H., and Thomas, M. (2022b). Self-attraction and loading feedback on ocean dynamics in both shallow water equations and primitive equations. *Ocean Modelling*, 169:101914.

Stepanov, V. N. and Hughes, C. W. (2004). Parameterization of ocean self-attraction and loading in numerical models of the ocean circulation. *Journal of Geophysical Research: Oceans*, 109(C3).

Sulzbach, R., Dobslaw, H., and Thomas, M. (2021). High-Resolution Numerical Modeling of Barotropic Global Ocean Tides for Satellite Gravimetry. *Journal of Geophysical Research: Oceans*, 126(5):e2020JC017097.

Swenson, S. and Wahr, J. (2002). Estimated effects of the vertical structure of atmospheric mass on the time-variable geoid. *Journal of Geophysical Research: Solid Earth*, 107(B9):ETG 4–1–ETG 4–11.

Sérazin, G., Penduff, T., Barnier, B., Molines, J.-M., Arbic, B. K., Müller, M., and Terray, L. (2018). Inverse Cascades of Kinetic Energy as a Source of Intrinsic Variability: A Global OGCM Study. *Journal of Physical Oceanography*, 48(6):1385 – 1408.

Sérazin, G., Penduff, T., Grégorio, S., Barnier, B., Molines, J.-M., and Terray, L. (2015). Intrinsic Variability of Sea Level from Global Ocean Simulations: Spatiotemporal Scales. *Journal of Climate*, 28(10):4279 – 4292.

Tamisiea, M. E., Hill, E. M., Ponte, R. M., Davis, J. L., Velicogna, I., and Vinogradova, N. T. (2010). Impact of self-attraction and loading on the annual cycle in sea level. *Journal of Geophysical Research: Oceans*, 115(C7).

Tapley, B. D., Bettadpur, S., Watkins, M., and Reigber, C. (2004). The gravity recovery and climate experiment: Mission overview and early results. *Geophysical Research Letters*, 31(9).

Tapley, B. D., Watkins, M. M., Flechtner, F., Reigber, C., Bettadpur, S., Rodell, M., Sasgen, I., Famiglietti, J. S., Landerer, F. W., Chambers, D. P., Reager, J. T., Gardner, A. S., Save, H., Ivins, E. R., Swenson, S. C., Boening, C., Dahle, C., Wiese, D. N., Dobslaw, H., Tamisiea, M. E., and Velicogna, I. (2019). Contributions of GRACE to understanding climate change. *Nature Climate Change*, 9(5):358–369.

Thomas, J. (1999). An Analysis of Gravity-Field Estimation Based on Intersatellite Dual-1-Way Biased Ranging (No. JPL-98-15); Technical Report. *Jet Propulsion Laboratory (JPL): Pasadena, CA, USA.* Available online: ftp://isdcftp.gfz-potsdam.de/grace/DOCUMENTS/ANCILLARY/ (accessed on 18 April 2023).

Thomas, M. and Sündermann, J. (1999). Tides and tidal torques of the world ocean since the last glacial maximum. *Journal of Geophysical Research: Oceans*, 104(C2):3159–3183.

Thomas, M., Sündermann, J., and Maier-Reimer, E. (2001). Consideration of ocean tides in an OGCM and impacts on subseasonal to decadal polar motion excitation. *Geophysical Research Letters*, 28(12):2457–2460.

Torge, W. and Müller, J. (2012). *Geodesy*. De Gruyter, Berlin, Boston.

Velicogna, I., Mohajerani, Y., A, G., Landerer, F., Mouginot, J., Noel, B., Rignot, E., Sutterley, T., van den Broeke, M., van Wessem, M., and Wiese, D. (2020). Continuity of Ice Sheet Mass Loss in Greenland and Antarctica From the GRACE and GRACE Follow-On Missions. *Geophysical Research Letters*, 47(8).

Velicogna, I., Sutterley, T. C., and van den Broeke, M. R. (2014). Regional acceleration in ice mass loss from Greenland and Antarctica using GRACE time-variable gravity data. *Geophysical Research Letters*, 41(22):8130–8137.

Velicogna, I. and Wahr, J. (2005). Greenland mass balance from grace. *Geophysical Research Letters*, 32(18).

Vinogradova, N. T., Ponte, R. M., Quinn, K. J., Tamisiea, M. E., Campin, J.-M., and Davis, J. L. (2015). Dynamic Adjustment of the Ocean Circulation to Self-Attraction and Loading Effects. *Journal of Physical Oceanography*, 45(3):678 – 689.

Vinogradova, N. T., Ponte, R. M., Tamisiea, M. E., Davis, J. L., and Hill, E. M. (2010). Effects of self-attraction and loading on annual variations of ocean bottom pressure. *Journal of Geophysical Research: Oceans*, 115(C6).

Volkov, D. L., Lee, S.-K., Landerer, F. W., and Lumpkin, R. (2017). Decade-long deep-ocean warming detected in the subtropical South Pacific. *Geophysical Research Letters*, 44(2):927–936.

Wahr, J., Molenaar, M., and Bryan, F. (1998). Time variability of the Earth's gravity field: Hydrological and oceanic effects and their possible detection using GRACE. *Journal of Geophysical Research: Solid Earth*, 103(B12):30205–30229.

Wang, H., Xiang, L., Jia, L., Jiang, L., Wang, Z., Hu, B., and Gao, P. (2012). Load Love numbers and Green's functions for elastic Earth models PREM, iasp91, ak135, and modified models with refined crustal structure from Crust 2.0. *Computers & Geosciences*, 49:190–199.

Weigelt, M., Sneeuw, N., Schrama, E. J. O., and Visser, P. N. A. M. (2013). An improved sampling rule for mapping geopotential functions of a planet from a near polar orbit. *Journal of Geodesy*, 87(2):127–142.

Weis, P., Thomas, M., and Sündermann, J. (2008). Broad frequency tidal dynamics simulated by a high-resolution global ocean tide model forced by ephemerides. *J. Geophys. Res. Ocean.*, 113(10).

Wiese, D. N., Bienstock, B., Blackwood, C., Chrone, J., Loomis, B. D., Sauber, J., Rodell, M., Baize, R., Bearden, D., Case, K., Horner, S., Luthcke, S., Reager, J. T., Srinivasan, M., Tsaoussi, L., Webb, F., Whitehurst, A., and Zlotnicki, V. (2022). The Mass Change Designated Observable Study: Overview and Results. *Earth and Space Science*, 9(8).

Wiese, D. N., Yuan, D.-N., Boening, C., Landerer, F. W., and Watkins, M. M. (2018). JPL GRACE Mascon Ocean, Ice, and Hydrology Equivalent Water Height Release 06 Coastal Resolution Improvement (CRI) Filtered Version 1.0. Ver. 1.0.

Wolff, J.-O., Maier-Reimer, E., and Legutke, S. (1997). The Hamburg Ocean Primitive Equation Model HOPE. *Tech. Rep. 13*. https://doi.org/10.2312/WDCC/DKRZ_Report_No13.

Wu, S.-C., Kruizinga, G., and Bertiger, W. (2004). Algorithm Theoretical Basis Document for GRACE Level-1B Data Processing V1.2. Technical Report GRACE 327-741. *Jet Propulsion Laboratory*. ftp://isdcftp.gfz-potsdam.de/grace/DOCUMENTS/Level-1/GRACE_Algorithm_Theoretical_Basis_Document_for_GRACE_L1B_Data_Processing.pdf.

Yoder, C. F., Williams, J. G., Dickey, J. O., Schutz, B. E., Eanes, R. J., and Tapley, B. D. (1983). Secular variation of Earth's gravitational harmonic J2 coefficient from Lageos and nontidal acceleration of Earth rotation. *Nature*, 303:757–762.

Yuan, D.-N. (2019). GRACE Follow-On JPL Level-2 Processing Standards Document. *Jet Propulsion Laboratory, California Institute of Technology, California, USA*. For Level-2 Product Release 06.

Zahel, W. (1977). A global hydrodynamic-numerical 1\degree-model of the ocean-tides; the oscillation system of the M2-tide and its distribution of energy dissipation. *Ann. Geophys.*, 33:31–40.

Zahel, W. (1978). The influence of solid Earth deformations on semidiurnal and diurnal ocean tides. In *Tidal Friction and the Earth's Rotation*, pages 98–124. Springer Verlag, Berlin, Heidelberg, New York.

Zenner, L., Gruber, T., Jäggi, A., and Beutler, G. (2010). Propagation of atmospheric model errors to gravity potential harmonics—impact on GRACE de-aliasing. *Geophysical Journal International*, 182(2):797–807.

Zhao, M., Ponte, R. M., Penduff, T., Close, S., Llovel, W., and Molines, J.-M. (2021). Imprints of Ocean Chaotic Intrinsic Variability on Bottom Pressure and Implications for Data and Model Analyses. *Geophysical Research Letters*, 48(24):e2021GL096341.

Zhou, H., Zheng, L., Pail, R., Liu, S., Qing, T., Yang, F., Guo, X., and Luo, Z. (2023). The impacts of reducing atmospheric and oceanic de-aliasing model error on temporal gravity field model determination. *Geophysical Journal International*, 234(1):210–227.

Zhu, S., Reigber, C., and König, R. (2004). Integrated adjustment of CHAMP, GRACE, and GPS data. *Journal of Geodesy*, 78(1–2).

Eidesstattliche Erklärung

Hiermit versichere ich an Eides statt, die vorliegende Dissertation selbstständig und ohne unerlaubte Hilfe angefertigt zu haben.

Bei der Verfassung der Dissertation wurden keine anderen als die im Text aufgeführten Hilfsmittel verwendet.

Ein Promotionsverfahren zu einem früheren Zeitpunkt an einer anderen Hochschule oder bei einem anderen Fachbereich wurde nicht beantragt.

Ort, Datum	Linus Shihora